

Carnegie Mellon University
MELLON COLLEGE OF SCIENCE

THESIS

SUBMITTED IN PARTIAL FULFILLMENT OF THE REQUIREMENTS
FOR THE DEGREE OF

DOCTOR OF PHILOSOPHY IN THE FIELD OF PHYSICS

TITLE: "Viral DNA Retention and Ejection Controlled by Capsid Stability "

PRESENTED BY: Krista Freeman

ACCEPTED BY THE DEPARTMENT OF PHYSICS

Alex Evilevitch 08/14/17
ALEX EVILEVITCH, CHAIR PROFESSOR DATE

Stephen Garoff 08/21/2017
STEPHEN GAROFF, DEPT HEAD DATE

APPROVED BY THE COLLEGE COUNCIL

Rebecca Doerge 08/24/2017
REBECCA DOERGE, DEAN DATE

Viral DNA Retention and Ejection Controlled by Capsid Stability

by
Krista Gabrielle Freeman

Submitted in partial fulfillment of the requirements for the degree of
Doctor of Philosophy

in

Physics

from

Carnegie Mellon University
Mellon College of Science
Pittsburgh, Pennsylvania, USA

Advised by Professor Alex Evilevitch
Defense date: May 18, 2017

Abstract

My thesis work explores the importance of metastability in the lifecycle of DNA viruses. Metastability refers to the fact that DNA viruses spend the majority of their lifetime in an energetically unfavorable state – that is, with a significant amount of stored internal energy in the form of tightly packaged DNA. This presents both a challenge and an advantage to the virus: the viral capsid must be both stable enough to retain its pressurized load during transit through harsh environments to the host, but also be unstable enough to quickly eject its genome into a host to begin the infection cycle. Here, I present data discussing both the destabilization occurring during the DNA ejection process and the mechanical stability needed to retain pressurized DNA.

To study the controlled destabilization a capsid undergoes during the infection process, I have used a combination of light scattering, x-ray scattering and cryo-electron microscopy to track the dynamics of viral DNA ejection. I showed first that receptor-bound phages eject their DNA stochastically with temperature-dependent rates correlated to an activation energy barrier [results published in the Journal of Physical Chemistry B (DOI: 10.1021/acs.jpcc.6b04172)]. In addition to this temperature dependence, the rate of the stochastic DNA ejection events is also greatly influenced by internal DNA pressure. A greater DNA pressure corresponds to more internal energy exerted on the portal, and thus a smaller excess energy barrier to overcome in destabilizing and opening the portal. This result suggests that DNA ejection occurs only after a 2-step unlocking process: the bacteriophage must not only bind to its receptor, but also acquire sufficient energy to critically destabilize the portal through DNA pressure and heat.

To study the capsid stability necessary to retain pressurized DNA, I used atomic force microscopy to measure the critical mechanical strength of herpes simplex virus type 1 (HSV-1) capsids with varying degrees of mechanical reinforcement. The data reveals that the capsid gains critical mechanical strength from external stabilization by the minor capsid protein UL25. To achieve full stability, the capsid must be fully occupied by a sufficient number of full-length UL25 copies. That is, without this full occupation of the capsid by UL25 proteins, infectious, DNA-containing virions cannot be formed. This suggests that the capsid structure and genetic coding are finely tuned to create a viral particle which is *just* strong enough and stable enough to ensure successful infection and replication, with no excess material carried or created.

Thus, we see that pressure is essential for efficient infection by viruses but also that pressure requires an extremely strong capsid. There must be a balance between storing enough energy (as DNA pressure) to power DNA ejection and storing more energy than the capsid can hold within its walls. This balance of pressure has been optimized through evolution, and results in the finely tuned and highly reproducible replication cycle of viruses. Understanding the purpose of and structural requirements for this stored energy will help the overall understanding of the mechanisms of viral infection.

Acknowledgements

I would like to start by acknowledging my PhD advisor, Dr. Alex Evilevitch, who has opened my eyes to a world of research I was unaware of before graduate school. Thank you, Alex, for sharing your excitement about virology with me and for teaching me via your own example how to tell the science story in a compelling way. Thank you also for giving me so many opportunities to travel the world in pursuit of scientific research – it has been a rewarding journey.

On that note, I would also like to thank my collaborators around the world for enabling me to do the experiments presented here. First and foremost, to Dr. Kiril Strelitzky of Cleveland State University: thank you not only for serving as the best undergraduate advisor a budding physicist could hope for, but even more so for evolving into a close collaborator as I pursued my PhD research. Your academic advice, friendly counsel, and of course endless laser time over the years has always been greatly appreciated. In addition, I must thank wholeheartedly Dr. Ulf Olsson for hosting me at Lund University in Sweden for two months in 2014. While I was at Lund for only a short time, I learned immensely and together we generated enough data for a nice paper. Continuing the thank-you tour around the world, I would also acknowledge beamline scientists at Paul Scherrer Institute in Switzerland (Dr. Urs Gasser and Dr. Joachim Kohlbrecher), Institut Laue-Langevin in France (Dr. Ralf Schweins), and Argonne National Lab in Illinois (Dr. Xiaobing Zuo) for hosting me for data collection and for teaching me many things about small angle scattering experiments. Last, but certainly not least, a whole hearted thank you to our local collaborators at the University of Pittsburgh, Dr. Fred Homa and Jamie Huffman, who have provided the materials and training necessary for experiments with HSV-1. A special thanks to Jamie for patiently and thoroughly answering my never-ending questions about all things biology.

I would next like to acknowledge generous support from the National Science Foundation Graduate Research Fellowship Grant (DGE-1252522 to K.G.F), as well as support from other National Science Foundation grants (CHE-1152770 and CHE- 1507694 to A.E.). The NSF fellowship, in addition to allowing me to pursue this research without pressures of teaching for my stipend, has already opened many doors for me. I will forever be indebted to the NSF for believing in my abilities, track record, and research proposal enough to fund me for these years.

With all of the directly research-related acknowledgements done, I would like to move now to thanking those who have supported me academically throughout this PhD experience. First and foremost, thank you to Dr. Steve Garoff for his consistent help, guidance, and advice as the physics department head while I pursued my degree. You performed this duty with a much-appreciated human touch while also making sure all my bases were covered. Similarly, thank you to members of my thesis committee (Dr. Mike Widom, Dr. Markus Deserno, Dr. Bob Suter, and Dr. Lynn Walker) for guiding me with thoughtful questions and suggestions to make this work the best it could be. Thanks also for your thoughtful advice regarding my goals and aspirations.

Of course, my education began long before joining CMU for my doctoral degree in physics. My academic successes come as a direct result of the support I had throughout my entire educational career. I have been fortunate enough to have a series of exceptional schools and caring teachers throughout my life. Thank you, in chronological order, to a lifetime of teachers from Metro Catholic Parish School, Saint Joseph Academy, and Cleveland State University.

Finally, I would like to thank those who have supported me in the most meaningful and necessary way: my family. To my mom and dad: from instilling a “no FUS” work ethic in me from a young age to teaching me when it is important to cut loose and party a little, you have given me the tools I needed excel while also living a happy and balanced life. Thanks for enduring with me all my stressful moments and celebrating with me in my relaxed moments. Thanks for feeding me, listening to me, and advising me when I needed you most. I love you both so much and I am so proud to be making you proud.

And to MG: only you can know how much writing these lines means to me. I could write a whole thesis on the countless ways you have lifted me onto your shoulders so that I could reach great heights. Instead, I will simply say: I love you, and thank you. Now, what are we talking about?

Contents

Chapter 1: Introduction and Motivation	1
1.1 A brief history of virology research	2
1.2 Modern physical virology research	3
1.3 An overview of the dsDNA viral “lifecycle”	4
1.3.1 DNA ejection and translocation	4
1.3.2 DNA packaging against force and pressure	6
1.3.3 The portal complex	6
1.4 DNA pressure and its role in viral survival	7
1.2.1 Tight packing	7
1.2.2 Electrostatic DNA repulsion energy	7
1.2.3 Repulsive hydration energy	8
1.2.4 DNA bending energy	9
1.5 Core questions	10
Chapter 2: Model Systems	15
2.1 Bacteriophage λ	15
2.1.1 Genetic and structural characterizations	16
2.1.2 Phage λ purification	16
2.1.3 Purification of the receptor protein LamB	18
2.2 Herpes Simplex Virus Type - 1	20
2.1.1 Genetic and structural characterizations	21
2.1.2 Purification of HSV-1 capsids	22
2.1.3 UL25 protein expression and purification	24
2.1.4 UL25 binding reaction	25
Chapter 3: Experimental methods	27
3.1 Light scattering	27

3.1.1 Dynamic light scattering	28
3.1.2 Static light scattering	29
3.1.3 DNA ejection dynamics experiments	31
3.1.4 Choice of angle	31
3.1.5 Dynamics curve normalization & analysis	33
3.1.6 LS system and sample details	34
3.2 Small angle scattering	34
3.2.1 Introduction to small angle scattering	34
3.2.2 SAS form factor modelling	36
3.2.1 SAXS experimental details.....	45
3.3 Cryo-transmission electron microscopy	46
3.3.1 Introduction to cryo-TEM	46
3.3.2 cryo-TEM experimental details	47
3.4 Atomic force microscopy	48
3.4.1 Introduction to atomic force microscopy	48
3.4.2 AFM calibration techniques	50
3.4.1 AFM measurement and data analysis	50
3.4.2 AFM experimental details	52
3.5 Quantitative Western Blot	53
Chapter 4: Controlled capsid destabilization (DNA ejection)	59
4.1 Introduction	59
4.1.1 Why are dynamics important?	59
4.1.2 Studying dynamics of specific viral processes	59
4.1.3 Early work on viral DNA ejection dynamics	59
4.2 Stochastic ejection of DNA from a population of bacteriophages	61
4.2.1 LS-measured DNA ejection dynamics: experiment and theory	61
4.2.2 LS-measured DNA ejection dynamics: understanding the whole curve.....	63

4.2.3 SAXS-measured DNA ejection dynamics	66
4.2.4 Cryo-TEM-measured DNA ejection dynamics	69
4.3.5 Combining all to show stochastic DNA ejection behavior	71
4.3 What causes the lag between receptor binding and DNA ejection initiation?	73
4.3.1 Portal as the Achilles' heel of phage λ	73
4.3.2 Temperature-induced destabilization of the portal	74
4.3.3 Pressure-induced destabilization of the portal	77
4.3.4 Electrostatic DNA-DNA friction and ejection dynamics	80
4.4 Ejection dynamics and viral fitness	83
4.5 Conclusions.....	84
Chapter 5: Critical capsid stability (DNA retention)	89
5.1 DNA packaging and retention in HSV-1	89
5.2.1 Prohead expansion caused by pressure buildup	89
5.2.2 Proteins needed to form the mature HSV-1 capsid	90
5.2.3 The biochemical basis for UL25 reinforcement	91
5.3 Post-assembly mechanical reinforcement by UL25	92
5.4 Mechanism of UL25 reinforcement	94
5.4.1 Full occupancy for full mechanical reinforcement.....	94
5.4.2 No binding = no reinforcement	98
5.4.3 Only full-length UL25 can fully reinforce the capsid	99
5.5 Quantifying the critical mechanical strength needed for DNA retention	101
5.6 Capsid softening at high temperatures causes mechanical failure	102
5.7 Conclusions.....	104
Chapter 5: Conclusions and future perspectives	108

List of Figures

- Figure 1.1: Virus “lifecycle”
Figure 1.2: DNA ejection into host
Figure 1.3: Cryo-EM map of HSV-1
Figure 1.4: Repulsive hydration forces
- Figure 2.1: Phage λ genetics and structure
Figure 2.2: ULTRA-Bradford test for LamB concentration
Figure 2.3: SDS-PAGE gel for LamB purification
Figure 2.4: HSV-1 cryo-EM reconstruction with parts labelled
Figure 2.5: Healthy and infected Vero cells
Figure 2.6: Sucrose gradient purification of HSV-1 capsids
Figure 2.7: UL25 protein purification
- Figure 3.1: Cartoon of light scattering from solution of particles
Figure 3.2: Illustration of time-dependent intensity fluctuations
Figure 3.3: Angle-dependent DLS on phage λ
Figure 3.4: Partial Zimm plot for phage λ
Figure 3.5: Illustration of LS ejection dynamics experiment
Figure 3.6: Explanation for choice of 120° as scattering angle
Figure 3.7: Semilog plot showing the double-exponential nature of LS curves
Figure 3.8: Example of SAXS on viruses
Figure 3.9: Cryo-EM reconstructions of HSV-1 and phage λ
Figure 3.10: Small angle scattering detector cartoon
Figure 3.11: SAXS data for filled & empty phage λ
Figure 3.12: Core-shell cartoon
Figure 3.13: Partially-filled capsid core-shell cartoon and model
Figure 3.14: Stochastic versus synchronized ejection illustrations
Figure 3.15: Nested core-shell model: 3 layers
Figure 3.16: Quantified cryo-EM map showing DNA distribution of phage λ
Figure 3.17: Multishell model compared to data
Figure 3.18: Multishell model compare with empty shell model
Figure 3.19: Importance of DNA layer placement in model
Figure 3.20: Contrast match cartoon
Figure 3.21: Cryo-TEM micrograph
Figure 3.22: AFM cantilever and tip cartoon
Figure 3.23: AFM force curve
Figure 3.24: Gallery of broken capsids
Figure 3.25: Western blot and quantified chart
Figure 3.26: Plot of % UL25 occupancy versus protein in binding reaction
- Figure 4.1: Typical LS dynamics curve and ejection initiation description
Figure 4.2: Theoretical description of intensity decay as a function of genome length
Figure 4.3: Stochastic and synchronized model cartoon
Figure 4.4: Diffusing DNA contribution to intensity
Figure 4.5: SAXS experimental results and analysis
Figure 4.6: SAXS modelling to rule out synchronized ejection
Figure 4.7: Cryo-EM micrograph collage
Figure 4.8: Partially-filled phages as a function of time

Figure 4.9: Agreement of three methods on ejection dynamics
Figure 4.10: Heat-triggered DNA ejection
Figure 4.11: LS ejection dynamics for 100% and 78% λ -DNA phages
Figure 4.12: SAXS support data
Figure 4.13: DNA ejection dynamics as a function of genome length
Figure 4.14: Activation energy
Figure 4.15: Effect of salt on DNA ejection dynamics

Figure 5.1: UL25 placement on HSV-1 capsid
Figure 5.2: AFM measurement illustration
Figure 5.3: Western Blot and binding curve
Figure 5.4: F_{break} and k as a function of UL25 occupancy
Figure 5.5: D_{max} as a function of UL25 occupancy
Figure 5.6: F_{break} and k as a function of UL25 amino acid length
Figure 5.7: Critical strength plot
Figure 5.8: F_{break} versus temperature

Abbreviations and Nomenclature

Phage λ : bacteriophage lambda

HSV-1: herpes simplex virus type 1

NPC: nuclear pore complex

wt: wild type

bp/kbp: basepair/kilo-basepair

aa: amino acid

LS: light scattering

DLS: dynamic light scattering

SLS: static light scattering

SAXS: small angle x-ray scattering

I: intensity

τ : characteristic time/exponential time constant

$\tau_{1/2}$: half-life

T: temperature

k_B : Boltzmann's constant

E_a : activation energy

AFM: atomic force microscopy

FZ curve: force versus distance curve

k: spring constant, or stiffness

F_{break} : force necessary to punch a hole in a capsid

atm: atmosphere

Chapter 1: Introduction and Motivation

1.1 A brief history of virology research

Viruses have plagued man since the beginning of life, and epidemics are the source of many dark periods in human history. The earliest written record, coinciding with the time of Hippocrates and the advent of medicine as a profession, dates back to the year 430 BC when the Athenian Plague wiped out more than a third of the population of Athens. The symptoms of the plague were described, in great detail, in only one record¹ written by the Greek Historian Thucydides, who begins his account by saying that “a pestilence of such extent and mortality was nowhere remembered”. Based on his vivid description of symptoms, modern researchers have attributed the plague to over 30 different diseases; the most commonly accepted sources are smallpox, measles, and typhoid. Today doctors and researchers access rigorously collected and documented medical evidence to diagnose and treat viral infections, but for thousands of years humans were sitting ducks when epidemics struck.

Fortunately, pioneering scientists invented tools to study what we now refer to as viruses, and even started developing vaccines as early as the 19th century²⁻³. The 20th century led into the golden age of virus discovery, with about 200 human viruses discovered in 100 years⁴. The golden age was about more than just a vast quantity of virus discoveries – the quality of virus science also skyrocketed as knowledge grew, laboratory equipment advanced⁵, and scientists learned how to produce, isolate, and study viruses in the lab. The 1930s brought new and innovate efforts to quantify the viral lifecycle⁶⁻⁷, catalog⁸⁻⁹ the conditions under which viruses thrive and suffer, and describe¹⁰ observed phenomena with equations and theories. These established preparation protocols¹¹ enabled scientists to consistently cultivate virus samples which were reproducible across generations. A natural consequence was the abundance of new knowledge of viral¹² and host¹³ genetics. In the 1950s the study of virology collided with day-to-day life like never before when the world experienced the peak of a prolonged outbreak of polio. Advances in virology allowed the University of Pittsburgh’s Dr. Jonas Salk to develop a vaccine¹⁴⁻¹⁵ which was met with initial hope and optimism, some skepticism and fear, and eventual widespread acceptance. It was, at its time, the most successful vaccination program in US history¹⁶ and it was the start of the virtual eradication of polio worldwide. With this success and robust public support, vaccine development continued through the rest of the 20th century¹⁷ and is still going strong today. Typical antiviral approaches today include prevention

via vaccination-based immunity or post-infection treatments with highly specific, and often harsh¹⁸, antiviral drugs¹⁹. Unfortunately it remains true that very few viruses can currently be *cured*. Furthermore, outbreaks of “new” viruses, like the highly publicized Ebola and Zika epidemics, still catch the medical community off guard because existing viral vaccines and treatments are too specific to combat emerging diseases.

1.2 Modern physical virology research

For the reasons described above, it is necessary to continue approaching quantitative virus studies from all angles – using different ideas, techniques, and analyses to map fundamental viral properties and, hopefully, reveal conserved traits or behaviors that can be exploited for less-specific antiviral drug approaches. There has already been significant progress in this direction in the 21st century. Scientists have generated new mathematical descriptions of virology – particularly in quantification of viral fitness²⁰, dynamic models of host infection^{21,22}, and even global analysis of viral epidemics²³. They have used viruses as new model systems for powerful physical characterization techniques²⁴⁻²⁷ not yet standard in the clinical research community. In this way, it has become possible to study viruses from a mechanistic, rather than medicinal, point of view. That is, rather than trying to understand the virus as a biochemically complex pathogen, it can be advantageous to reduce it to a genome-loaded nano-machine.

This has been the approach of quantified virology in the last several decades. Indeed, the term “physical virology” was even coined to describe the growing interdisciplinary interest in measuring the structures and behaviors of viruses. Physical virologists study the manifestation of the laws of physics in the viral structure, function, dynamics, and the general viral life cycle. My thesis research is focused on one unique aspect of physical virology: I aim to understand the consequences of the DNA pressure found in double-stranded DNA (dsDNA) viruses, such as bacteriophage λ and herpes simplex virus type-1 (my two model systems). In this type of virus, the microns-long genome (a very stiff and highly charged material) is packaged into the nanometer-scale virus head (called the capsid) through the portal complex, which is situated at one unique vertex of the capsid²⁸. As discussed in greater detail later in this chapter, the portal works with an ATP-driven molecular motor²⁹ which consumes energy to force DNA into the capsid, creating an internal pressure of tens of atmospheres³⁰⁻³¹. This pressure has enormous effects on the structure and function of the virus...in fact the pressure, and the metastable state of the virus it creates, is key to successful virus infection and replication. The virus must be, at once, both stable enough to retain its

pressurized load while traversing harsh environments to find a host, as well as unstable enough to efficiently transfer that DNA load into host. My research addresses this requirement of pressure-based metastability in the viral lifecycle.

1.3 An overview of the dsDNA virus “lifecycle”

While viruses are considered non-living due to their inability to reproduce without a host, they still have a highly regimented replication cycle. The details of replication, from the mechanism of transferring DNA to the host to the order of virion assembly, can change significantly for different types of viruses. That said, most dsDNA viruses share common steps in completion of their “lifecycle”: the virus ejects its DNA into the host, where it hijacks the host’s reproductive machinery to produce new viral DNA and proteins. Those proteins are self-assembled into pre-formed capsids, into which the new DNA is packaged to form progeny virions. The newly formed virions eventually lyse the host cell and go on to repeat the cycle. This cycle is simplified and illustrated for phage λ in Figure 1.1(left); the HSV-1 lifecycle is largely the same, but there are several key differences in the method of host infection, as illustrated in Figure 1.1(right). Unlike phage lambda, which keeps its body outside host and delivers its genome through a syringe-like tail, the HSV-1 virion actually enters its host fully. This requires an additional step which is mediated by the viral lipid envelope (it surrounds the capsid and encapsidated DNA), which fuses to the host cell membrane via endocytosis to allow the capsid to enter the cell. The capsid is then transported to the nucleus where it binds to the nuclear pore complex, triggering the translocation of DNA from the capsid and into the nucleus. Replication of viral protein and DNA and the assembly of new capsids proceeds within the nucleus in a very similar fashion to the process already described for phage λ . After assembly, capsids leave the nucleus and cell, acquiring tegument proteins and a lipid envelope on the way to ensure their infectivity for the next host.

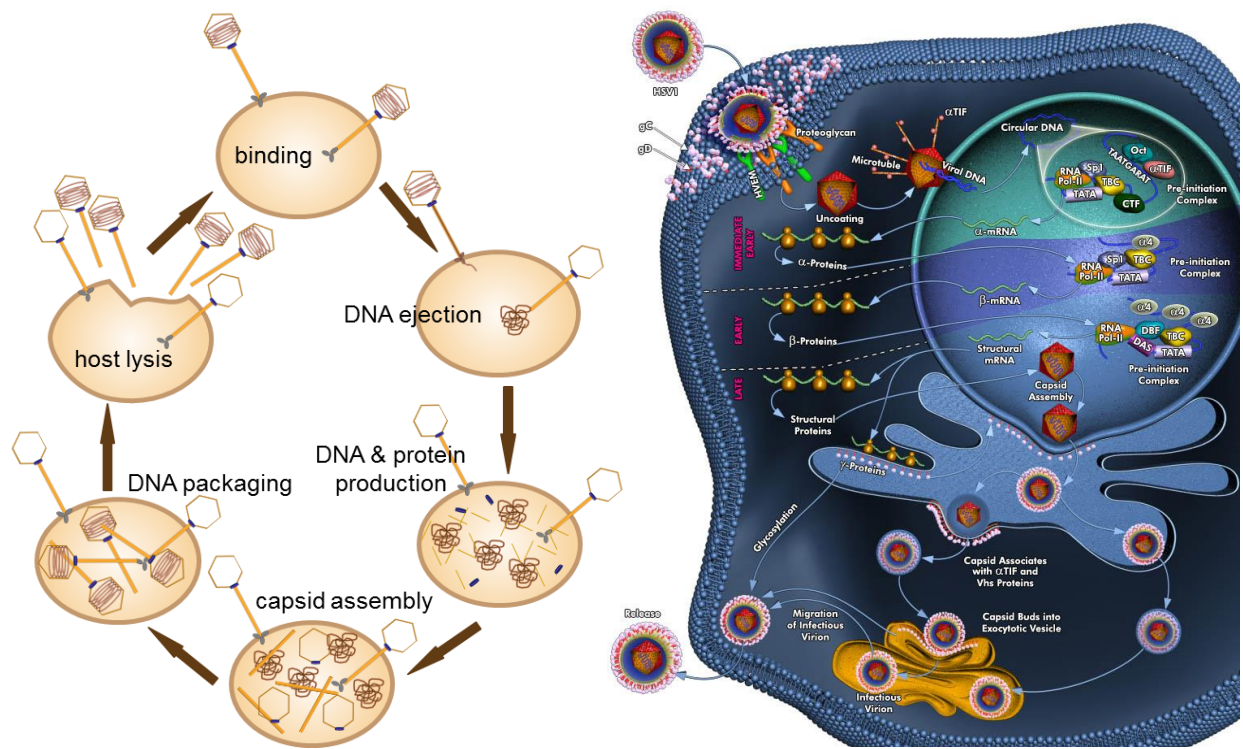


Figure 1.1: Illustrations of the replication cycles of phage λ (left) and HSV-1 (right). [HSV-1 illustration created by Qiagen (© 2009 QIAGEN, all rights reserved)]

1.3.1 DNA ejection and translocation

As described in the preceding section, an important first step in the viral replication cycle is the transfer of the genome to the host. In dsDNA viruses, this occurs via “DNA ejection” which is powered by the tens of atmospheres of pressure contained within the capsid³⁰⁻³² (this pressure is discussed in greater detail in section 1.4). There is at least one major difference in the mechanisms of DNA ejection for the two model viruses used in this thesis work: phage lambda “injects” DNA into the host through a long syringe-like tail, while the HSV-1 capsid itself docks to the host nucleus and ejects the DNA directly from the capsid into the nucleus (no tail). Despite this difference, due to the capsid structural similarities and comparable packing density/DNA pressure, it is reasonable to predict similar DNA ejection behaviors for HSV-1 and phage λ (both processes are illustrated in Figure 1.2, reprinted from a Science article by Gelbart and Knobler³³).

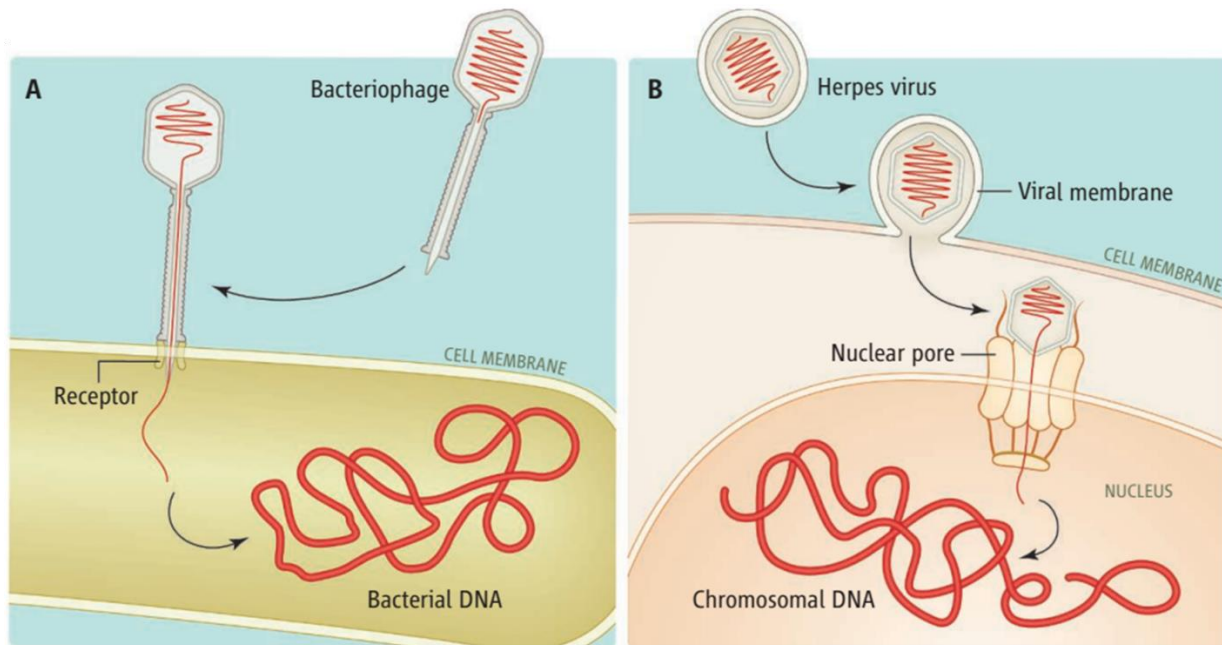


Figure 1.2: Pressure-driven DNA ejection illustrated³³ for (A) phage λ and (B) HSV-1

The DNA ejection and translocation process has been studied in much greater detail for phage λ , since its receptor protein can be isolated and used in *in vitro* ejection experiments^{26, 34-36} (so far not possible for HSV-1). These studies have revealed that the phage λ DNA ejection process depends on chemical, mechanical and thermal factors. Some of these factors are also known to influence HSV-1 DNA ejection. The first step is chemical; for phage λ the chemical trigger is binding with the receptor protein LamB, while for HSV-1 the chemical signal is binding to the nuclear pore complex (NPC). This chemical binding step sends the signal to the portal to open. The next step, which depends on both mechanical and thermal factors, is the subject of Chapter 4 of this thesis: the portal does not open instantaneously after binding occurs, but rather waits until sufficient thermo-mechanical stress is exerted on it. The final step is the actual translocation of the DNA out of the capsid, which again depends on mechanics (it is unclear whether this step depends on temperature or not). For wild-type phage λ the rate of genome translocation, measured with single-molecule experiments²⁶, can be as high as 60kbps/s. This fast translocation through the portal and tail leads to full DNA ejection in just 1.5 seconds. The rates of ejection are dependent on pressure, as evidenced by the 8-11 second ejection time for a shortened-genome mutant (containing only 78% of the DNA half of the pressure compared with wild type phage λ).

1.3.2 DNA packaging against force and pressure

Another critical step in the viral lifecycle is the successful packaging of DNA into the capsid. As discussed above, DNA packaging occurs within the host after the DNA copies have been replicated and the capsid proteins have self-assembled. Actually, DNA packaging begins not into mature capsids but into a capsid-precursor called the procapsid for both phage λ ³⁷ and HSV-1³⁸. When DNA packaging starts, the packaging motor binds first to the self-assembled procapsid, then binds to DNA and begins pushing it into the procapsid. This task is easy at first, but becomes much more difficult as the capsid gets filled with stiff and highly charged DNA. In fact, toward the end of packaging, the phage λ motor pushes against forces greater than 50pN²⁷, making it one of the strongest molecular motors in existence! The initiation of DNA packaging triggers ejection of scaffold proteins and the continued packing of DNA triggers expansion³⁹ of the loosely-assembled spherically icosahedral procapsid into the more rugged, more angularly icosahedral structures of mature capsids. This procapsid expansion is driven by the building internal DNA pressure which, as described in detail in section 1.4, builds up to tens of atmospheres by the end of the packaging process. To package against this building pressure the virus employs an energy-consuming motor which, according to experimental measurements, hydrolyzes about $\frac{1}{2}$ of an ATP molecule per basepair packaged⁴⁰.

1.3.3 The portal complex

The packaging motor is part of the portal complex, which binds to one unique vertex of the assembled icosahedral capsid^{37, 41} and contains hardware to enable the packaging, gating, and ejection of double stranded DNA. While the detailed structures of the λ and HSV-1 portals are unknown, they likely shares significant characteristics^{29, 42-43} with the portals of other double stranded DNA viruses. Many resources are devoted to understanding the workings of such portals; from genetic probing⁴⁴⁻⁴⁵ to near atomic-resolution structural experiments⁴⁶⁻⁴⁸ and from DNA packaging²⁷ force measurements to electrophysiological testing of the portal as a channel⁴⁹, scientists have collected many pieces of experimental data. In addition to experimental research there are numerous models⁵⁰⁻⁵¹ that address the structure-function relationships necessary to allow the portal complex to “open” and “close” in addition to exerting powerful packaging forces. While the opening of the portal, in particular, is of great importance in this thesis work, the exact mechanism of portal action is itself an active topic of research. It will thus not be

addressed in great detail in this document, though it is an interesting and complex question whose further study and characterization will certainly aid our understanding of virus machinery.

1.4 DNA pressure and its role in viral survival

Significant advances in physical virology were brought on by the theoretical prediction^{32, 52} and experimental quantification^{30-31, 53} of internal DNA pressure. Virus pressure is a consequence of the tight packaging of long strands of DNA into small capsids, and it is important in many aspects of the viral lifecycle (some of which are explored in this thesis). Below, I outline the physical conditions leading to DNA pressure.

1.4.1 Tight packing

In the case of phage λ , a 48.5kbp genome (16.4 μ m long) is packaged into a capsid with an inner radius of 29.4nm⁵⁴ and an outer radius of 31nm⁵⁵. On the other hand, HSV-1 packages 152kbp (51.4 μ m long) into a capsid of inner radius 46nm⁵⁶ and outer radius 62nm⁵⁶. These numbers correspond to DNA packing densities of 492mg/mL (phage λ) and 402mg/mL (HSV-1), putting the packaged DNA well within the range of liquid-crystalline densities⁵⁷⁻⁵⁸. This very high concentration causes hexagonal ordering of the DNA within the viral capsids – a very unique property found in only a couple other naturally occurring systems (sperm nuclei and ciliate chromatin⁵⁹). Aside from providing a unique system to study with techniques like x-ray scattering⁶⁰⁻⁶¹ and cryo-electron microscopy^{24, 62}, which beautifully reflect the ordered packaged DNA, this tight packing in viruses also leads to the internal virus pressure important to viral replication and survival. The pressure is stored energy – specifically electrostatic interaction energy, hydration repulsion energy, and bending energy of DNA^{32, 52}.

1.4.2 Electrostatic DNA repulsion energy

As mentioned above, the DNA is packaged into a hexagonal phase which has been experimentally observed with small angle x-ray scattering⁶⁰⁻⁶¹ and 3D reconstructions of cryo-electron microscopy^{24, 62} images. Such experiments show that the large DNA densities in capsids leave very little room for extra space between DNA layers. In fact, the interaxial spacing between neighboring DNA layers is just 27.5 Å for wild-type phage λ ⁶¹ and 31Å for HSV-1⁶³. These small interaxial distances correspond to surface-to-surface separations of just 7.5-11Å. In these extremely close quarters, illustrated with the 3D cryo-EM reconstruction in Figure 1.3, there are two repulsive forces that contribute to stored DNA pressure within the capsid.

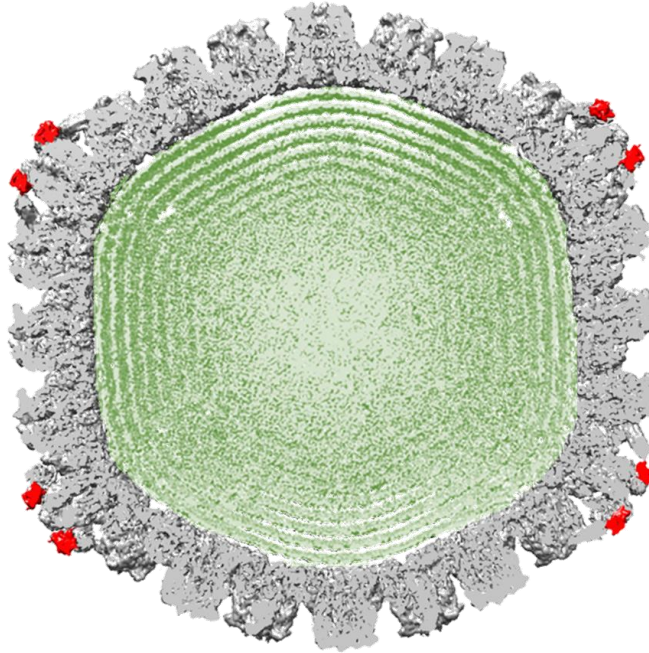


Figure 1.3: The DNA (green) that is packaged into the HSV-1 capsid (EMDB 6386²⁴) has an interaxial spacing of just $\sim 32\text{\AA}$ ⁶³, leaving it in a physically stressed (and energetic) state.

Electrostatic DNA-DNA repulsion is caused by Coulomb interactions between neighboring strands of highly charged DNA. Each DNA strand has a negative charge on the phosphate group, giving the DNA a uniform linear charge of exactly $1e/1.7\text{\AA}$. When strands of this charged molecule are brought into close proximity, as in the virus capsid, they feel a large repulsive electrostatic interaction. This interaction can be weakened by adding cationic salts to the system. The positive charges on the salts bind to the negative charges along the length of DNA, effectively screening the charge. In packaged DNA systems which have sufficient spacing between neighboring DNA strands (such as HSV-1 and the mutant of phage λ packaged with only 78% of the wild type genome length⁶⁴) adding salt screens the electrostatic repulsion enough to allow neighboring strands to move closer together, decreasing the measured interaxial spacing. In fully-packaged phage λ , however, the DNA is already so tightly packed that even adding salt to screen the DNA charges does not reduce the interaxial spacing. In this case, hydration forces (discussed below) are dominant.

1.4.3 Repulsive hydration energy

Beyond electrostatics, there is another repulsive energy felt in the packaged DNA system. When surface-to-surface separations get closer than 15\AA , the repulsive energy is dominated not by the Coulomb

interaction but instead by a repulsive hydration force. This hydration force is the source of more than 5000 scientific papers, and its exact mechanism is still not agreed upon! There are two forces at work here: the “primary hydration force” and the “secondary hydration force”⁶⁵. The primary force, most likely at work in viral DNA⁶⁶, is created by interactions between polarized water molecules bound to DNA. The polarization is caused by interactions between water and DNA – the phosphate groups of DNA, being hydrophilic and negatively charged, attract the positive charges of the water molecule. The result is a systematic polar reorientation of water molecules that results in the following picture: think of concentric DNA layers not just as two opposing, charged DNA layers but now with two additional charged water layers added in between to increase the repulsive force (illustrated in Figure 1.4). On the other hand, the “secondary hydration force” is caused by competition between water molecules bound to DNA and those bound to other solutes (like salts) in the system. This force arises when the water molecules are pulled away from phosphate groups to bind instead to the other solutes, leaving the DNA, in effect, dehydrated. The secondary force is dependent on salt concentration and is associated with weaker interactions.

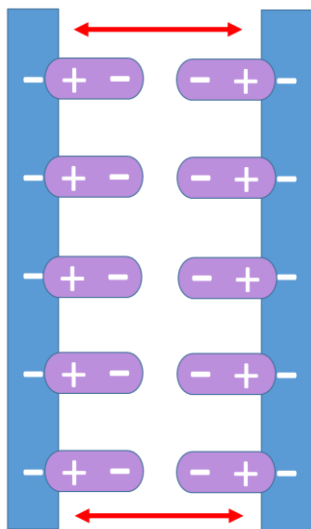


Figure 1.4: Cartoon showing the idea of repulsive primary hydration forces. The blue molecules are DNA, with negative charges associated with phosphate groups. The purple molecules are water, which are polarized by binding to the charged DNA. Repulsive interactions between neighboring DNA strands are increased by the polarized water layers, which act as additional charged layers between the already-repelling DNA layers.

1.4.4 DNA bending energy

Beyond the repulsive forces felt by DNA, there is an additional mechanical force caused by strong bending due to confinement in a small capsid. DNA enters capsids in an “inverse spool” conformation – that is, it winds into a structure resembling a very ordered ball of yarn, but from the outside in. The reason for this is simple to understand: DNA is a semi-rigid polymer with a persistence length of 50nm... it does

not easily bend into the small container of a viral capsid. Thus, as DNA is packed into the capsid it attempts to reduce the bending stress as much as possible by moving to the walls of the capsid. This strategy works very well for the first concentric layer of DNA, but when the second layer is packaged into the capsid things become more complicated due to the electrostatic and hydration repulsions described above.

As the second concentric DNA layer starts to pack into the capsid, again the DNA tries to minimize bending energy by moving as close to the capsid wall as possible. However, now the DNA encounters another source of unfavorable excess energy: electrostatic and hydration repulsive forces from the first concentric layer of packaged DNA and its bound water molecules. This repulsion from the first concentric layer pushes the second layer back toward the center of the capsid to relax the electrostatic interaction energy. And so it goes for all remaining concentric layers of DNA, such that the final DNA conformation is determined by a balance between bending energy and electrostatic repulsion. This balance depends most strongly on the packaging density of the virus, and is reflected in the interaxial spacings between neighboring DNA layers. This balance determines the internal DNA pressure exerted on the walls of the capsid – the pressure which is essential to many aspects of viral survival.

1.5 Core questions

In my doctoral thesis I will address the role of the large amount of DNA pressure in the retention and ejection of viral DNA. The pressure is stored energy, which means that dsDNA viruses exist in an energetically unfavorable state whenever they are packaged with DNA. This is the root of viral particle metastability, which is both a challenge to and an advantage for the virus – while the virus must be strong enough to hold all that energy as pressure during its travels through harsh environments to find a host, it eventually uses the stored energy to power DNA ejection and begin the replication cycle. Therefore, it is clear that without metastability the virus replication as we understand it would not work.

I will begin this dissertation by first describing in detail the model systems on which my work is based (Chapter 2): bacteriophage λ (or phage λ) and the human herpes simplex virus type-1 (HSV-1). In Chapter 3 I will introduce in detail all the experimental techniques and analysis methods used in this work. I will then show how these experiments have helped answer the following questions:

1) DNA ejection (Chapter 4): What role does particle metastability play in the population dynamics of viral DNA ejection? Does the amount of pressure, and thus the “magnitude” of the metastability, change the dynamics? How are population dynamics different from single molecule dynamics?

2) DNA retention (Chapter 5): How is the viral particle strong enough to hold tens of atmospheres of DNA pressure – this makes the capsid stronger than a car tire! What specifically gives the capsid its strength, and by what mechanism does it do so?

Answering these questions will help our overall understanding of the structure, function, and kinetic behavior of viral DNA and capsids. Understanding how these two main components of viruses work together can illuminate the fine-tuning that evolution has done to make these nano-machines as potent as possible. This knowledge is essential for the future development of broad-based antivirals and for the exploitation of virus components in nanotechnology.

References

1. Thucydides, History of the Peloponnesian War. London Dent: New York, 1914; p 652.
2. Pasteur, M., An Address on Vaccination in Relation to Chicken Cholera and Splenic Fever. *British medical journal* **1881**, 2, 283.
3. Jenner, E., *An Inquiry into the Causes and Effects of the Variolae Vaccinae*. Classics of Medicine Library, Division of Gryphon Editions: London, 1801.
4. Woolhouse, M.; Scott, F.; Hudson, Z.; Howey, R.; Chase-Topping, M., Human Viruses: Discovery and Emergence. *Philos Trans R Soc Lond B Biol Sci* **2012**, 367, 2864-2871.
5. Storch, G. A., Diagnostic Virology. *Clinical Infectious Diseases* **2000**, 31, 739-751.
6. Ellis, E. L.; Delbrück, M., The Growth of Bacteriophage. *The Journal of general physiology* **1939**, 22, 365-384.
7. Krueger, A. P., The Sorption of Bacteriophage by Living and Dead Susceptible Bacteria. *The Journal of general physiology* **1931**, 14, 493-516.
8. Northrop, J. H., Concentration and Purification of Bacteriophage. *The Journal of general physiology* **1938**, 21, 335.
9. Krueger, A. P., A Method for the Quantitative Determination of Bacteriophage. *The Journal of general physiology* **1930**, 13, 557-564.
10. Delbrück, M., The Growth of Bacteriophage and Lysis of the Host. *The journal of general physiology* **1940**, 23, 643-660.
11. Dulbecco, R.; Vogt, M., Plaque Formation and Isolation of Pure Lines with Poliomyelitis Viruses. *Journal of Experimental Medicine* **1954**, 99, 167-182.
12. Knight, C. A., The Nature of Some of the Chemical Differences among Strains of Tobacco Mosaic Virus. *Journal of Biological Chemistry* **1947**, 171, 297-308.
13. Luria, S. E.; Delbrück, M., Mutations of Bacteria from Virus Sensitivity to Virus Resistance. *Genetics* **1943**, 28, 491.
14. Salk, J. E., Poliomyelitis Vaccine in the Fall of 1955. *American Journal of Public Health and the Nation's Health* **1956**, 46, 1-14.
15. Salk, J. E., Considerations in the Preparation and Use of Poliomyelitis Virus Vaccine. *Journal of the American Medical Association* **1955**, 158, 1239-1248.
16. Glasser, M. A., Attitudes and Reactions of the Public to Health Programs: I. A Study of the Public's Acceptance of the Salk Vaccine Program. *American Journal of Public Health and the Nations Health* **1958**, 48, 141-146.
17. Fischl, M. A.; Richman, D. D.; Grieco, M. H.; Gottlieb, M. S.; Volberding, P. A.; Laskin, O. L.; Leedom, J. M.; Groopman, J. E.; Mildvan, D.; Schooley, R. T., The Efficacy of Azidothymidine (Azt) in the Treatment of Patients with Aids and Aids-Related Complex. *New England Journal of Medicine* **1987**, 317, 185-191.
18. Lewis, W.; Dalakas, M. C., Mitochondrial Toxicity of Antiviral Drugs. *Nature medicine* **1995**, 1, 417-422.
19. De Clercq, E., Antiviral Drugs in Current Clinical Use. *J Clin Virol* **2004**, 30, 115-133.
20. Marée, A. F.; Keulen, W.; Boucher, C. A.; De Boer, R. J., Estimating Relative Fitness in Viral Competition Experiments. *Journal of virology* **2000**, 74, 11067-11072.
21. Dimitrov, D.; Willey, R.; Sato, H.; Chang, L.-J.; Blumenthal, R.; Martin, M., Quantitation of Human Immunodeficiency Virus Type 1 Infection Kinetics. *Journal of virology* **1993**, 67, 2182-2190.
22. Culshaw, R. V.; Ruan, S., A Delay-Differential Equation Model of Hiv Infection of Cd4+ T-Cells. *Mathematical biosciences* **2000**, 165, 27-39.
23. Corbett, E. L.; Watt, C. J.; Walker, N.; Maher, D.; Williams, B. G.; Raviglione, M. C.; Dye, C., The Growing Burden of Tuberculosis: Global Trends and Interactions with the Hiv Epidemic. *Archives of internal medicine* **2003**, 163, 1009-1021.
24. Huet, A.; Makhov, A. M.; Huffman, J. B.; Vos, M.; Homa, F. L.; Conway, J. F., Extensive Subunit Contacts Underpin Herpesvirus Capsid Stability and Interior-to-Exterior Allostery. *Nature structural & molecular biology* **2016**.
25. Van Valen, D.; Wu, D.; Chen, Y. J.; Tuson, H.; Wiggins, P.; Phillips, R., A Single-Molecule Hershey-Chase Experiment. *Curr Biol* **2012**, 22, 1339-1343.
26. Grayson, P.; Han, L.; Winther, T.; Phillips, R., Real-Time Observations of Single Bacteriophage Lambda DNA Ejections in Vitro. *Proc Natl Acad Sci U S A* **2007**, 104, 14652-14657.

27. Smith, D. E., Single-Molecule Studies of Viral DNA Packaging. *Current opinion in virology* **2011**, *1*, 134-141.
28. Dube, P.; Tavares, P.; Lurz, R.; Van Heel, M., The Portal Protein of Bacteriophage Spp1: A DNA Pump with 13-Fold Symmetry. *The EMBO journal* **1993**, *12*, 1303.
29. Rao, V. B.; Feiss, M., The Bacteriophage DNA Packaging Motor. *Annu Rev Genet* **2008**, *42*, 647-681.
30. Evilevitch, A.; Lavelle, L.; Knobler, C. M.; Raspaud, E.; Gelbart, W. M., Osmotic Pressure Inhibition of DNA Ejection from Phage. *Proc Natl Acad Sci U S A* **2003**, *100*, 9292-9295.
31. Grayson, P.; Evilevitch, A.; Inamdar, M. M.; Purohit, P. K.; Gelbart, W. M.; Knobler, C. M.; Phillips, R., The Effect of Genome Length on Ejection Forces in Bacteriophage Lambda. *Virology* **2006**, *348*, 430-436.
32. Tzllil, S.; Kindt, J. T.; Gelbart, W. M.; Ben-Shaul, A., Forces and Pressures in DNA Packaging and Release from Viral Capsids. *Biophys J* **2003**, *84*, 1616-1627.
33. Gelbart, W. M.; Knobler, C. M., Pressurized Viruses. *Science* **2009**, *323*, 1682-1683.
34. Lof, D.; Schillen, K.; Jonsson, B.; Evilevitch, A., Forces Controlling the Rate of DNA Ejection from Phage Lambda. *J Mol Biol* **2007**, *368*, 55-65.
35. Lof, D.; Schillen, K.; Jonsson, B.; Evilevitch, A., Dynamic and Static Light Scattering Analysis of DNA Ejection from the Phage Lambda. *Phys Rev E Stat Nonlin Soft Matter Phys* **2007**, *76*, 011914.
36. Wu, D.; Van Valen, D.; Hu, Q.; Phillips, R., Ion-Dependent Dynamics of DNA Ejections for Bacteriophage Lambda. *Biophys J* **2010**, *99*, 1101-1109.
37. Bazinet, C.; King, J., The DNA Translocating Vertex of Dsdna Bacteriophage. *Annu Rev Microbiol* **1985**, *39*, 109-129.
38. Newcomb, W. W.; Thomsen, D. R.; Homa, F. L.; Brown, J. C., Assembly of the Herpes Simplex Virus Capsid: Identification of Soluble Scaffold-Portal Complexes and Their Role in Formation of Portal-Containing Capsids. *Journal of Virology* **2003**, *77*, 9862-9871.
39. Medina, E.; Nakatani, E.; Kruse, S.; Catalano, C. E., Thermodynamic Characterization of Viral Procapsid Expansion into a Functional Capsid Shell. *J Mol Biol* **2012**, *418*, 167-180.
40. Guo, P.; Peterson, C.; Anderson, D., Prohead and DNA-Gp3-Dependent Atpase Activity of the DNA Packaging Protein Gp16 of Bacteriophage Φ 29. *Journal of molecular biology* **1987**, *197*, 229-236.
41. Johnson, J. E.; Chiu, W., DNA Packaging and Delivery Machines in Tailed Bacteriophages. *Curr Opin Struct Biol* **2007**, *17*, 237-243.
42. Johnson, J. E.; Chiu, W., DNA Packaging and Delivery Machines in Tailed Bacteriophages. *Current opinion in structural biology* **2007**, *17*, 237-243.
43. Fokine, A.; Rossmann, M. G., Molecular Architecture of Tailed Double-Stranded DNA Phages. *Bacteriophage* **2014**, *4*, e28281.
44. Bazinet, C.; King, J., The DNA Translocating Vertex of Dsdna Bacteriophage. *Ann. Rev. Microbiol.* **1985**, *39*, 109-129.
45. Black, L. W., DNA Packaging in Dsdna Bacteriophages. *Annual Reviews in Microbiology* **1989**, *43*, 267-292.
46. Lhuillier, S.; Gallopin, M.; Gilquin, B.; Brasiles, S.; Lancelot, N.; Letellier, G.; Gilles, M.; Dethan, G.; Orlova, E. V.; Couprie, J.; et al., Structure of Bacteriophage Spp1 Head-to-Tail Connection Reveals Mechanism for Viral DNA Gating. *Proc Natl Acad Sci U S A* **2009**, *106*, 8507-8512.
47. Tang, J.; Lander, G. C.; Olia, A.; Li, R.; Casjens, S.; Prevelige, P.; Cingolani, G.; Baker, T. S.; Johnson, J. E., Peering Down the Barrel of a Bacteriophage Portal: The Genome Packaging and Release Valve in P22. *Structure* **2011**, *19*, 496-502.
48. Olia, A. S.; Prevelige, P. E., Jr.; Johnson, J. E.; Cingolani, G., Three-Dimensional Structure of a Viral Genome-Delivery Portal Vertex. *Nat Struct Mol Biol* **2011**, *18*, 597-603.
49. Geng, J.; Fang, H.; Haque, F.; Zhang, L.; Guo, P., Three Reversible and Controllable Discrete Steps of Channel Gating of a Viral DNA Packaging Motor. *Biomaterials* **2011**, *32*, 8234-8242.
50. Padilla-Sanchez, V.; Gao, S.; Kim, H. R.; Kihara, D.; Sun, L.; Rossmann, M. G.; Rao, V. B., Structure-Function Analysis of the DNA Translocating Portal of the Bacteriophage T4 Packaging Machine. *J Mol Biol* **2014**, *426*, 1019-1038.
51. Tavares, P.; Zinn-Justin, S.; Orlova, E. V., Genome Gating in Tailed Bacteriophage Capsids. In *Viral Molecular Machines*, Springer: 2012; pp 585-600.
52. Purohit, P. K.; Kondev, J.; Phillips, R., Mechanics of DNA Packaging in Viruses. *Proc Natl Acad Sci U S A* **2003**, *100*, 3173-3178.

53. Bauer, D. W.; Huffman, J. B.; Homa, F. L.; Evilevitch, A., Herpes Virus Genome, the Pressure Is On. *J Am Chem Soc* **2013**, *135*, 11216-11221.
54. Earnshaw, W.; Harrison, S., DNA Arrangement in Isometric Phage Heads. *Nature* **1977**, *268*, 598-602.
55. Earnshaw, W. C.; Hendrix, R. W.; King, J., Structural Studies of Bacteriophage Lambda Heads and Proheads by Small Angle X-Ray Diffraction. *Journal of molecular biology* **1979**, *134*, 575-594.
56. Wu, L.; Lo, P.; Yu, X.; Stoops, J. K.; Forghani, B.; Zhou, Z. H., Three-Dimensional Structure of the Human Herpesvirus 8 Capsid. *Journal of virology* **2000**, *74*, 9646-9654.
57. Knobler, C. M.; Gelbart, W. M., Physical Chemistry of DNA Viruses. *Annu Rev Phys Chem* **2009**, *60*, 367-383.
58. Booy, F.; Newcomb, W.; Trus, B.; Brown, J.; Baker, T.; Steven, A., Liquid-Crystalline, Phage-Like Packing of Encapsidated DNA in Herpes Simplex Virus. *Cell* **1991**, *64*, 1007-1015.
59. Livolant, F., Ordered Phases of DNA in Vivo and in Vitro. *Physica A: Statistical Mechanics and its Applications* **1991**, *176*, 117-137.
60. Li, D.; Liu, T.; Zuo, X.; Li, T.; Qiu, X.; Evilevitch, A., Ionic Switch Controls the DNA State in Phage Lambda. *Nucleic Acids Res* **2015**, *43*, 6348-6358.
61. Liu, T.; Sae-Ueng, U.; Li, D.; Lander, G. C.; Zuo, X.; Jonsson, B.; Rau, D. C.; Schefer, I.; Evilevitch, A., Solid-to-Fluid-Like DNA Transition in Viruses Facilitates Infection. *Proc Natl Acad Sci U S A* **2015**, *112*, 14675-14680.
62. Lander, G. C.; Johnson, J. E.; Rau, D. C.; Potter, C. S.; Carragher, B.; Evilevitch, A., DNA Bending-Induced Phase Transition of Encapsidated Genome in Phage Lambda. *Nucleic Acids Res* **2013**, *41*, 4518-4524.
63. Sae-Ueng, U.; Li, D.; Zuo, X.; Huffman, J. B.; Homa, F. L.; Rau, D.; Evilevitch, A., Solid-to-Fluid DNA Transition inside Hsv-1 Capsid Close to the Temperature of Infection. *Nat Chem Biol* **2014**, *10*, 861-867.
64. Qiu, X.; Rau, D. C.; Parsegian, V. A.; Fang, L. T.; Knobler, C. M.; Gelbart, W. M., Salt-Dependent DNA-DNA Spacings in Intact Bacteriophage Lambda Reflect Relative Importance of DNA Self-Repulsion and Bending Energies. *Phys Rev Lett* **2011**, *106*, 028102.
65. Parsegian, V.; Zemb, T., Hydration Forces: Observations, Explanations, Expectations, Questions. *Current opinion in colloid & interface science* **2011**, *16*, 618-624.
66. Bloomfield, V. A., DNA Condensation by Multivalent Cations. *Biopolymers* **1997**, *44*, 269-282.

Chapter 2: Model Systems

2.1 Bacteriophage λ

The model system for all the scattering experiments presented in this thesis was bacteriophage λ , commonly called phage λ . Bacteriophages are viruses which infect, reproduce within, and ultimately kill bacteria. There are an estimated 10^{31} bacteriophage particles on Earth, making the phage population more abundant than the sum of all organisms, from bacteria to humans². In addition to being most abundant, the phage population is also highly

genetically diverse - evidence of many long and varying evolutionary pathways³. Despite this genetic diversity, most

Fun fact: the word phage comes from the Greek *phagein* – “to eat” – so bacteriophages are literally bacteria eaters.

Phage λ was discovered in 1950 when then-PhD student Esther Lederberg found¹ her *e coli* colonies “nibbled and plaqued” – they had been lysed (“eaten”) by phage λ .

bacteriophages do have significant conserved traits. For example, the majority of phages have structurally similar capsids which retain at least 15kbp of double stranded DNA (dsDNA). Because of these conserved traits, phage λ has often been used as a model to study dsDNA bacteriophages in general. It makes a good model, in part, because its DNA-ejection-triggering receptor protein, LamB, is known and can be isolated for use in *in vitro* experiments. Thus, the λ -LamB system makes a clean system for studying the mechanism of pressurized viral DNA ejection. This is its purpose in this thesis.

2.1.1 Genetic and structural characteristics of phage λ

Phage λ consists of an icosahedral capsid (the virus “head”, about 65nm in diameter) and a tail (about 135nm in length). Both the capsid and tail are made of proteins and are connected to each other by a protein complex called the portal (the portal is discussed in greater detail in Chapter 1). The capsid stores the phage genome, which for the wild type phage is 48.5kbp of double-stranded DNA. When this long and stiff (wild type DNA is 16.4 μ m long with a persistence length of 50nm) DNA is packed into the ~32nm radius capsid, DNA pressures of tens of atmospheres are achieved⁴ (the origin of pressurized DNA is discussed in greater detail in Chapter 1). The cartoon and cryo-EM micrograph in Figure 2.1, both published in 2011

by Rajagopala et al⁵, summarize the structural information known for the phage λ virus, including the name and copy number of all the component proteins.

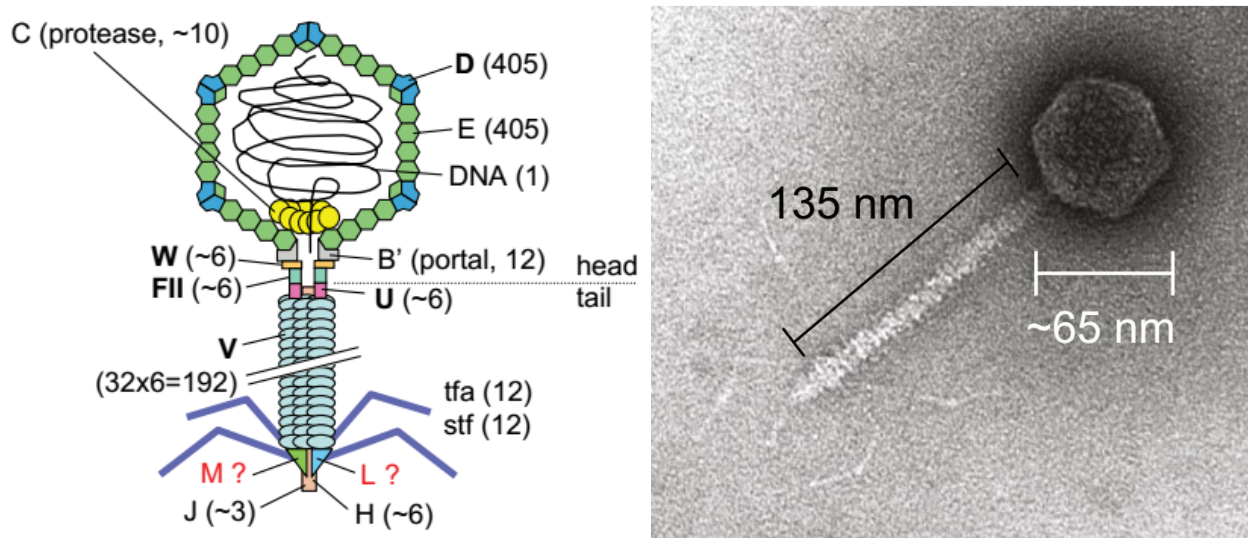


Figure 2.1: The cartoon illustrates the protein interactions resulting in a phage λ virion, while the cryo-EM micrograph gives a snapshot of physical dimensions. Published by Rajagopala et al⁵.

2.1.2 Phage λ purification

One of my first tasks in the lab was to learn how to make my own stocks of phage λ for experiments.

Phage λ is produced and purified with the following general procedure:

- 1) E coli cells which are lysogenically infected with phage λ (actually, a strain of phage λ with a mutation that causes the lytic cycle repressor protein to function at temperatures below 37°C, but become non-functional at higher temperatures⁶) are streaked from a frozen culture onto an agar plate containing LB and antibiotics. This plate is incubated at 30°C (where the repressor protein is active and the infection is still lysogenic) for ~20 hours to allow the infected bacterial colonies to multiply. Controls are done to ensure no contamination is present on the plate.
- 2) Starter cultures are made by inoculating tubes of LB broth with a single bacterial colony. The starter cultures are incubated (shaking) at 30°C for 12-16 hours to allow the bacteria to grow and proliferate. The once-clear LB broth becomes cloudy as bacteria multiply.
- 3) The bacteria-laden starter cultures are used to inoculate large volumes of YT broth. The YT broth flasks are incubated, shaking, at 30°C until they become cloudy from bacterial growth (~3 hours).

- 4) The phage λ lytic cycle is triggered by transferring the cultures to a 42°C shaking water bath. At this high temperature, the lytic cycle repressor protein is “turned off” and a large number of progeny phages begin to assemble in the infected bacteria. The lytic growth of phages results in bacterial cell lysis and the release of phages into the medium. As the bacteria rupture, the medium becomes clear again –indicating that most of the phages are already out of the cells and are ready to harvest and purify.
- 5) Any remaining intact bacterial cells are lysed by adding chloroform and incubating at 30°C. Also add DNase and RNase (to digest the bacterial DNA and RNA) as well as enough solid NaCl to bring the NaCl concentration up to 0.5M.
- 6) Phages are separated from the cell debris by centrifugation. The pellet is cell debris and can be discarded. The supernatant contains the phages.
- 7) Phages are precipitated by adding PEG-8000 to 10% w/v and allowing this mixture to incubate at 4°C overnight. The combination of the 0.5M NaCl (added in step 5) and the PEG makes the viruses insoluble and they aggregate together and precipitate⁷. The precipitation is encouraged by centrifugation to pellet the phages.
- 8) The phage-rich pellet is resuspended and PEG is removed by adding chloroform (enough to double the total volume) and centrifuging to separate the aqueous phase (top layer, contains phages), PEG (a solid middle layer) and chloroform (the lowest layer). The aqueous phase is harvested for further purification.
- 9) The phages are purified via ultracentrifugation on a CsCl gradient to separate heavier phages from other smaller soluble contamination in the solution. The phages form a band, which is extracted via side punch and dialyzed in the desired buffer for further use.

The above procedure was performed for isolation of λ phages with genome lengths of 48.5kbp (λ cl875, referred to throughout the text as “100% λ -DNA” phage), 41.5kbp (EMBL3, referred to throughout the text as “94% λ -DNA” phage), or 37.7kbp (λ b221, referred to throughout the text as “78% λ -DNA” phage). Phage samples were dialyzed in TM buffer (50 mM Tris, supplemented by 5 or 20 mM MgCl₂, pH 7.4). Throughout this study, we use varying MgCl₂ concentrations added to Tris buffer. Since Tris is used for all buffers in

this study, buffer solutions are referred to by the added MgCl₂ concentration, with the naming scheme TM-5 (indicating 50mM Tris, 5mM MgCl₂) or TM-20 (50mM Tris, 20mM MgCl₂).

2.1.3 Purification of the receptor protein LamB

The receptor was the LamB protein, an outer membrane protein of *e. coli*. It was first isolated in 1973 by Randall-Hazelbauer and Schwartz⁸, who also showed that the purified receptor protein retains its phage-inactivating function. LamB is a 160kDa trimer of proteins⁹ which make up the maltose porin channel of *e. coli*¹⁰. For this work, LamB was purified from pop 154 (a strain of *E. coli* K12 in which the *LamB* gene has been transduced from *Shigella sonnei* 3070) using the following protocol¹¹:

- 1) Pop154 bacteria are streaked from a frozen culture onto an LB-agar plate. This plate is incubated at 37°C overnight to allow the infected bacterial colonies to multiply. Controls are done to ensure no contamination is present on the plate.
- 2) Starter cultures are made by inoculating tubes of LB broth with a single bacterial colony then adding maltose to a final concentration of 0.2% (the maltose induces expression of the LamB since it is the maltoporin complex). The starter cultures are incubated (shaking) at 36°C for 6 hours to allow the bacteria to grow and proliferate. The once-clear LB broth becomes cloudy as bacteria multiply.
- 3) The bacteria-laden starter cultures are used to inoculate large volumes of LB broth + 0.2% Maltose. The LB broth flasks are incubated, shaking, at 37°C until they become cloudy from bacterial growth (12-14 hours).
- 4) Cells are harvested by centrifugation and frozen at -80°C overnight.
- 5) Cell pellet is thawed and cells are lysed by resuspension in breaking buffer (50mM NaPO₄, 100mM NaCl, and sonication. Centrifugation separated the large cell debris (pellet) from the desired membrane proteins (supernatant) and further ultracentrifugation is used to pellet the membrane proteins.
- 6) LamB is isolated by iterating the following procedure with ever-increasing concentrations of the solubilizing detergent oPOE (n-Octyl-oligo-oxyethylene): the membrane protein pellet is resuspended in sodium phosphate buffer and homogenized, then incubated with a small (0.3%)

concentration of oPOE to solubilize small and weakly bound membrane proteins. The solution is ultracentrifuged to pellet unsolubilized membrane proteins (such as LamB) and then resuspended as described above, but incubated with a larger (first 0.5%, then 1.0%) oPOE concentration. This repeats up to the final oPOE concentration of 3.0%, when LamB is solubilized and remains in the supernatant for the subsequent spin.

- 7) The solubilized LamB is purified via an affinity column (specifically, a gravity-flow amylose resin column) eluted with 20% maltose. The elution fractions, which are rich in LamB, are collected and tested with an ULTRA-Bradford assay:

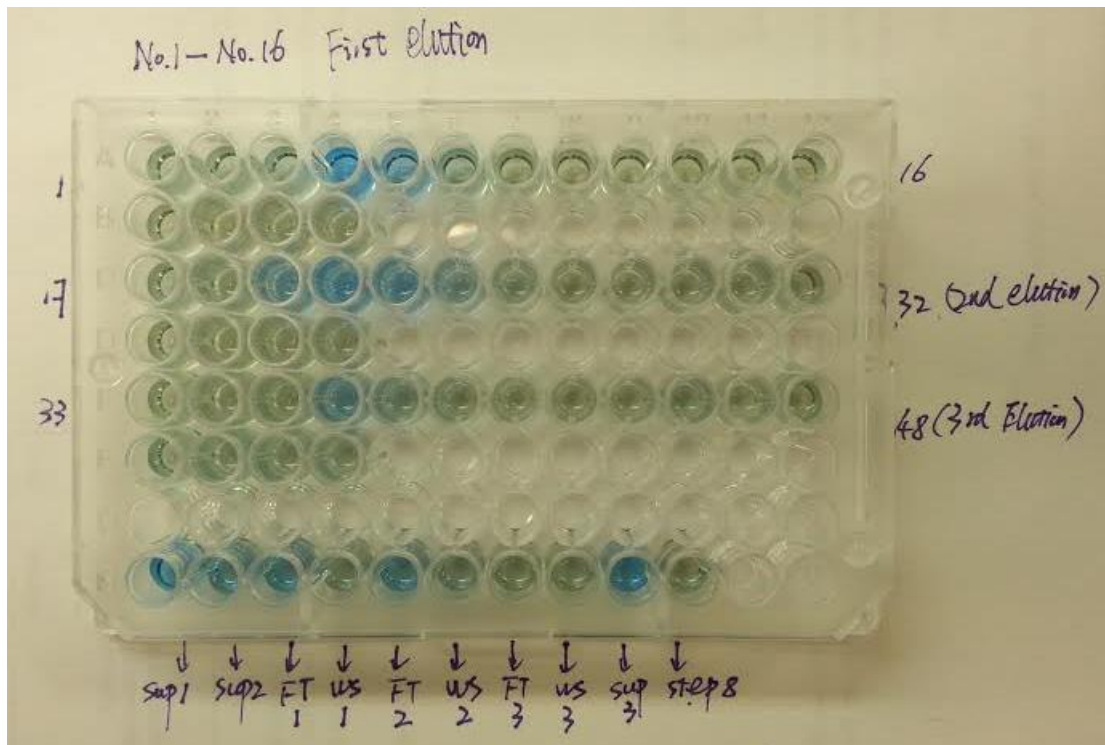


Figure 2.2: An ULTRA-Bradford reagent test tells you which elution fractions contain more protein (darker blue = higher protein concentration).

The elution fractions are run on a SDS-PAGE protein gel to confirm that LamB is present and purified. The resulting gel should look like this:

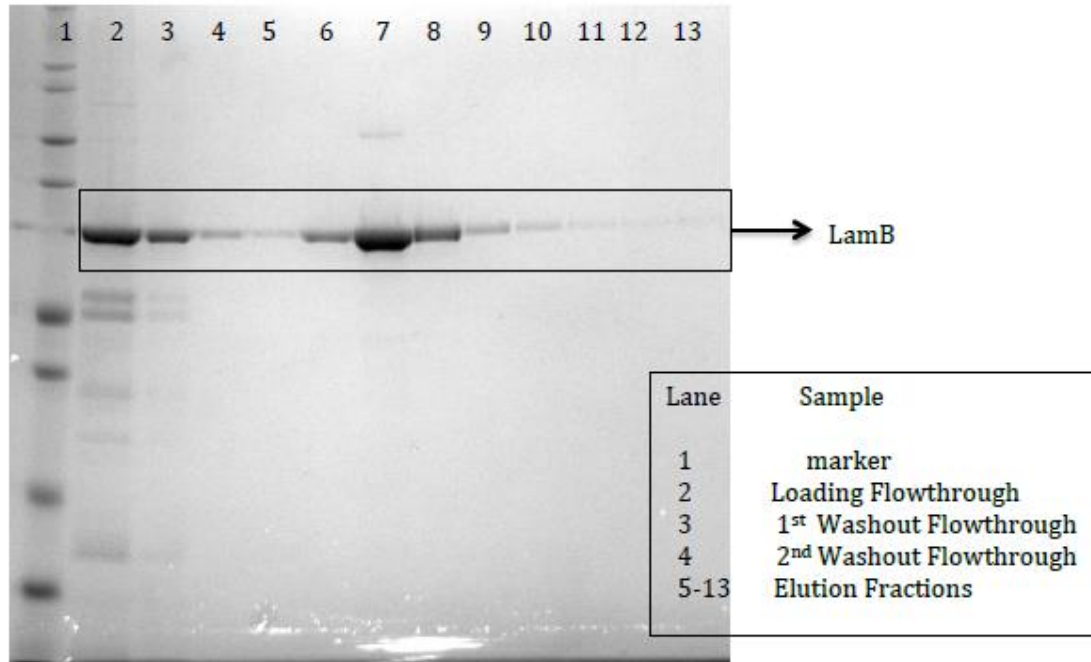


Figure 2.3: The SDS-PAGE gel is used to verify that a protein of the appropriate size (160kDa) is obtained and that it is relatively pure in solution (no other strong bands).

- 8) Finally, the most concentrated elution fractions are combined and further concentrated via membrane centrifugation, then dialyzed in TM buffer + 1% oPOE for future experimental use. The protein concentration is quantified via UV absorbance measurements.

2.2 Herpes Simplex Virus Type - 1

The human herpes simplex virus type-1 (HSV-1) is the model system for the atomic force microscopy experiments documented in this thesis. More than 130 unique herpesviruses have been identified, with hosts ranging from mammal to mollusk¹². Nine of these herpesviruses are human pathogens, including herpes simplex virus 1 and 2 (HSV-1 and HSV-2). HSV-1, which can cause both orolabial and genital herpes, plagues about 60% of American adults¹³ and is nearly universal in developing countries¹⁴. Structure is conserved within the herpesvirus family, with all viruses composed of a double-stranded DNA (dsDNA) genome encased in a strong protein shell called the capsid¹⁵. This strong structural conservation between different herpesviruses suggests that the physical mechanisms of viral function may also be conserved within this viral family. Therefore HSV-1 has been widely used as an experimental model to study the physical properties of all herpesviruses.

2.2.1 Genetic and structural characteristics of HSV-1

HSV-1 consists of a 152kbp dsDNA genome¹⁶ packaged within a 120nm diameter capsid which is coated with tegument proteins and enveloped in a lipid membrane. The mature HSV-1 capsid is comprised of seven proteins: VP5, VP19C, VP23, VP26, and the proteins encoded by the genes UL25, UL17 and UL6 (hereafter, gene names will be used to refer to their respective proteins). VP5 is the major capsid protein and the structural subunit of the capsid building blocks called capsomeres. The capsid is self-assembled through tiling of 150 hexons (six copies of VP5, each decorated with one copy of VP26, or pUL36, at the tip) and 12 pentons (five copies of VP5) into an icosahedral shell¹⁷⁻¹⁸. These capsomeres are connected by 320 triplexes, which are heterodimers with one copy of VP19C and two copies of VP23¹⁷. This combination of pentons and hexons creates the icosahedral shape of the capsid, with six five-fold, ten three-fold, and fifteen two-fold rotation axes. Each of the twelve points of five-fold symmetry are marked by pentons, and one of these vertices is also occupied by the portal (12 copies of pUL6) through which viral DNA is packaged¹⁹. The pentons are each externally bound to the capsid vertex-specific component (CVSC), which is five copies of a heterodimer consisting of one copy each of pUL25 and pUL17²⁰⁻²¹. The component proteins are illustrated in a color-coded cross-section of a cryo-EM micrograph (cryo-EM map deposited as EMD-6386²²) in Figure 2.4.

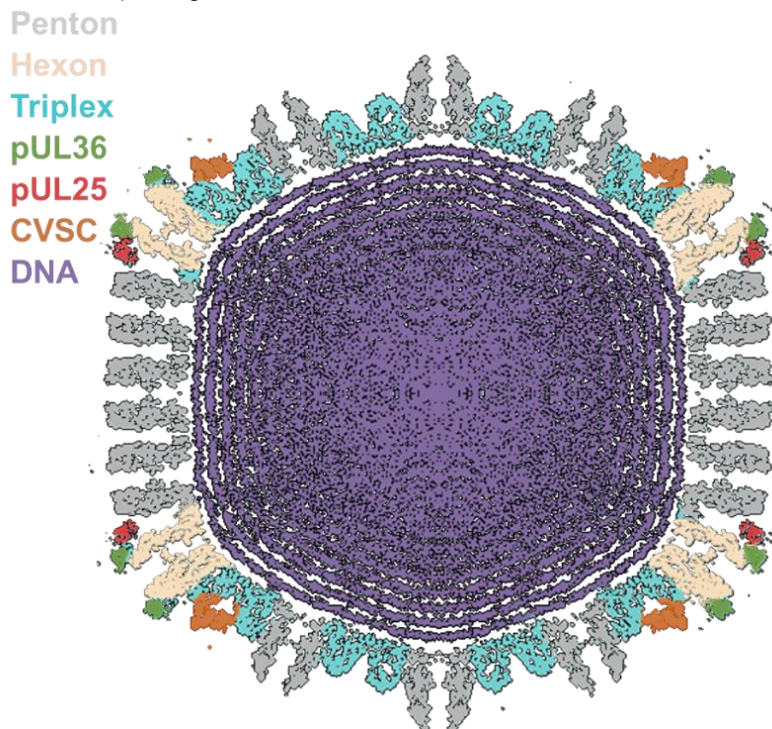


Figure 2.4: The HSV-1 capsid, as presented²² in this cryo-EM 3D reconstruction, is comprised of 150 hexons (6 copies of the major capsid protein VP5), 12 pentons (5 copies of VP5), 320 triplex proteins, and about 60 copies each of pUL38 (adorning copies of VP5 in pentons), pUL17 (part of the CVSC), and pUL25 (part of the CVSC).

2.2.2 Purification of HSV-1 capsids

To purify HSV-1 capsids, you must start by growing cultures of African green monkey kidney cells (typically called Vero cells) which will eventually be infected with HSV-1 to produce capsids. These cells are grown in Dulbecco's modified Eagle's medium with 5% fetal bovine serum and 5% penicillin/streptomycin until they are confluent (that is, until they coat the surface they are grown on with 100% coverage). The confluent cells are infected with HSV-1 virions (either the wild type, typically called KOS, strain or the mutants described in detail in Chapter 4) at a multiplicity of infection of 5 infectious particles per Vero cell. This infection stalls the growth of the cells because the virus overtakes the cellular reproductive machinery to produce new viruses. The infection proceeds for about a day before the cells begin to “round up” or show the “cytopathic effect” – that is, the cells transition from healthy cells (attached to the surface and oblong in appearance) to unhealthy cells (pulling away from the surface and spherical in appearance) as illustrated in Figure 2.5 below (published by Macedo, et al ²³).

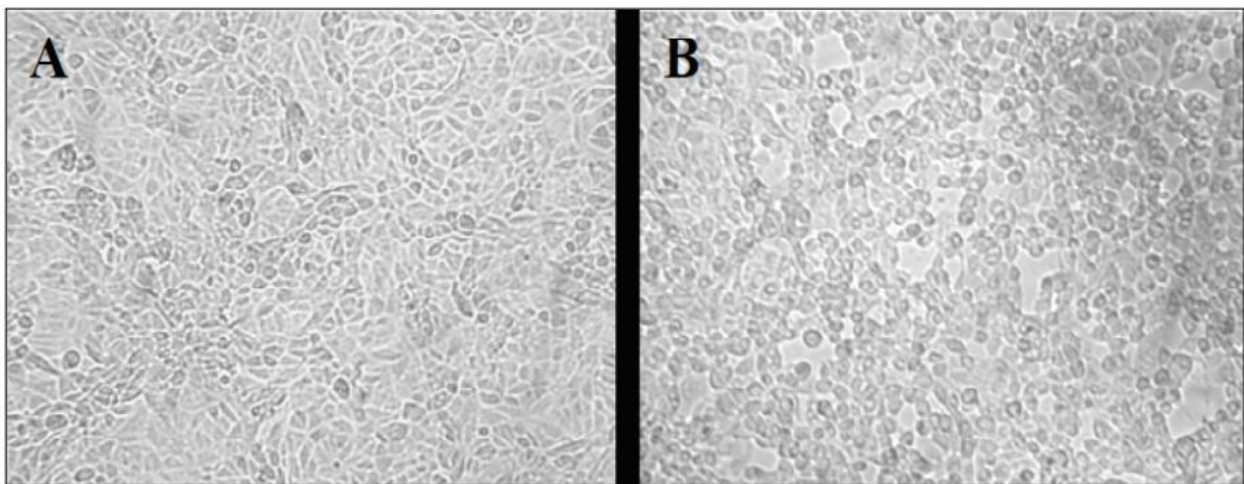


Figure 2.5: Healthy Vero cells are firmly attached to the substrate and appear oblong (A) while HSV-1 infected Vero cells which have already produced many progeny capsids inside the cells become spherical and pull away from the surface (B). Image was published by Macedo et al²³.

At this point, cells are scraped into solution and centrifuged so a cell pellet can be isolated. The cell pellet is then resuspended (in HLB, or hypertonic lysis buffer, a low-salt solution which swells the cells) and lysed by addition of a gentle detergent (0.5% NP-40 Substitute). Lysis ruptures the cell membrane and releases cell nuclei, as well as a lot of cell debris, into solution. The solution is again centrifuged to pellet the nuclei while leaving smaller cell debris in the supernatant. The nuclei pellet is resuspended in a high

salt TNE buffer (10 mM Tris, 500mM NaCl, 1 mM EDTA) with protease inhibitor cocktail – this sets up an environment that capsids can be released into without risk of degradation or rupture. The nuclear membranes are disrupted by gentle sonication to release nuclear capsids into solution, then large nuclear debris was cleared by brief centrifugation (debris is pelleted while the lighter capsids stay in supernatant). The capsid-rich supernatant is collected and underlaid with a cushion (35% sucrose in TNE), then ultracentrifuged – this step allows the capsids to pass through the cushion, but smaller cellular debris is caught at the sucrose interface. The capsid pellet is resuspended, loaded onto a 20–50% (w/w) TNE sucrose gradient, and ultracentrifuged to separate the A-, B-, and C- (if formed) capsids. Since A-, B-, and C- capsids have sufficiently distinct masses they migrate to different points in the sucrose gradient, as illustrated in Figure 2.6.

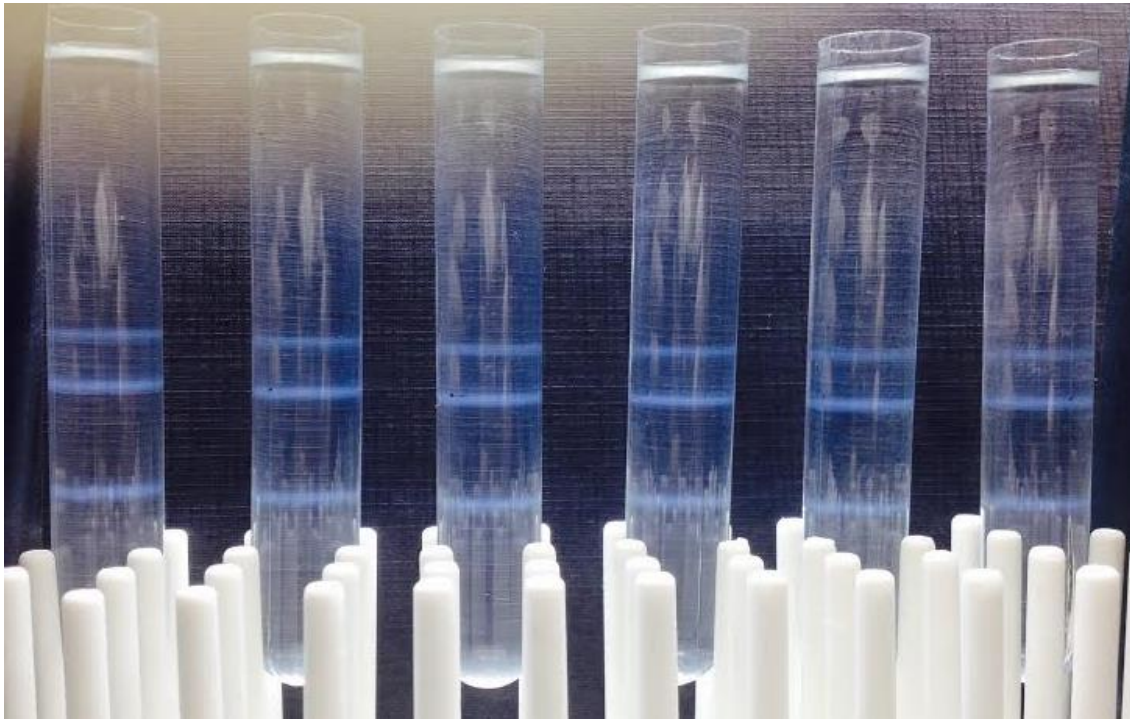


Figure 2.6: Sucrose gradients are used to separate A-, B- and C- capsids (top, middle, and bottom bands, respectively). After spinning, the bands are extracted and spun down to yield concentrated solutions of pure A-, B-, and C- capsids.

The A-, B-, and C-capsid bands are isolated by puncturing the side of the centrifuge tube with a needle and syringe and extracting each band. The extractions are diluted 10-fold in TNE buffer (to allow capsids to pellet out of the sucrose) and ultracentrifuged again to form a purified capsid pellet. Capsids are resuspended in TNE and stored at 4°C for further use.

2.2.3 UL25 protein expression and purification

An assay for the expression of the UL25 protein was developed in Dr. Fred Homa's laboratory. In short, a plasmid encoding the UL25 gene (which expresses the UL25 protein) was inserted into e coli. The e coli was cultured and then induced to express UL25 by the addition of IPTG, which triggers transcription of the lac operon (the lac operator controls the UL25 gene and thus triggering lac operon transcription also triggers expression of the UL25 protein). The cells were pelleted, then ruptured with a freeze-thaw cycle, resuspension in lysis buffer, and gentle sonication. The soluble proteins in the cell lysate are then harvested by centrifugation (insoluble portions of the cell lysate clump together into large structures which pellet, while the soluble portions stay in the supernatant). The UL25 protein is purified from the solution of soluble proteins by nickel resin purification (using HisPur Ni-NTA Resin). The supernatant (containing a variety of soluble proteins and cellular contaminants) is mixed with the resin, incubated, then washed several times; UL25 proteins bind strongly to the resin while other nonspecific proteins and contaminants are washed away. The UL25 protein is removed from the resin by adding a large concentration of Imidazole, which has a very high binding affinity for the resin and out-competes the UL25 protein for access to binding sites. Finally, the column is washed to remove the unbound UL25, which is collected and run on a gel to test its purity and estimate its concentration (Figure 2.7).

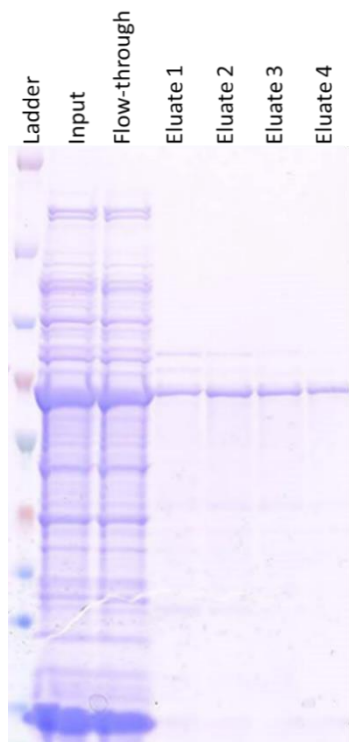


Figure 2.7: After purification, the UL25 protein is run on a NuPAGE protein gel to check for the correct protein size and acceptable level of purity. A protein standard like BSA in known concentrations is also run on the gel for estimation of protein concentration.

2.2.4 UL25 binding reaction

Binding reactions were prepared for the AFM study of the mechanism of mechanical reinforcement by the UL25 protein. To prepare these samples, UL25-null capsids (produced as described above, using HSV-1 strain FH439 which is a UL25 deletion mutant) were incubated with varying amounts of purified UL25 protein at room temperature for 90 minutes in PBS buffer (1.37 M NaCl, 27 mM KCl, 43 mM Na₂HPO₄·7H₂O, 14 mM KH₂PO₄). This binding reaction was then purified and unbound UL25 protein removed by ultracentrifugation in a 20-50% (w/w) TNE sucrose gradient. The protein-bound capsids collected in a band which was harvested by side puncture, diluted in TNE buffer and ultracentrifuged again to pellet the capsids. Capsids were resuspended in TNE and stored at 4°C for further experimental use.

References

1. Lederberg, E., "Lysogenicity in Escherichia Coli K-12". **1951**.
2. Travis, J., All the World's a Phage-Viruses That Eat Bacteria Abound--and Surprise. *Science News* **2003**, *164*, 26-28.
3. Hatfull, G. F., Bacteriophage Genomics. *Current opinion in microbiology* **2008**, *11*, 447-453.
4. Evilevitch, A.; Lavelle, L.; Knobler, C. M.; Raspaud, E.; Gelbart, W. M., Osmotic Pressure Inhibition of DNA Ejection from Phage. *Proc Natl Acad Sci U S A* **2003**, *100*, 9292-9295.
5. Rajagopala, S. V.; Casjens, S.; Uetz, P., The Protein Interaction Map of Bacteriophage Lambda. *BMC microbiology* **2011**, *11*, 213.
6. Dale, J. W.; Greenaway, P. J., Preparation and Assay of Phage Lambda. In *Nucleic Acids*, Walker, J. M., Ed. Humana Press: Totowa, NJ, 1984; pp 201-209.
7. Juckles, I., Fractionation of Proteins and Viruses with Polyethylene Glycol. *Biochimica et Biophysica Acta (BBA)-Protein Structure* **1971**, *229*, 535-546.
8. Randall-Hazelbauer, L.; Schwartz, M., Isolation of the Bacteriophage Lambda Receptor from Escherichia Coli. *Journal of bacteriology* **1973**, *116*, 1436-1446.
9. Berkane, E.; Orlik, F.; Stegmeier, J. F.; Charbit, A.; Winterhalter, M.; Benz, R., Interaction of Bacteriophage Lambda with Its Cell Surface Receptor: An in Vitro Study of Binding of the Viral Tail Protein GpJ to Lamb (Maltoporin). *Biochemistry* **2006**, *45*, 2708-2720.
10. Luckey, M.; Nikaïdo, H., Specificity of Diffusion Channels Produced by Lambda Phage Receptor Protein of Escherichia Coli. *Proceedings of the National Academy of Sciences* **1980**, *77*, 167-171.
11. Ivanovska, I.; Wuite, G.; Jonsson, B.; Evilevitch, A., Internal DNA Pressure Modifies Stability of Wt Phage. *Proc Natl Acad Sci U S A* **2007**, *104*, 9603-9608.
12. Davison, A. J.; Eberle, R.; Ehlers, B.; Hayward, G. S.; McGeoch, D. J.; Minson, A. C.; Pellett, P. E.; Roizman, B.; Studdert, M. J.; Thiry, E., The Order Herpesvirales. *Arch Virol* **2009**, *154*, 171-177.
13. Xu, F.; Schillinger, J. A.; Sternberg, M. R.; Johnson, R. E.; Lee, F. K.; Nahmias, A. J.; Markowitz, L. E., Seroprevalence and Coinfection with Herpes Simplex Virus Type 1 and Type 2 in the United States, 1988-1994. *The Journal of Infectious Diseases* **2002**, *185*, 1019-1024.
14. Whitley, R. J.; Kimberlin, D. W.; Roizman, B., Herpes Simplex Viruses. *Clinical Infectious Diseases* **1998**, *26*, 541-555.
15. Brown, J. C.; Newcomb, W. W., Herpesvirus Capsid Assembly: Insights from Structural Analysis. *Curr Opin Virol* **2011**, *1*, 142-149.
16. Macdonald, S. J.; Mostafa, H. H.; Morrison, L. A.; Davido, D. J., Genome Sequence of Herpes Simplex Virus 1 Strain Kos. *Journal of virology* **2012**, *86*, 6371-6372.
17. Newcomb, W. W.; Trus, B. L.; Booy, F. P.; Steven, A. C.; Wall, J. S.; Brown, J. C., Structure of the Herpes Simplex Virus Capsid. Molecular Composition of the Pentons and the Triplexes. *Journal of molecular biology* **1993**, *232*, 499-511.
18. Zhou, Z. H.; Dougherty, M.; Jakana, J.; He, J.; Rixon, F. J.; Chiu, W., Seeing the Herpesvirus Capsid at 8.5 Å. *Science* **2000**, *288*, 877-880.
19. Padeloup, D.; Blondel, D.; Isidro, A. L.; Rixon, F. J., Herpesvirus Capsid Association with the Nuclear Pore Complex and Viral DNA Release Involve the Nucleoporin Can/Nup214 and the Capsid Protein Pul25. *Journal of virology* **2009**, *83*, 6610-6623.
20. Trus, B. L.; Newcomb, W. W.; Cheng, N.; Cardone, G.; Marekov, L.; Homa, F. L.; Brown, J. C.; Steven, A. C., Allosteric Signaling and a Nuclear Exit Strategy: Binding of UI25/UI17 Heterodimers to DNA-Filled Hsv-1 Capsids. *Mol Cell* **2007**, *26*, 479-489.
21. Cockrell, S. K.; Huffman, J. B.; Toropova, K.; Conway, J. F.; Homa, F. L., Residues of the UI25 Protein of Herpes Simplex Virus That Are Required for Its Stable Interaction with Capsids. *J Virol* **2011**, *85*, 4875-4887.
22. Huet, A.; Makhov, A. M.; Huffman, J. B.; Vos, M.; Homa, F. L.; Conway, J. F., Extensive Subunit Contacts Underpin Herpesvirus Capsid Stability and Interior-to-Exterior Allostery. *Nature structural & molecular biology* **2016**.
23. Macedo, N. R. P. V.; Ribeiro, M. S.; Villaça, R. C.; Ferreira, W.; Pinto, A. M.; Teixeira, V. L.; Cirne-Santos, C.; Paixão, I. C.; Giongo, V., Caulerpin as a Potential Antiviral Drug against Herpes Simplex Virus Type 1. *Revista Brasileira de Farmacognosia* **2012**, *22*, 861-867.

Chapter 3: Experimental Methods

3.1 Light scattering

Light scattering (LS) was the heart of the DNA ejection dynamics experiments presented in this thesis. LS is a non-invasive technique capable of measuring *in situ* particle size, structure, molecular weight, aspect ratio, and more. There are two main types of light scattering experiments: dynamic and static. The experiments for this thesis research included physical characterization with dynamic light scattering (DLS) and static light scattering (SLS) as well as quantification of viral population dynamics with detailed time-resolved measurements of intensity. In all cases, a low concentration (10^{11} particles per mL) of phage λ was prepared in an aqueous solution and filtered into a cylindrical glass LS cell. A polarized Argon ion laser was directed onto the sample, where it scattered off the phage particles in solution. The scattered light was detected by using a goniometer to swing a photomultiplier tube to a wide range of scattering angles.

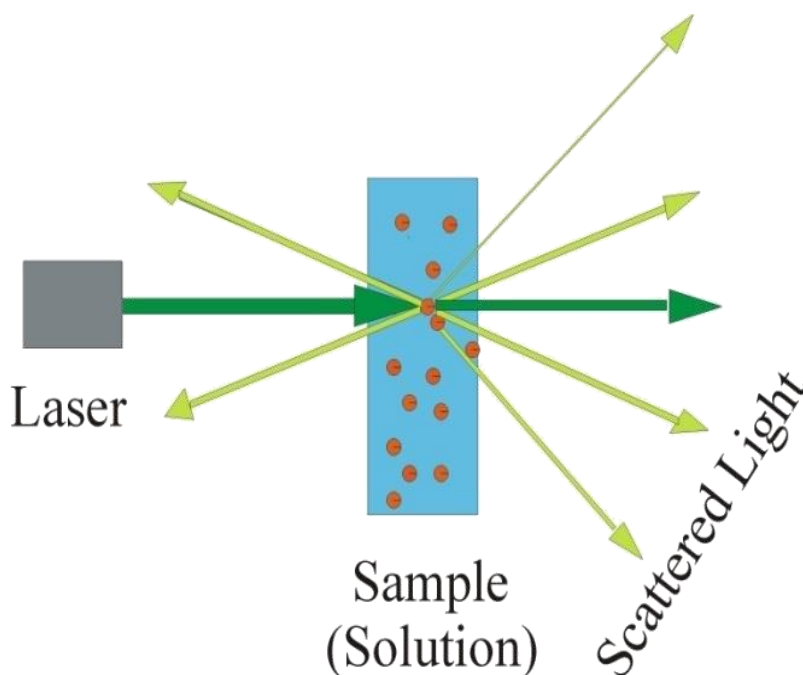


Figure 3.1: A simplified cartoon of light scattering shows that the laser hits the solution and scatters when it hits particles. The motion of the particles coming in and out of the laser beam causes intensity fluctuations – these fluctuations can be seen with the naked eye as flickering of the scattered light projected onto a screen, and can also be measured with a detector as in DLS. The angular dependence of the scattered light signal can also be informative.

3.1.1 Dynamic light scattering

Dynamic light scattering (DLS) tracks fluctuations in scattered light intensity as a function of time; in equilibrium systems, these fluctuations are caused by particles moving in and out of the laser's path due to Brownian motion. For small, monodisperse, spherical particles in dilute solution, Brownian motion is described theoretically with the Stokes-Einstein equation: $D = \frac{k_B T}{6\pi\eta R}$, where D is the diffusion coefficient, $k_B T$ is thermal energy, η is viscosity and R is particle radius. Thus, small particles have a larger diffusion coefficient and move in and out of the laser beam more frequently, leading to more rapid intensity fluctuations in a DLS experiment. Similarly, large particles move slower and have less rapid scattered intensity fluctuations (see Figure 3.2).

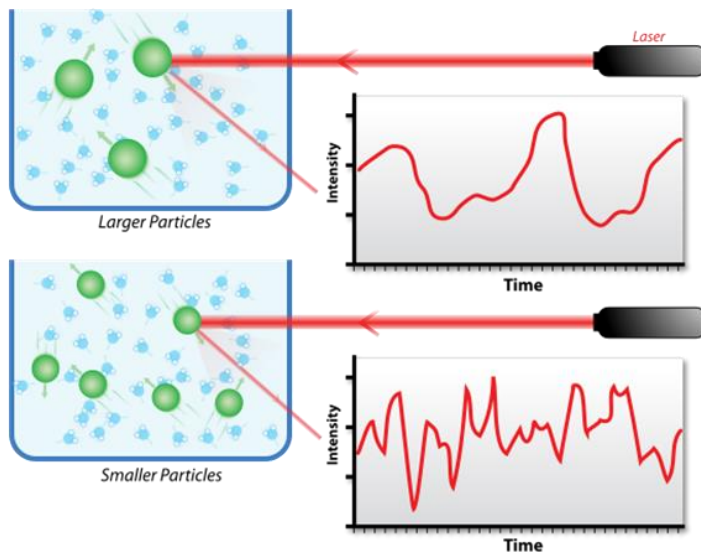


Figure 3.2: The size of particles dictates particle speed and thus the rate of fluctuations in scattered light intensity. These fluctuations are measured and processed into correlation functions, which are fit and analyzed to yield particle characteristics in a DLS experiment. Cartoon originally appears at:

https://en.wikipedia.org/wiki/Dynamic_light_scattering

The measured time-dependent intensity fluctuations are processed to yield an “intensity-intensity correlation function”, $g^{(2)}(q, \tau) = \int_0^T I(q, t)I(q, t + \tau)dt$, which correlates the intensity at time t with that a short time τ later. The “field correlation function” $g^{(1)}(q, \tau)$ is computed using the Siegert equation, $g^{(2)}(q, \tau) = 1 + |g^{(1)}(q, \tau)|^2$ and fit¹ to the sum of stretched exponentials, $g^{(1)}(q, \tau) = \sum_{i=1}^N A_i e^{(-\Gamma_i \tau)^{\beta_i}}$, where A_i , Γ_i , and β_i are the amplitude, decay rate and stretching parameter of the i -th mode, with N being the number of modes (there is a “mode” for each type of particle in the solution). The measured decay rate, Γ , depends strongly on the scattering vector or momentum transfer vector, $q = \frac{4\pi n}{\lambda} \sin(\theta/2)$ (where n is the index of refraction, λ is the laser wavelength, and θ is the scattering angle), and the particle diffusion coefficient, D : $\Gamma = Dq^2$.

Measuring the dynamics at a range of angles allows for rigorous measurement of D and thus, from the Stokes-Einstein equation mentioned above, an estimate of the hydrodynamic radii R_h of all particles present in the solution; such data is presented in Figure 3.3 for LamB and phage λ together in solution.

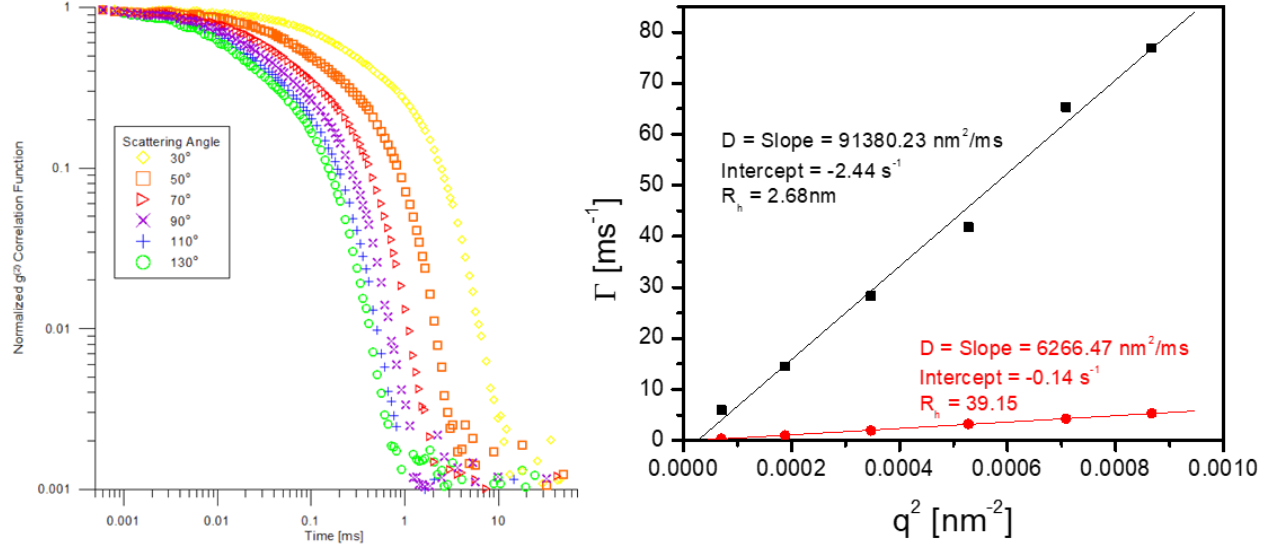


Figure 3.3: DLS measurements of phage λ and solubilized LamB receptor protein result in bimodal correlation functions as in the graph on the left (the weaker fast mode is caused by the smaller receptor complexes while the main mode is the phage λ particles). When analyzed, these correlation functions yield decay rates (Γ) for both particle species. Size estimates are made by plotting Γ vs q^2 , as in the plot on the right, and extracting the diffusion coefficient. The estimated hydrodynamic radius is larger than the physical capsid radius; this is likely due to hydrodynamic drag (which is accentuated by the long phage tail).

3.1.2 Static light scattering

Static light scattering (SLS), unlike DLS, neglects the intensity fluctuations and instead measures average intensity over a period of time. Typically, SLS is done over a wide range of angles and sample concentrations. When both dependences are plotted together, in what is called a Zimm plot, one can extract values for particle molecular weight (M_w), radius of gyration (R_g), and second virial coefficient (A_2). The analysis is theoretically based on the Rayleigh-Gans-Debye approximation of the Zimm equation²: $\frac{KC}{R} =$

$$\frac{1}{M_w} \left(1 + \frac{(qR_g)^2}{3} \right) + 2A_2c, \text{ where } c \text{ is the concentration of particles in the solution, } A_2 \text{ is the second virial}$$

coefficient, $K = \frac{4\pi^2 n_0^2 \left(\frac{dn}{dc} \right)^2}{N_A \lambda^4}$ is the optical constant [n_0 is index of refraction, dn/dc is refractive index

increment, N_A is Avogadro's number, and λ is wavelength] and $R(\theta) = R_{std} \frac{I(\theta)_{sol} - I(\theta)_{soln}}{I(\theta)_{std}} \left(\frac{n_{soln}}{n_{std}} \right)^2$ the excess

Rayleigh Ratio [R_{std} is the Rayleigh ratio of the standard (carbon disulfide), $I(\theta)$ is the intensity of solution, solvent, or standard, and n is the index of refraction of solvent or standard]. By measuring average intensity at a series of concentrations and scattering angles, then extrapolating to $c = 0$ and $q = 0$, one can reliably measure R_g , M_w , and A_2 . When average intensity has been measured at a range of scattering angles, but only at a single concentration (assumed to be sufficiently dilute that the interactions governed by A_2 are negligible), the data is plotted as $Kc/R \propto 1/I$ versus q^2 . This partial Zimm plot is fit to a straight line and radius of gyration, R_g , is obtained by $R_g = \sqrt{\frac{3 \times \text{slope}}{\text{intercept}}}$. Such an experiment is shown for phage λ before DNA ejection in Figure 3.4, where $R_g = 30.7\text{nm}$ is measured. This result, together with the measured R_h value from multi-angle DLS, confirms the approximately spherical symmetry of the capsid (the measured ratio of $R_g/R_h = 0.784$ closely matches the 0.778 ratio predicted for hard spheres).

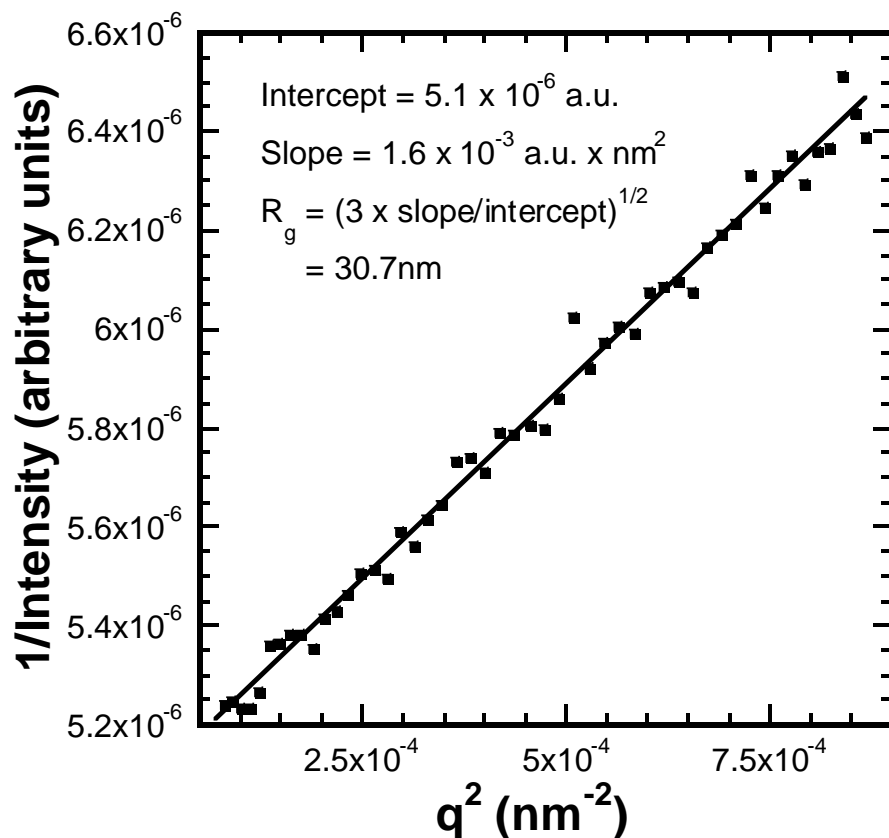


Figure 3.4: A partial Zimm plot (with only scattering angle-dependence, not concentration dependence or even an accurately measured optical constant K) is sufficient to measure the radius of gyration, R_g , of phage particles in solution.

3.1.3 DNA ejection dynamics experiments

The DNA ejection dynamics experiments could not be accurately described as either DLS or SLS; the detector was fixed at a specified scattering angle to track average intensity as a function of time for 100 minutes after triggering viral DNA ejection. To perform a dynamics experiment, a phage solution was filtered into the scattering cell and equilibrated at the desired temperature for about 30 minutes. Once the intensity signal was sufficiently stable, the sample was briefly removed to mix in a small volume of concentrated LamB solution (such that λ :LamB = 1:100 to ensure rapid binding). This mixture was gently mixed for ~10s with a low-speed vortex, then reinserted into the experimental apparatus and monitored for the next 100 minutes. The time resolution was 1.2s. The experiment and a typical measurement are depicted in Figure 3.5 below.

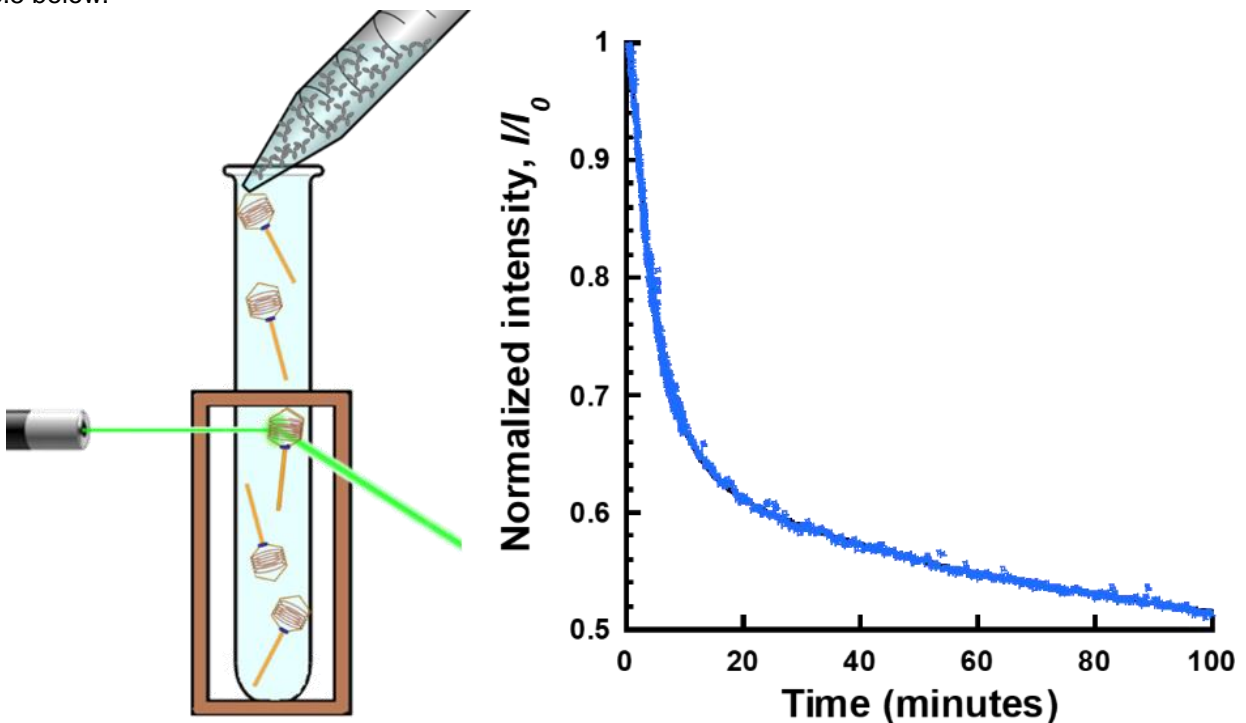


Figure 3.5: At time 0, purified receptor proteins are added to the phage sample to trigger ejection. The resulting drop in intensity is tracked with fine temporal resolution for 100 minutes to measure viral DNA ejection dynamics.

3.1.4 The choice of angle in DNA ejection dynamics experiments

The experimental scattering angle was fixed at 120° . This scattering angle was chosen to improve the ejection dynamics signal-to-noise ratio by rapidly reducing the contribution to scattered intensity of ejected DNA. In LS experiments, if the scattering particles are sufficiently small ($qR_g < 1$, this is called the Guinier regime), the scattered light intensity scales² like $I \propto 1/[1+(qR_g)^2/3]$ (this comes from rearranging

the Zimm equation mentioned above, $\frac{Kc}{R} = \frac{1}{M_W} \left(1 + \frac{(qR_g)^2}{3} \right) + 2A_2c$, where $Kc/R \propto 1/I$). If molecular weight remains the same, but the size of particles grows such that $qR_g > 1$ (as is the case of ejected and relaxing DNA), the scattering drops off sharply as the denominator rapidly grows³. In these experiments, the scattering angle of 120° was chosen to take advantage of this sharp dropoff as soon as DNA is ejected. That is, encapsidated DNA ($R_g = 30.7\text{nm}$) has $qR_g = 0.86$, keeping it safely within, but near, the $qR_g < 1$ cutoff for the Guinier regime. However, upon ejection the DNA expands – when it has expanded to just $R_g \sim 35\text{nm}$, $qR_g = 1$ and the light intensity scattered from the particle has dropped to 95% compared to the encapsidated DNA scattering intensity. When the DNA has diffused to $R_g \sim 100\text{nm}$, its scattered light intensity has dropped to 30% relative to the encapsidated DNA value. By the time the DNA is fully relaxed, with $R_g \sim 1000\text{nm}$, the scattering intensity is negligible.

If a smaller scattering angle, say 30° or 60° for example, had been chosen instead of 120°, the transition out of the Guinier scattering regime (when $qR_g = 1$) would be delayed until the ejected DNA reached a correspondingly larger R_g value. That is, the ejected DNA would contribute significantly for a longer period of time after the ejection event (see Figure 3.6). In this way, the chosen angle of 120° aids in quickly reducing the signal from ejected DNA and therefore maximizing the rapid change in signal as phages transition from DNA-filled to empty.

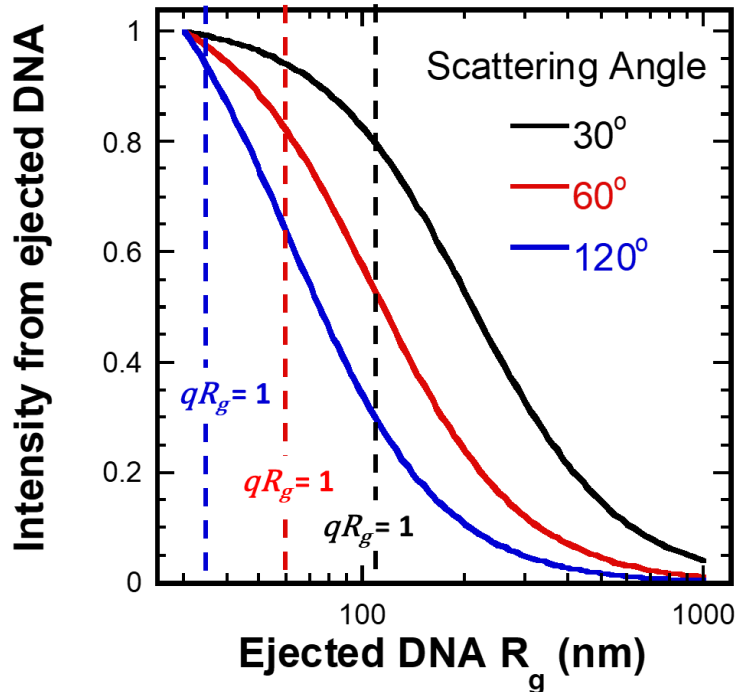


Figure 3.6: When qR_g transitions from less than to greater than 1, the scattered light intensity, which scales as $I \propto 1/[1+(qR_g)^2/3]$, begins to drop off much more sharply as the denominator grows. For this reason, the scattering angle of 120° was chosen; at this angle the drop in intensity caused by the transition out of the Guinier scattering begins at a DNA radius of $\sim 35\text{nm}$. Compared to scattering angles of 60° or 30° (where the Guinier scattering regime extends to $\sim 60\text{nm}$ or $\sim 120\text{nm}$, respectively), the experimental angle of 120° reduces more quickly the signal from ejected DNA, allowing the experiments to focus on the dynamics of ejection initiation.

3.1.5 Dynamics curve normalization and analysis

The ejection dynamics data required careful normalization and analysis to compare across different temperatures and genome lengths. We first normalized the time-dependent intensity by the initial intensity value, and fit that data to a biexponential function plus a constant: $I_{norm}(t) = I(t)/I(0) = b + A_1 \exp(-t/\tau_{fast}) + A_2 \exp(-t/\tau_{slow})$, where $b + A_1 + A_2 = 1$. Using the b baseline value obtained from the fit, we re-normalized the intensity data by $I_{1 \rightarrow 0}(t) = (I_{norm}(t) - b)/(1 - b)$ such that the intensity curves all stretched from 1 (initial intensity) to 0 (fitted baseline value). Such treatment ensures that all curves reflect the dynamics of the full population of phages in the sample transitioning from DNA-filled to empty, even in cases (such as low temperature) where the complete transition was not fully observed after 100 minutes.

Final analysis of the fully normalized curves is done by fitting to another biexponential curve, $I_{1 \rightarrow 0} = A \exp(-t/\tau_{fast}) + (1 - A) \exp(-t/\tau_{slow})$, which yields time constants for a faster and a slower process present in the experiment. An example of the LS data, with the fits described above, is shown in Figure 3.7 below. This plot is presented on a semi-log scale to illustrate the biexponential nature of the measured dynamics curves.

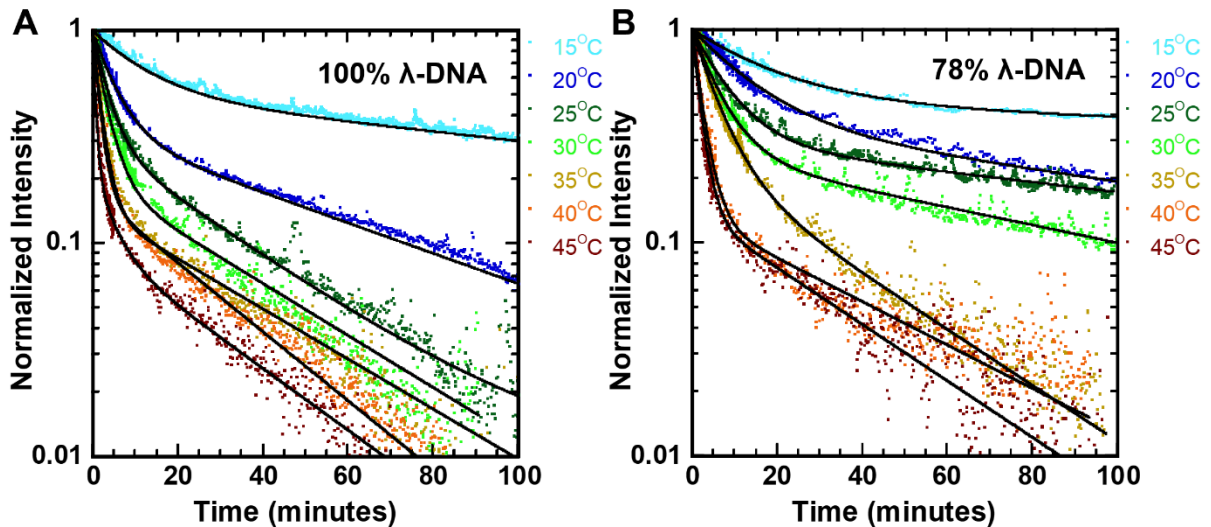


Figure 3.7: LS ejection dynamics curves are bi-exponential, as shown in these semi-log plots for 100% and 78% λ -DNA phages. Linear plots are displayed in Chapter 4.

The two time constants obtained from the fits described above are separated by about a factor of 4 through most of the temperature range. In Chapter 4, I present evidence that the slower process, with

$\tau_{slow} \sim 30$ minutes, corresponds to the relaxation and diffusion of ejected DNA. As described in the previous section, this ejected DNA does contribute significantly to the scattered intensity until it has diffused sufficiently. However, in this thesis I focus largely on the much faster intensity decay process (described in the equation above by τ_{fast}). This process corresponds⁴ to the average lag-time before initiation of a stochastic DNA ejection event. This τ_{fast} can be converted into the more intuitive half-life, $\tau_{1/2} = \ln(2) \times \tau_{fast}$, a quantity describing the time necessary for half of the phages in the solution to eject their DNA. The dependences of τ_{fast} and half-life will be discussed in great detail in Chapter 4.

3.1.6 LS system and sample details

Light scattering experiments were performed on a home built system (PI K. Streletzky, Cleveland State University) by directing a beam of 1W Argon Ion laser (wavelength $\lambda = 514.5\text{nm}$, Spectra-Physics 2017) into a Brookhaven Instruments setup comprised of a goniometer (BI-200SM), photomultiplier (BI-DS2) and correlator (BI-9000)¹. Both incident and measured scattered light were vertically polarized, as ensured by a Glan-Laser calcite polarizer (Thorlabs, GL10) and a Precision Linear Polarizer (Newport 20LP-VIS-B). Light scattering samples were prepared by diluting bacteriophage λ stock to 1.2×10^{11} pfu/mL in a 1.2mL volume of TM+1% oPOE buffer. This diluted phage sample was filtered (0.2 μm polycarbonate filter, Whatman) directly into a pre-cleaned⁵ glass cell then incubated for at least 10 minutes in the temperature controlled sample holder, which was maintained within 0.1°C by a Neslab RTE-110 water bath, heat exchange coils, and a decalin-filled quartz vat that surrounds the sample cell.

3.2 Small angle scattering

The LS ejection dynamics experiments were supported by time-resolved small angle x-ray scattering experiments. The intensity at low q values can be directly compared with LS intensity results, but the results can also provide additional information about the number and structure of the particles in the sample. While not directly related to the experimental results discussed here, I have also put significant efforts into understanding the theory predicting small angle scattering (SAS) intensity curves from viruses. As a result, I have produced scattering models in varying degrees of detail. Therefore, in addition to using this section to describe the experimental setup and analysis for the SAXS ejection dynamics project described in Chapter 4, I will also summarize my modelling efforts and ideas.

3.2.1 Introduction to small angle scattering

Due to their monodisperse nature, nanometer-scale features, and liquid-crystalline DNA density, viruses make a wonderful system to study with small angle scattering. For example, the tight packing of DNA into capsids results in a small DNA-DNA interaxial spacing (as discussed in greater detail in Chapter 1). This spacing can be experimentally measured by analyzing the DNA diffraction peak observable with small-angle x-ray scattering (SAXS). This concept is illustrated in Figure 3.8 from Sae-Ueng et al, who measured the position and area of the DNA diffraction peak at a range of temperatures.

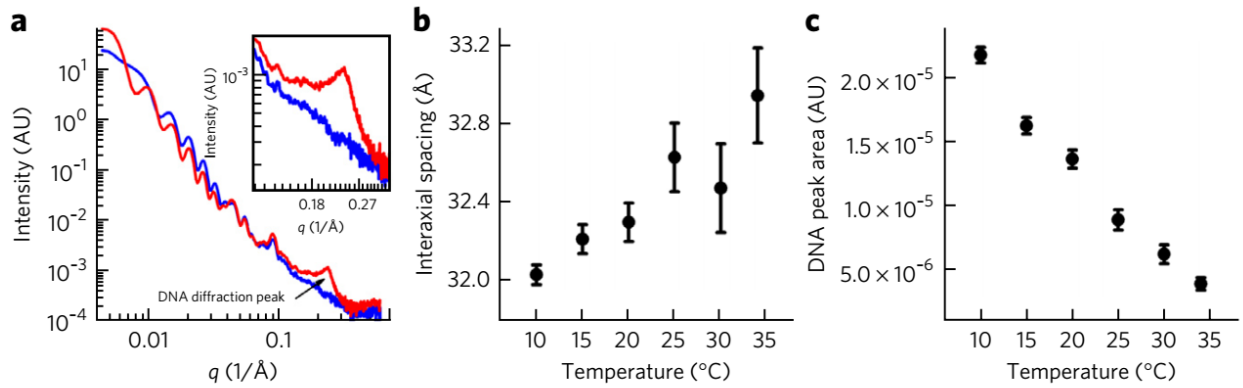


Figure 3.8: An example⁶ of the power of small angle scattering – it is able to resolve the diffraction peak caused by ordered layers of DNA within an HSV-1 capsid. This peak can be quantified by fitting it to a peak function and extracting the peak position, area, and width.

In addition to giving information about the DNA spacing, small angle scattering techniques can also provide information about the overall size of a viral particle (assuming a spherical shape) and whether or not it contains DNA (this can be determined even if the scattering intensity is insufficient to resolve the DNA diffraction peak). These physical properties are reflected in a scattering vector (q , with the same definition as in the LS sections above) dependent quantity called the form factor, $P(q)$. The form factor can be calculated from the electron density of the particles in the sample, $\rho(r)$, by $P(q) = \int \rho(r)e^{iq \cdot r} d^3r$. It is related to the scattering intensity, $I(q) = P(q) * S(q)$, where $S(q)$ is the structure factor. The structure factor is related³ to interactions between particles, and for dilute hard-spheres (like the viruses in this experiment) it is essentially equal to 1.

Therefore the q - dependence of the small angle scattering dependence can be predicted by mathematically describing the electron density of the virus and solving the integral equation for the form factor. The electron density, conveniently, can be constructed by considering the results of 3D cryo-EM

reconstructions, like those for HSV-1 (published by Huet et al⁷) and phage λ (published by Lander et al⁸) in Figure 3.9 below.

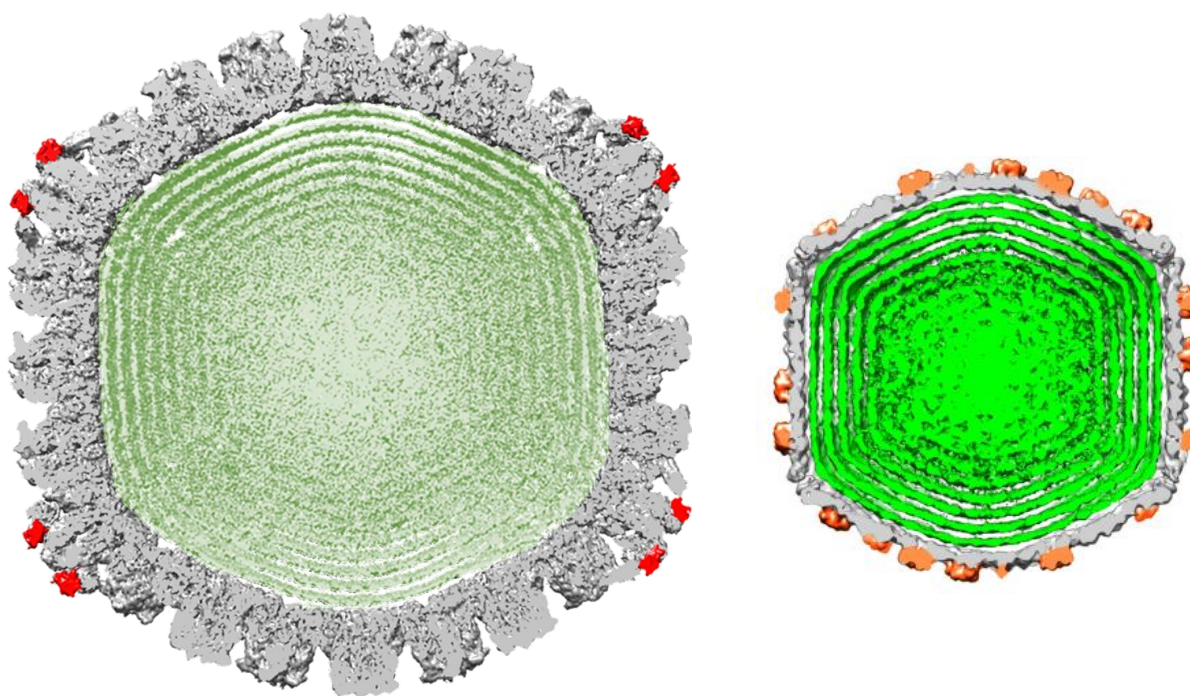


Figure 3.9: High resolution cryo-EM reconstructions are helpful in describing the electron density of viruses. Density maps like these for HSV⁷ (left) and phage λ ⁸ (right) show that viruses can be approximated as concentric, near-spherical shells of electron-dense DNA surrounded by a thicker electron-dense protein shell. Accurately knowing the thickness and position of these layers allows for calculation of the form factor and modelling of the intensity versus q plots measured with SAS.

3.2.2 SAS form factor modelling

As mentioned in the previous section, SAS intensity has a direct dependence on the scattering vector and the scattering length density (sls) distribution, $\rho(r)$, of scattering objects: $I(q) = \int \rho(r)e^{iq \cdot r} d^3r$, or assuming spherical symmetry⁹: $I(q) = 4\pi \int \rho(r) \frac{\sin(qr)}{qr} dr$. Therefore, the radial density distribution of the particles determines the unique shape of I versus q plots obtained with a SAS technique. The raw SAS data is measured on an area detector as a 2D radial intensity map. This projected scattered intensity pattern typically has circular symmetry and the q – dependence can therefore be obtained through circular averaging and radial reduction of the intensity map. The measured q range depends on the geometry of the SAS setup and detector.

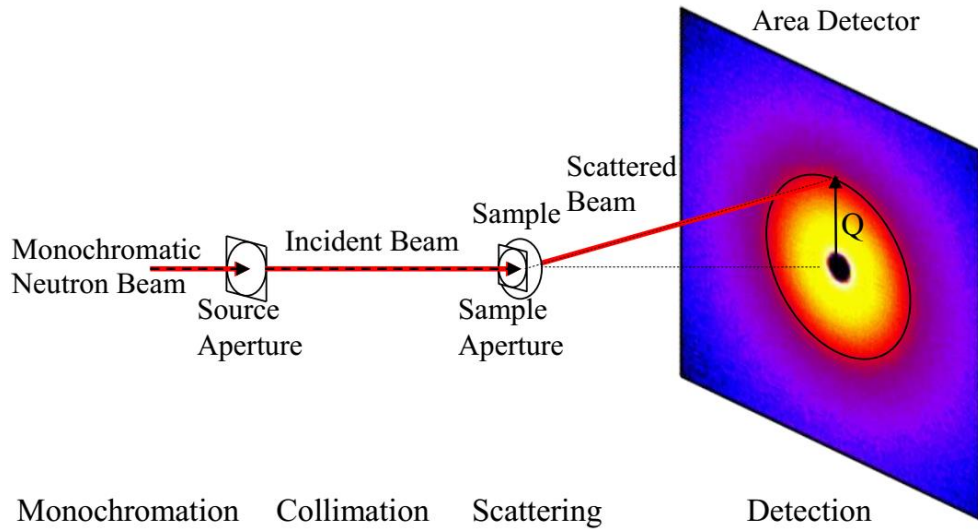


Figure 3.10: This illustration³ from Boualem Hammouda at NIST's National Center for Neutron Research nicely illustrates the intensity map projected onto the 2D detector in a SAS experiment. The intensity typically has circular symmetry and its q – dependence can be measured by monitoring the change in recorded intensity from the center of the map ($q = 0$) to its outer edges (q_{mas} determined by experiment geometry). This figure nicely illustrates why the scattering vector q is also called the momentum transfer vector – it describes the magnitude and direction that the scattered particles were deflected by their interaction with the sample particles.

Because of this predictable q – dependence for well-defined particles, it is possible to use SAS to study transitions of particles from one form to another. For example, in the process of viral DNA ejection, a population of viruses starts out uniformly DNA-filled and ends uniformly empty. Since these two distinct species are structurally well defined, the scattering curves due to them can be modelled. The resulting models can be compared to measured experimental data to verify (or disprove) the existence of a particular structure within the sample at any given time. This enables one to check if, indeed, the sample begins with all DNA-filled particles and ends with all empty particles. In addition, this approach can also be utilized to study the intermediate populations, which may contain both filled and empty particles simultaneously (or, perhaps even partially filled particles). I used such a modelling strategy to extract more information from my DNA ejection dynamics SAXS experiments (Figure 3.11).

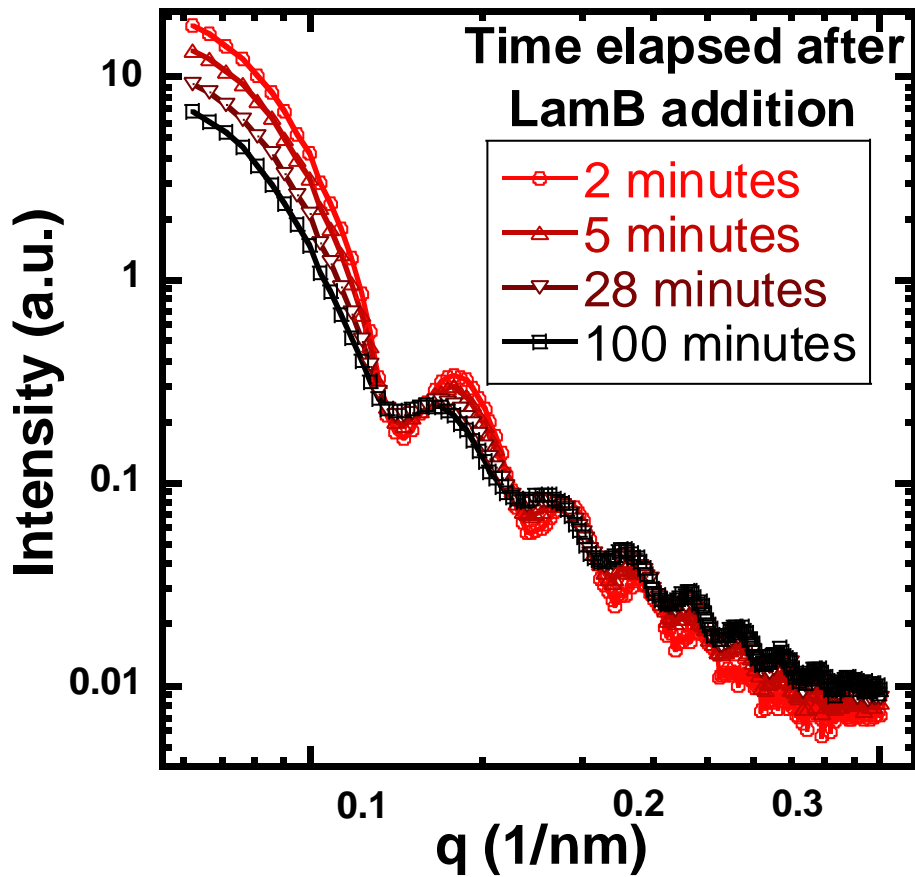


Figure 3.11: Time-resolved SAXS experiments done at MAX IV in Lund, Sweden showed an evolution of the scattering form factor as the phage λ population in the sample transitioned from DNA-filled to empty protein shells.

My first modelling efforts, and those reported in my first paper⁴, were as simple as possible: I considered the virus to be a core-shell particle. Such a particle is made of an electron-dense spherical shell (with radius R_s and uniform scattering length density ρ_s) filled with a core (of radius R_c and uniform ρ_c). To model a particle like this, it is necessary that the shell have a different scattering length density from the solvent background: $\rho_s \neq \rho_{solvent}$. While the shell must be electron-dense, the core can be the same as the solvent ($\rho_c = \rho_{solvent}$) or different (Figure 3.12).

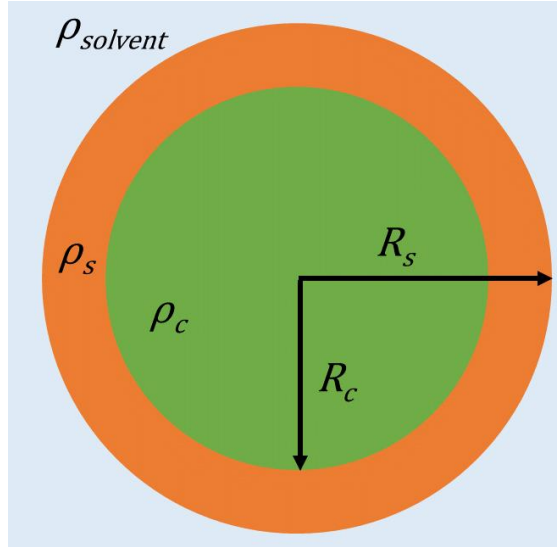


Figure 3.12: An illustration of a core-shell particle. To model the q -dependent intensity for a particle like this, you must be able to mathematically describe each parameter in the figure.

Given the core-shell setup described, the scattering intensity can be modelled by:

$$I_{core-shell}(q) \propto \frac{1}{V_s} \left(\frac{3V_c}{qR_c} (\rho_c - \rho_s) j_1(qR_c) + \frac{3V_c}{qR_s} (\rho_s - \rho_{solvent}) j_1(qR_s) \right)^2$$

Here $j_1(qR)$, the first spherical Bessel function, results from the mathematical description of the spherical electron-dense shells of DNA and protein. The spherical Bessel functions from this core-shell model describe some of the unique peaks and valleys observed experimentally for both DNA-filled and empty viral capsids. Filled and empty capsids can be coarsely modeled as core-shell systems with the capsid as the protein shell and a core of either DNA (filled capsid) or solvent (empty capsid). Partially-filled capsids can be coarsely modelled by modifying the core scattering length density (here this was done by taking weighted averages of the scattering length densities of DNA and solvent). Figure 3.13 illustrates the different core-shell models for DNA-filled, partially DNA-filled, and empty capsids.

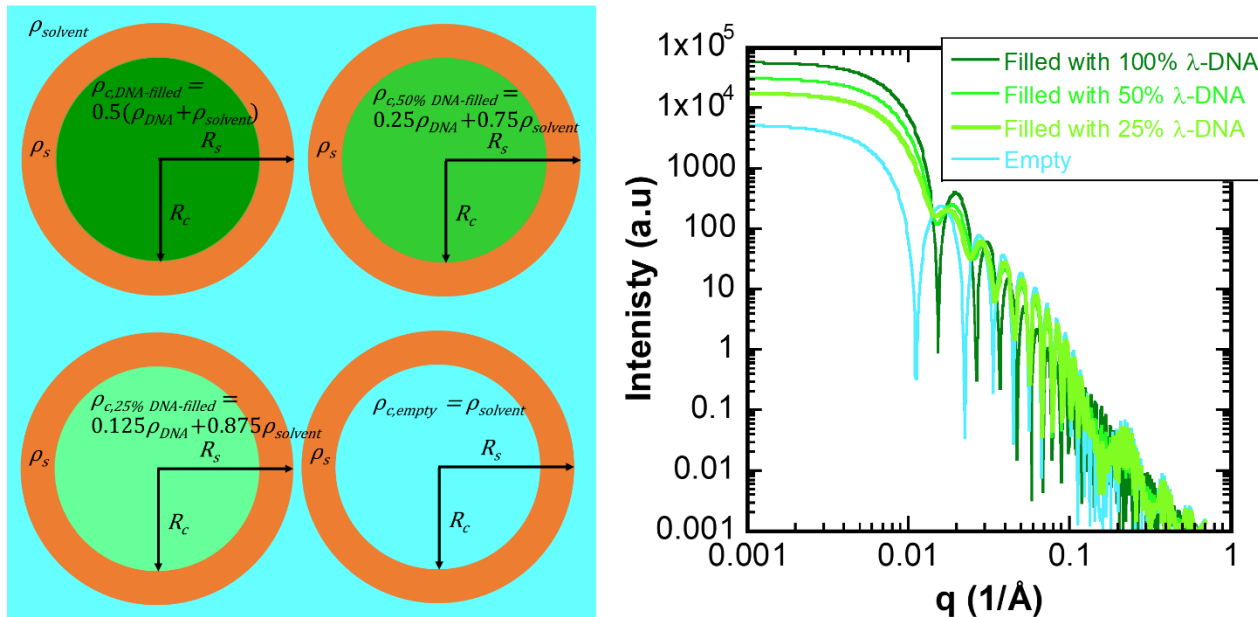


Figure 3.13: By varying the scattering length density, one can model viruses as core-shell particles with cores ranging from 100% λ -DNA (since λ -DNA occupies ~50% of the core volume, the core sld for a DNA-filled particle is the average of DNA and solvent sld values) to solvent. Intermediate states are modelled by estimating the core sld with weighted averages of the DNA and solvent sld values. Given accurate sld values and known particle geometry, the scattering curves can be coarsely modelled.

In Chapter 4, I compare the I versus q dependence for time-resolved SAXS experimental data with two ejection models developed using the core-shell modelling described above. The two ejection models (illustrated in Figure 3.14) are: 1) stochastic ejection modelled with linear combinations of DNA-filled and solvent-filled protein shells (weighting of each curve is described by the ratio “Filled:Empty”); and 2) synchronized ejection modelled by changing the density of DNA filling the core (DNA density described by “% DNA Inside”).

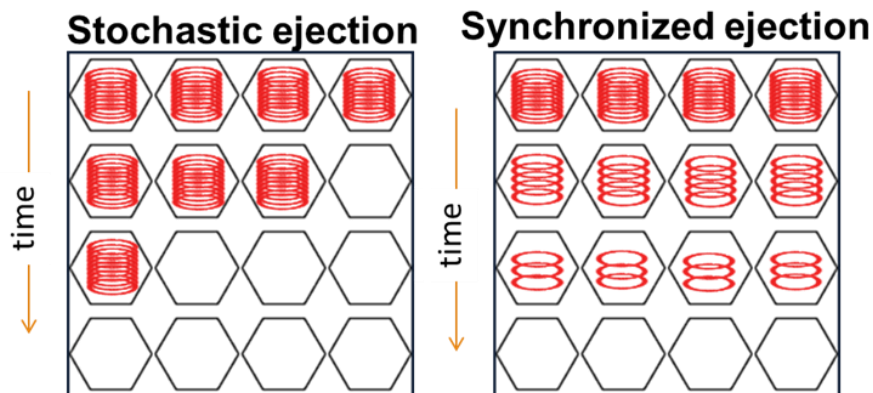


Figure 3.14: Stochastic ejection is modelled by assuming that only filled or empty particles can exist in the sample together. Synchronized ejection, on the other hand, assumes that the particles all eject simultaneously and the population can be considered to be made of homogenous partially-filled capsids.

By comparing these two models to the experimental data, it was possible to rule out synchronized ejection (this is discussed in much greater detail in Chapter 4) as a mechanism to describe DNA ejection dynamics. This is just one simple example of the power of modelling.

SAS models can also be much more sophisticated. To understand the SAS curves more deeply, I explored a more realistic model – I started by considering the virus to be a series of nested core-shell particles. For example, a particle with three layers could be seen as a core shell particle (with R_c , ρ_c , R_{s1} , and ρ_{s1} as described above) nested within an outer shell of R_{s2} and ρ_{s2} . See Figure 3.15.

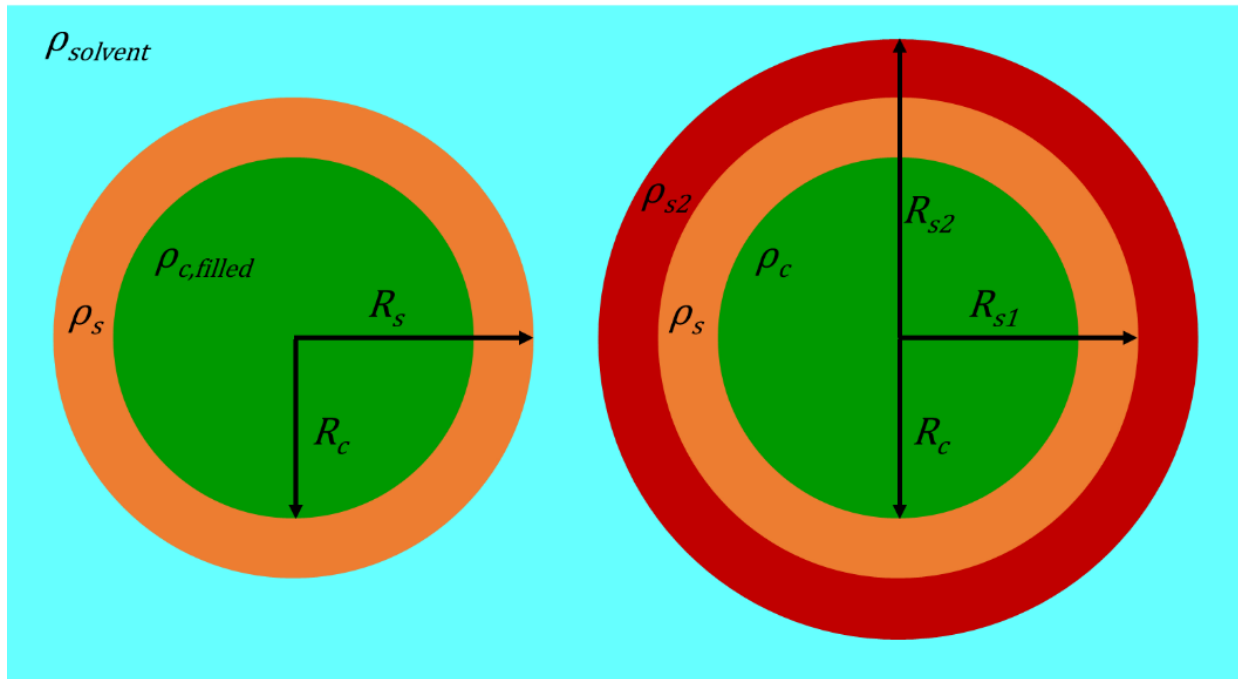


Figure 3.15: A particle with three layers can be modelled as a core-shell particle by accounting mathematically for the structure of the “core”. That is, the “core” is itself a core-shell particle (whose contribution to scattering can be described as above) that is nested into an additional outer shell.

The scattering intensity profile of such a triple-layer particle is described below. The equation is similar to the core-shell intensity described above, but with the addition of a third term describing the new shell of radius R_{s2} and sld ρ_{s2} :

$$I(q) \propto \frac{1}{V_{s2}} \left(\frac{3V_c}{qR_c} (\rho_c - \rho_{s1}) j_1(qR_c) + \frac{3V_c}{qR_{s1}} (\rho_{s1} - \rho_{s2}) j_1(qR_{s1}) + \frac{3V_c}{qR_{s2}} (\rho_{s2} - \rho_{solvent}) j_1(qR_{s2}) \right)^2$$

Building a “mutlshell” model, as it is called, is thus done by adding a $\frac{3V_i}{qR_i} (\rho_i - \rho_{i+1}) j_1(qR_i)$ term for each shell i , starting from the core ($i = 0$) and working out to the solvent ($i = N$). These terms are summed and

the sum is squared and scaled by the volume of the entire particle ($4\pi R_{SN}^3/3$). In this way, a model can be built to accommodate as many shells (all with varying thicknesses and positions) as desired. Such a model is described mathematically with the general expression:

$$P(q)_N = \frac{scale}{V_N} \left[\sum_{i=1}^{N-1} \frac{3V_i(\rho_i - \rho_{i+1})}{qr_i} j_1(qr_i) + \frac{3V_N(\rho_N - \rho_{solvent})}{qr_N} j_1(qr_N) \right]$$

Thus, one could use this expression to build a model to represent a typical dsDNA virus particle. For example, with phage λ it is known from cryo-EM reconstructions like the one in Figure 3.16 (published by Liu et al¹⁰) that in addition to a protein shell of known thickness, there are at least 7 ordered layers of DNA extending from the outer walls of the capsid toward the core. These DNA layers are separated by layers of solvent, and the core seems to be comprised mostly of solvent.

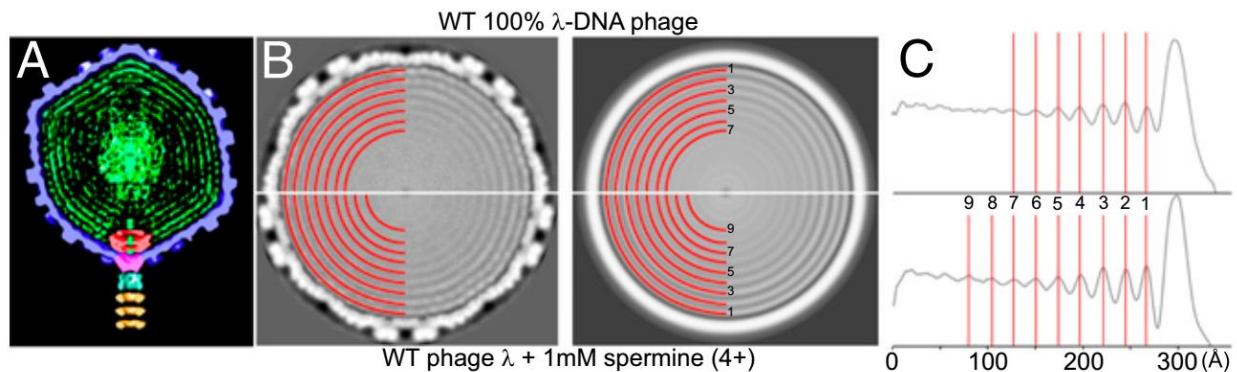


Figure 3.16: Cryo-EM reconstructions provide powerful evidence for DNA ordering as concentric spherical shells with tight packing. These results can be used to determine the location and thickness of electron-dense spherical shells in multi-shell SAS modelling.

Using images like those in Figure 3.15, I had parameters from which to start constructing models for capsids of phage λ and HSV-1. I carefully placed layers of DNA, solvent, and protein to match the cryo-EM structures as closely as possible, then adjusted those layers in an effort to match the modelled curve to the experimental data. Since there are so many free parameters in a model like this, I was not able to use a fitting function but instead adjusted the parameters by hand to see which arrangement of materials would most closely mimic the experimental results. My closest-match for phage λ is shown in Figure 3.17 below. A wonderful feature of this type of modelling is the accurate prediction of the DNA diffraction peak that is observed experimentally.

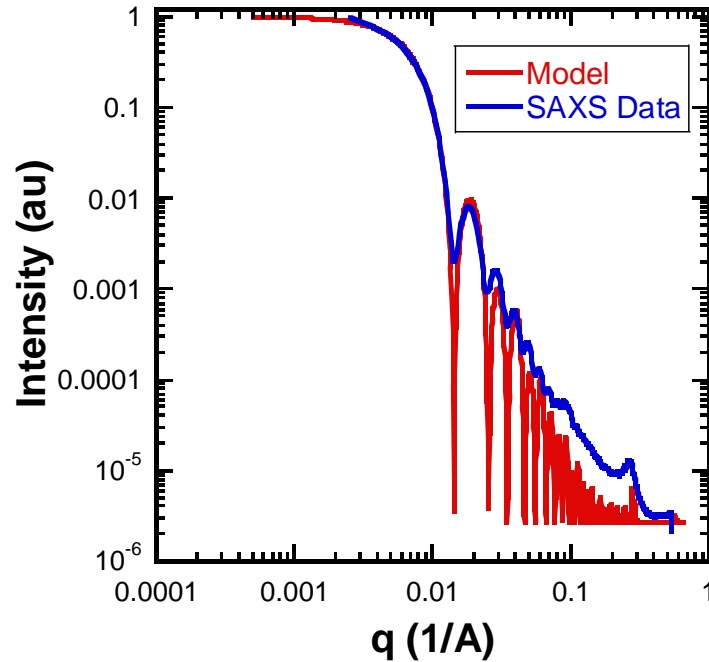


Figure 3.17: This phage λ capsid model was constructed using the equation for the multishell form factor, $P(q)_N$. As a starting point, I used the capsid shell size and DNA layer location provided by cryo-EM micrographs like the one in Fig. 3.15. While those parameters taken at face value did not produce a fully accurate model, the locations of different layers could be adjusted to more closely match the experimental data. Taking instrumental smearing into account would bring even better convergence between the model and experiment.

I built similar models for HSV-1 capsids; Figure 3.18 shows DNA-filled and empty models. Notice the lack of DNA peak in the empty model and the accurate location of it in the DNA-filled model.

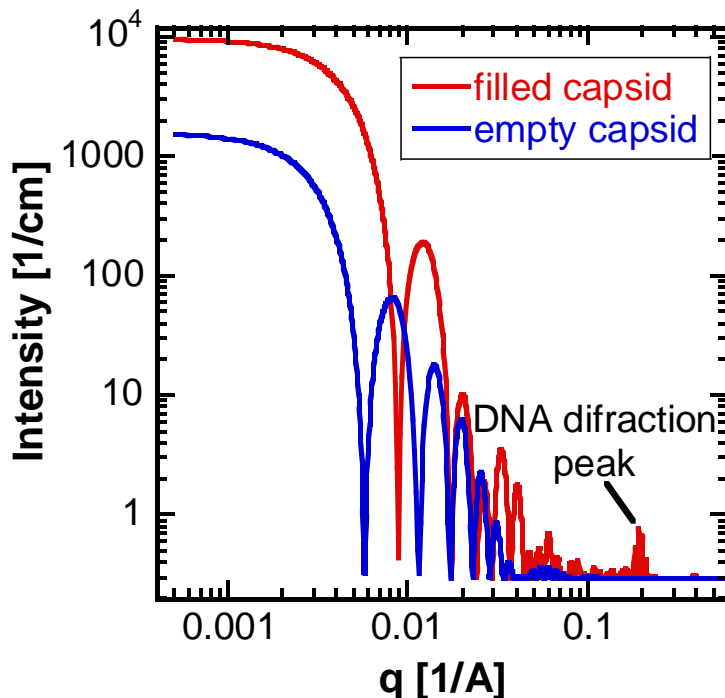


Figure 3.18: The multi-shell model applied to HSV-1 capsid geometry. There are several significant differences between DNA-filled and empty capsids – the scattering curves are well defined for both species of scatterers, which correlates well with the fact that both can be independently measured in experiments.

Finally, to round out this modelling effort, I explored the consequences of moving different DNA layers radially throughout the capsid to see if SAS would be capable of resolving small changes in radial DNA density. Some of these results are highlighted in Figure 3.19 for HSV-1.

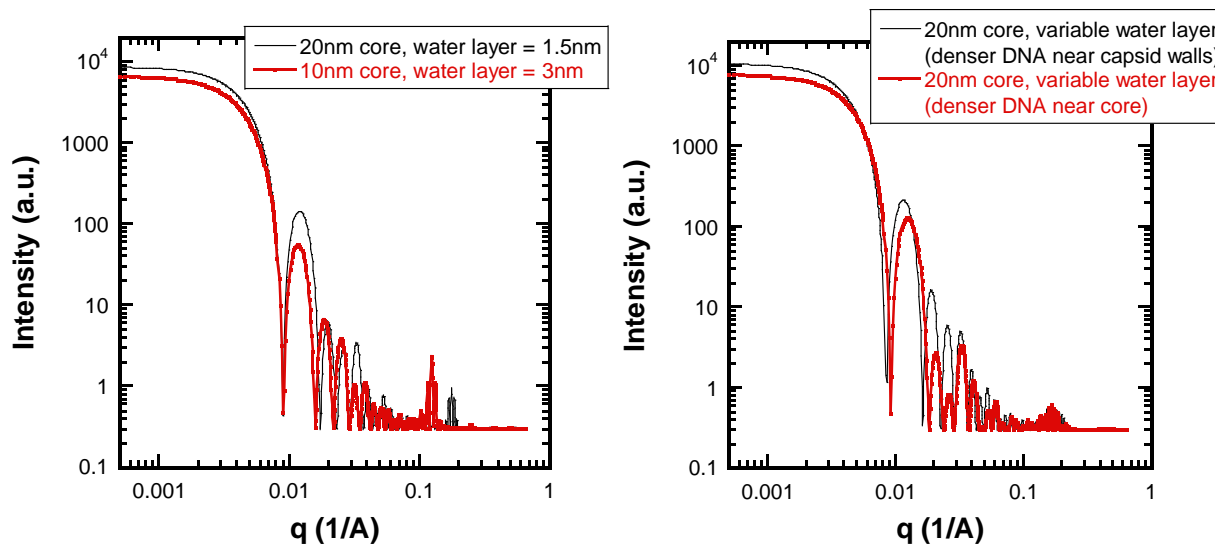


Figure 3.19: By exploring the effect on models of changing the location of DNA layers, I observed that the q -dependence of scattered intensity depends strongly on the exact arrangement of DNA within the viral capsids. Moving the DNA layers around shifted the relative positions of scattering minima and maxima and also influenced strongly the DNA diffraction peak (from which DNA-DNA interaxial spacing is measured). Given that, SAS experiments should be able to yield precise information about the DNA radial density distribution within capsids. What is needed is a way to reliably fit experimental data – as of now, that is difficult due to the many parameters in the model.

Models like these would be essential for extracting meaningful structural information from SAS experiments.

One possible way to extract this information is to mask certain parts of the scattering with contrast matching.

Typically, contrast matching is done with small angle neutron scattering (SANS), where the solvent scattering length density can be chosen to match the scattering length density of some component of the scattering particle. For example, one could match the sld of the solvent to the sld of the viral capsid. The resulting scattering would be due only to the DNA packaged within the capsid; the protein shell itself would be essentially “invisible” to the neutron beam. In an effort to test this idea, I did perform several SANS experiments at Paul Scherrer Institute (Villigen, Switzerland) and Institut Laue-Langevin (Grenoble, France). The concept for the experiments is shown below in Figure 3.20. The figure shows the preliminary SANS results which, while insufficient for analysis with precise models due to the very weak scattering signal, does prove the concept that contrast matching can be used to isolate scattering from encapsidated

DNA only, and that the resulting scattering curve would have a significantly different angular dependence than the scattering from a whole capsid (including the protein shell).

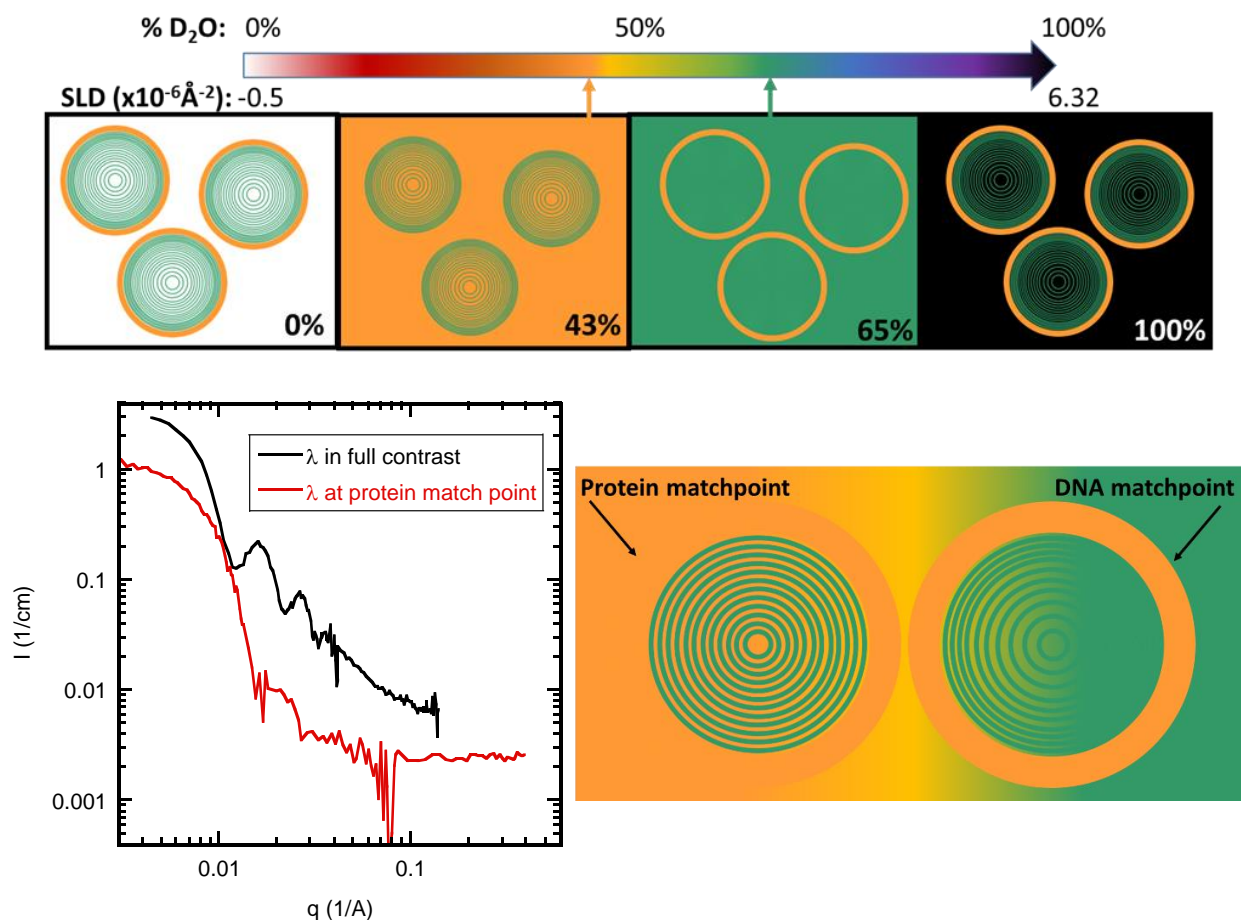


Figure 3.20: Some SAS techniques, such as SANS, allow for contrast matching of the solvent background with different components of the scattering particles. This can be taken advantage of to “mask” the scattering of a specific component – such as the protein-based capsid or the encapsidated DNA. By isolating the scattering from the remaining component, it is easier to understand from which physical markers each feature of the scattering curve derives. For viruses like phage λ and HSV-1, the protein shell can be contrast matched by preparing the viruses in a solvent made of 43 wt% D₂O and 57 wt% H₂O. Such an experiment was performed with the result plotted in the bottom right of this figure – while the resolution is not good, it is clear that there is a difference in scattering when the protein shell is or is not contrast-matched with the background.

3.2.3 SAXS experimental details

For the published⁴ DNA ejection dynamics experiments presented in this thesis, small angle X-ray scattering (SAXS) measurements were carried out at the I911-4 beamline at the MAX IV Laboratory in Lund, Sweden (wavelength $\lambda = 0.91\text{Å}$, scattering vector range of $0.006\text{-}0.475\text{Å}^{-1}$). The sample was $20\mu\text{L}$ of $\sim 2 \times 10^{13}$ pfu/mL bacteriophage λ solution which, just before loading, was mixed with $30\mu\text{L}$ of 0.36mg/mL LamB solution to trigger DNA ejection. The sample was then immediately injected into a flow through

capillary held at 20°C. The intensity was monitored for 100 minutes, with higher resolution during the first 1.5-6.5 minutes (10 consecutive 30s exposures) followed by alternating 2 minute exposures and 3 minute breaks. The intensity versus scattering angle was plotted for each time and the curves analyzed with linear combination fitting, as described in the text, to yield the fraction of filled phages as a function of time.

3.3 Cryo-transmission electron microscopy

Cryo-transmission electron microscopy (cryo-TEM) was used as a third experimental method in the phage λ DNA ejection dynamics study described in Chapter 4. It was a unique and necessary addition to this study because, unlike the scattering methods which indirectly probe whether capsids are DNA-filled or empty, cryo-TEM takes a literal snapshot of the population at different points in time. Taking these time-resolved pictures of the system allowed me to verify that a significant fraction of phages retain their DNA for tens of minutes after adding the ejection-triggering receptor, LamB.

3.3.1 Introduction to cryo-transmission electron microscopy

Electron microscopy works, in general, by firing an electron beam at a sample and monitoring where each electron ends up after the interaction with the sample. In cryo-TEM, the sample is frozen in a sheet of vitreous ice – this is done both to protect the sample from the heat of the electrons and, more importantly, to eliminate motion of the particles in the sample so that high-resolution images can be obtained. An electron beam is directed onto this frozen sample, where it interacts with the particles. The electron is absorbed by dense materials – like compact protein and encapsidated DNA – but passes through the ice without significant loss or deflection. In this way, monitoring the location and number of electrons that are transmitted through the ice and sample can yield an image of the particles in the sample (see Figure 3.21 for an interesting example).

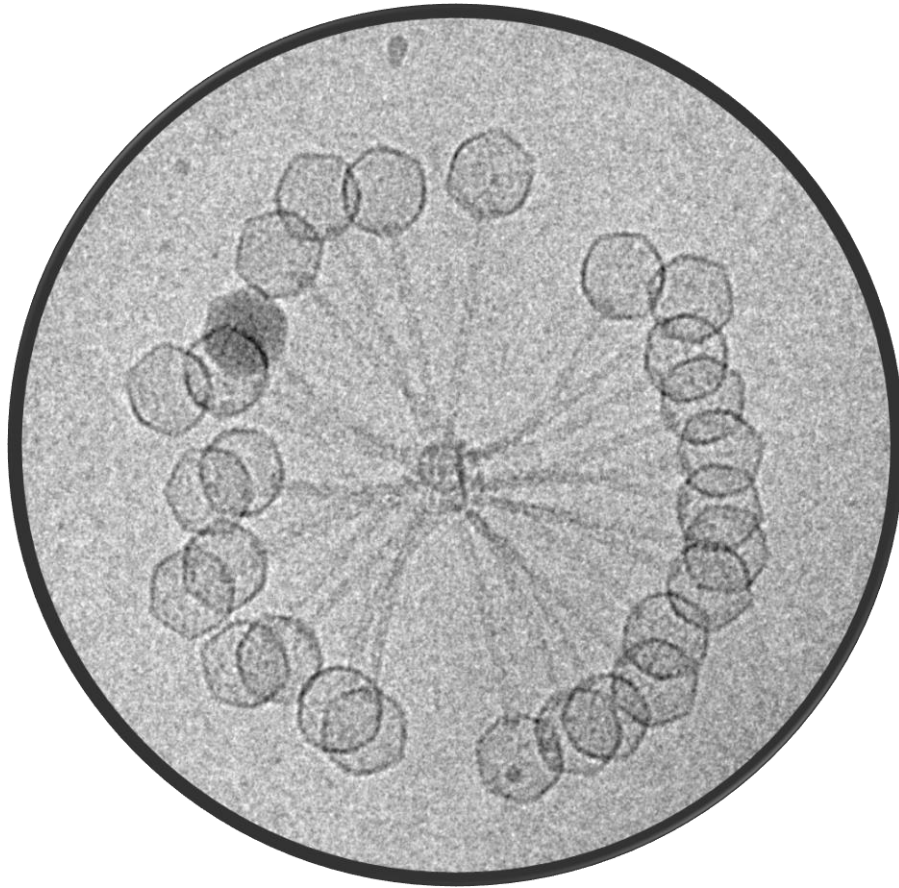


Figure 3.21: A cryo-TEM micrograph of phage λ particles. All particles but one (in the top left quadrant of the group of phages) have ejected their DNA. These phages are grouped together due to the preparation method in this particular experiment: ejection was triggered and allowed to complete, then ejected DNA was digested and the sample was rinsed/filtered to exchange the buffer. In this buffer exchange, the surfactant responsible for solubilizing the receptor protein LamB was washed away. This caused the hydrophobic receptor protein to attract many phage tails in an effort to reduce its contact with water. The result is a beautiful bouquet of viruses.

3.3.2 Cryo-TEM experimental details

Cryo transmission electron microscopy (cryo-EM) samples were prepared by mixing, in a water bath held at 20°C, 20 μ L of $\sim 2 \times 10^{13}$ pfu/mL bacteriophage λ solution with 30 μ L of 0.36mg/mL LamB solution. The samples were incubated at 20°C for a specified time (between 1 and 100 minutes) then vitrified in a controlled environment vitrification system by loading onto a glow discharged lacey carbon film supported by a copper grid, blotting with filter paper to create a thin film, then plunging the grid into liquid ethane at its freezing point. The vitrified samples were stored under liquid nitrogen and imaged with an electron microscope (Philips CM 120 BioTWIN Cryo) equipped with an energy filter imaging system (Gatan GIF 100) and a digital multiscan CCD camera (Gatan 791). One grid was prepared for each timepoint

studied, and for each grid at least 20-30 micrographs of unique 750nm X 750nm square areas (containing at least 500 unique phages total) were imaged. These micrographs were analyzed and averaged to measure the fraction of DNA-filled capsids remaining in the sample at a given time. The average fractions of filled particles versus total number of particles were normalized between 0 and 1 to account for phages that either were empty before the experiment began or damaged DNA-filled phages which do not trigger DNA ejection. This normalization was accounted for in propagation of the standard errors [standard error $\sigma_{SE} = \sigma_{SD}/\sqrt{\text{\#micrographs}}$, where σ_{SD} is the standard deviation of the fraction of DNA-filled phages across all of the micrographs at a particular timepoint], which are plotted with the average fraction of DNA-filled phages at each timepoint.

3.4 Atomic force microscopy

Atomic force microscopy (AFM) was used for the experiments described in Chapter 5, the DNA retention section of this thesis. The technique was used to measure mechanical properties (specifically, stiffness, breaking force and maximum indentation before breakage) of HSV-1 viral capsids with varying amount of reinforcement protein UL25 present. These results of these experiments pointed toward a model of mechanical reinforcement by the UL25 protein.

3.4.1 Introduction to atomic force microscopy

Atomic Force Microscopy (AFM) is a quantitative imaging and mechanical mapping technique for samples with nanometer scale features (such as viruses!). The method is based on the precise knowledge of the position of a tool called the “tip”. The tip is essentially a nanometer scale (in the experiments described here, the tip has a radius of ~20nm) stylus that interacts with a sample which has been deposited onto a rigid substrate (here, glass is used as the substrate). The tip is mounted on the end of what is called the “cantilever” – a long (~100 μ m), flexible rod with known nominal spring constant and resonant frequency. The cantilever juts off the end of a chip known as the “probe”, which is loaded into a probe holder and inserted into the experimental apparatus. In the AFM used in this study, the probe holder is situated above the sample such that the probe, cantilever, and tip are all submerged in the sample fluid. The sample, a small droplet deposited onto glass, is fixed to a rigid metal puck. This puck is in turn fixed to the sample platform, the position of which is precisely controlled by a piezoelectric scanning motor. In an AFM experiment, the piezo drives the sample stage to move. When the tip is in contact with the sample surface,

motion leads to changes in topography and bending of the cantilever. The cantilever is covered in gold to enhance its reflectivity, because its position (and thus the position of the tip mounted below) is tracked by monitoring its reflection of an incoming laser beam. This concept is illustrated in Figure 3.22 where the tip is shown to be interacting with an HSV-1 capsid (the object of max height ~125nm).

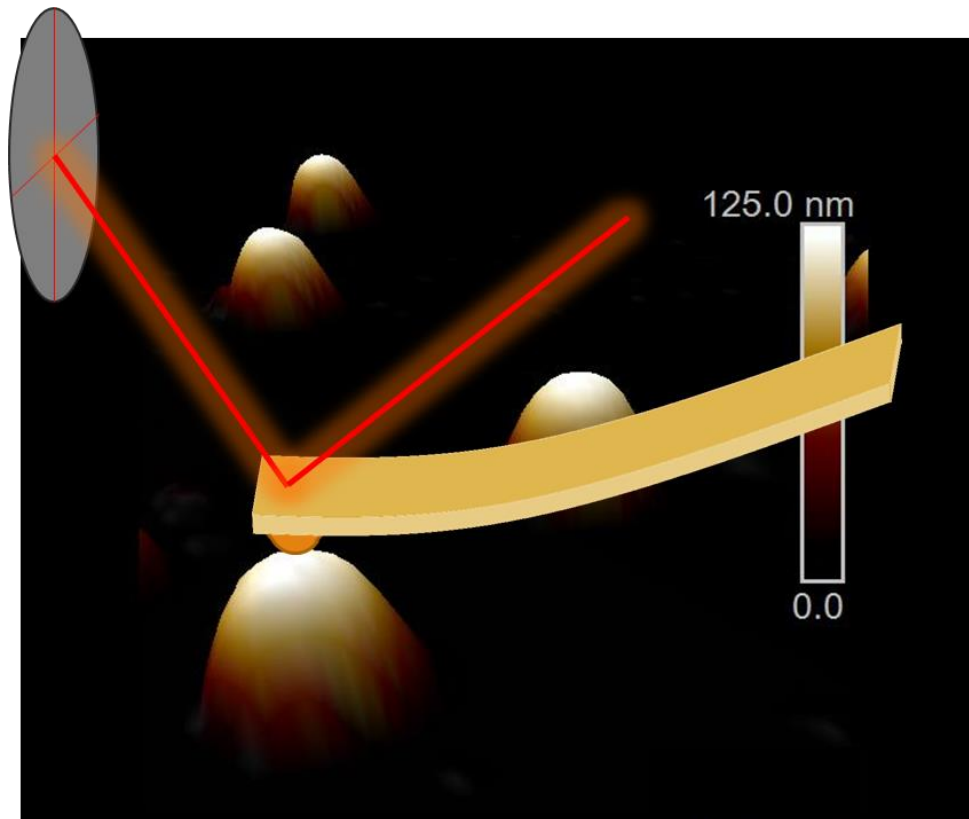


Figure 3.22: AFM relies on the very precise knowledge of tip position in all three spatial dimensions. As the sample moves relative to the probe, the tip height increases or decreases to accommodate the changing topography of the surface beneath it. This changing height is monitored by tracking the deflection of a laser beam reflecting off the top of the probe's cantilever. The more the cantilever bends to allow the tip to keep up with topographical changes, the greater is the deflection of the laser beam.

When the sample stage is driven to move by the piezoelectric scanner, the consequent motion of the cantilever (due to changes in the sample topography that tip is interacting with) is recorded as deflections of the laser beam from the center of the detector. The magnitude of these deflections is fed back into the AFM system in a feedback loop that aims to maintain a constant interaction between the tip and the sample (for example, the feedback loop could be used to maintain the same distance between the tip and the sample at all times, despite changing sample topography).

3.4.2 AFM calibration techniques

In addition to being used to measure precise topographical details of the sample deposited on the glass, AFM can also provide (with the right controls) absolute measurements of capsid mechanical properties. The most commonly measured properties in this thesis were the capsid spring constant (k), the capsid breaking force (F_{break}) and the maximum capsid indentation before breakage (d_{max}). These quantities can be precisely measured under a range of conditions to study the sample parameters important to mechanical strength. However, care must be taken in such measurements to account accurately for all the mechanical objects present in the system. Most importantly, it is essential to calibrate the response of the AFM by measuring the exact cantilever stiffness and quantifying the input versus output response of the system. The cantilever stiffness, $k_{cantilever}$ (units of N/m), is measured with a technique called “thermal tune”, where the cantilever is oscillated in free space (in the sample volume but away from the substrate or sample particles) at a range of driving frequencies. The response of the cantilever to this driving is recorded and the peak is analyzed to extract the exact cantilever resonant frequency and spring constant. The input versus output response of the system is calibrated by measuring a variable called the deflection sensitivity. Deflection sensitivity describes the spatial distance the piezo moves when 1 volt is applied to it. It is measured by pushing a clean section of the glass substrate against the tip and measuring the slope of the resulting volts per nanometer plot; the inverse of the slope is the deflection sensitivity (units of nm/V). With $k_{cantilever}$ and deflection sensitivity in hand, one can “ramp” – or push with a known force – on the substrate or a particle in the sample. This can be done by telling the instrument to send a defined voltage to the piezo, which results in the scanner (and thus sample) pushing, with a defined force, against the tip. The absolute magnitude of this force of this push is determined by multiplying the defined pushing voltage (V) by the deflection sensitivity (nm/V) and the cantilever spring constant (N/m) to yield a force value in nN.

3.4.3 AFM measurement and data analysis

With the calibrations of the cantilever and instrument done, AFM measurements can proceed. Figure 3.23 below describes the methodology of making an AFM measurement of particle stiffness, breaking force, and maximum indentation. A measurement is done by maneuvering the tip to the center of a capsid and ramping, first with a small force and then with a large force. The small-force ramps produce a linear response in the resulting applied force versus Z curve (this is called the FZ-curve, or force curve).

The large-force ramps cause the response of the capsid to become non-linear, and eventually lead to capsid breakage.

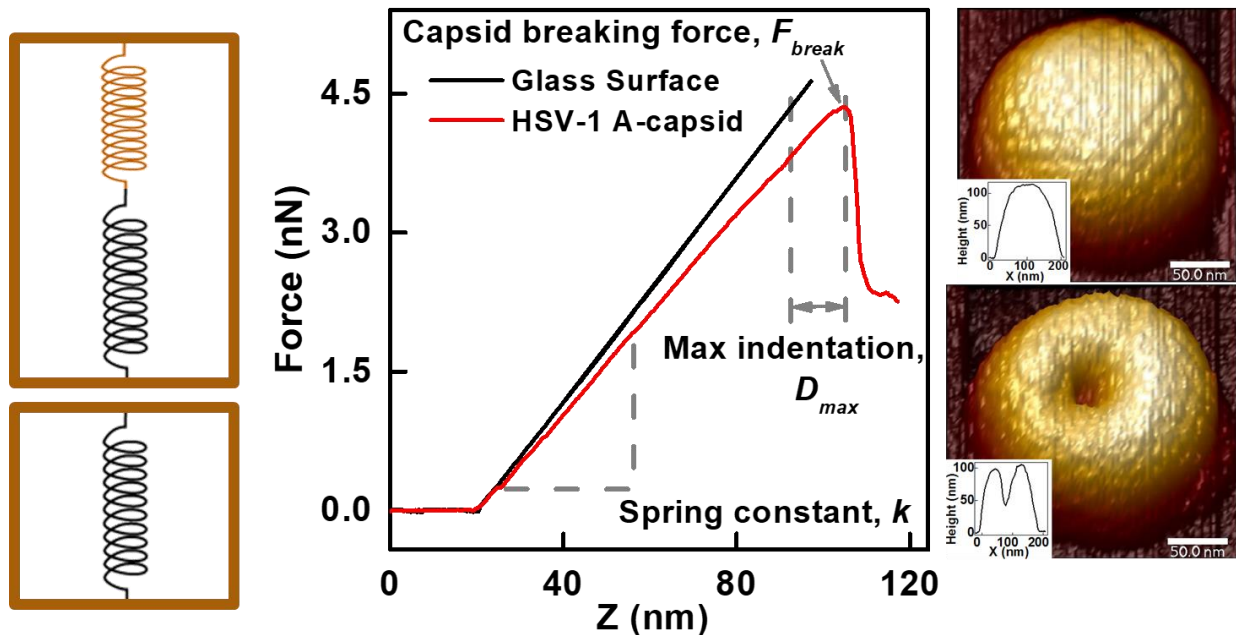


Figure 3.23: Pushing the tip and sample together with a known amount of force allows for the measurement of force curves, like the one shown in the middle of this figure. The slope of a force curve yields spring constant and, for capsids, the sharp drop-off point of the force curve corresponds to capsid breakage. To obtain accurate capsid spring constants, a force curve measurement of nearby glass must also be made.

The linear response of the capsid to low applied forces is due to the behavior of the capsids as elastic shells. This elastic behavior is only a global property of the capsids; on smaller length-scales, the response of the capsid to applied forces will certainly depend strongly on where exactly the capsid is pushed and may be highly non-linear. We ensure that we are measuring global, elastic mechanical properties by choosing the tip wisely. We chose a relatively (compared to most high-resolution tips with tip radii of just a few nm) blunt tip with tip radius ~ 20 nm for these experiments. Given that the HSV-1 capsids measured here have a radius of ~ 60 nm, our mechanical probing covers a fairly large area of the capsid surface. By choosing this coarse tip size relative to the capsid size, we ensure that we probe global rather than local dynamics.

For each capsid probed, a piece of nearby glass must also be measured. This is necessary because the glass also has an elastic response to force. To measure absolute capsid stiffness, the elastic response of the glass (which is felt through the capsid when pushing on the capsid) must be accounted for.

This is done by considering the system to be two springs in series: the tip interacts directly with the capsid and indirectly (through the capsid) with the glass. Therefore, the effective spring constant that is measured

is related to the capsid and glass spring constants by $\frac{1}{k_{eff}} = \frac{1}{k_{glass}} + \frac{1}{k_{capsid}}$ and thus the capsid spring

constant can be accurately determined by $k_{capsid} = \frac{k_{eff}k_{glass}}{k_{glass}-k_{eff}}$.

The breaking force of the capsids requires less mathematical analysis – with the deflection sensitivity and cantilever spring constant in hand, ramping on the capsid produces a force curve with known absolute force. The breaking force is simply read off this graph – it is the point where the force, rather than continuing to increase linearly, suddenly drops off. In Figure 3.24 below, I include a gallery of broken capsids; these were imaged after doing the high-force ramping experiments described above.

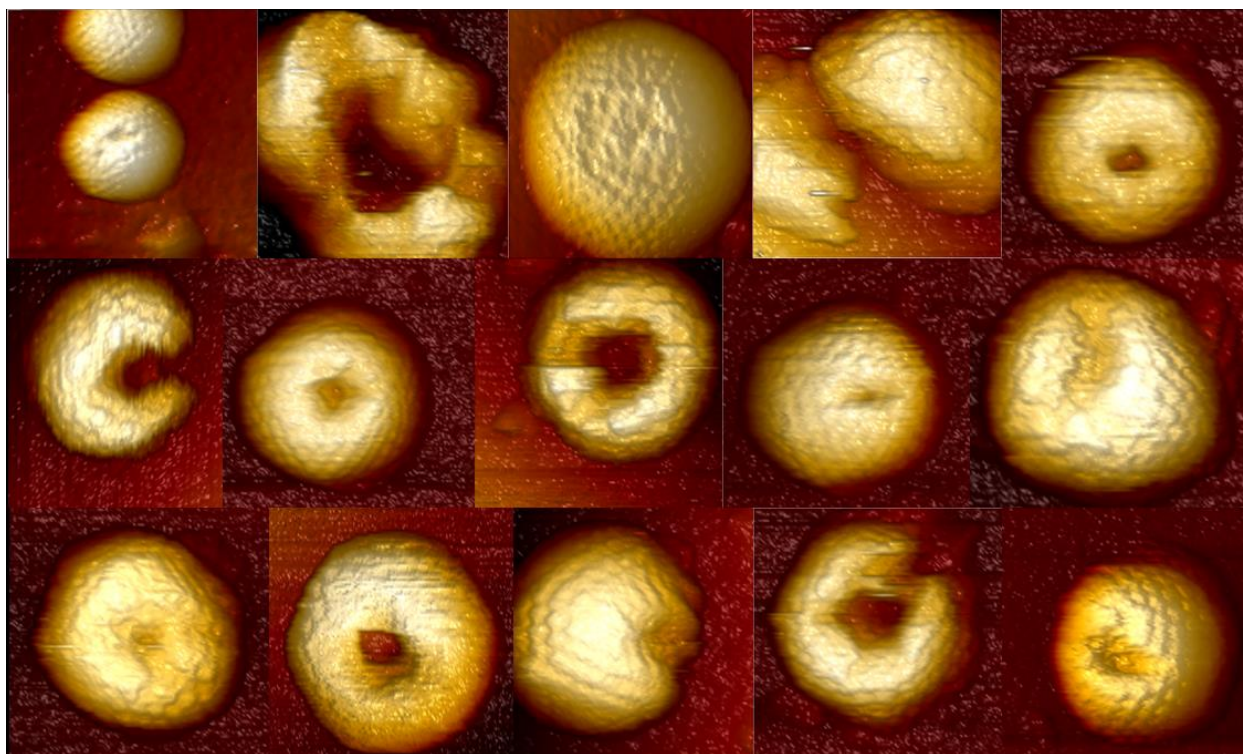


Figure 3.24: A gallery of capsids pushed to their breaking point...literally! The typical force required to break a capsid is a few nanoNewtons, but this varies depending on the type of capsid and the environmental conditions. For example, capsids filled with DNA have a slightly larger breaking force than empty capsids – this indicates that the AFM “feels” a mechanical contribution from the encapsidated DNA.

3.4.4 AFM experimental details

All AFM measurements were performed on a MultiMode8 AFM with NanoScope V controller, NanoScope software and NanoScope Analysis software (Bruker AXS Corporation, Santa Barbara, CA,

USA). Images were acquired in Peak Force Tapping mode. All data (images and force-distance curves) were collected in liquid. A droplet of 40 μl sample was deposited on a glass cover slip. The details of substrate and sample preparations can be found elsewhere ¹¹⁻¹². After 30 min the sample was ready for the experiments. Rectangular gold-coated cantilevers (Olympus, Tokyo, Japan) were used. The cantilever tip radius was 20 ± 5 nm. Measured averaged stiffness of cantilevers was 0.06 N/m, determined by the thermal fluctuations method ¹³. Spring constant and breaking force for a viral particle were obtained from the indentation measurement. At least 15–20 particles were measured to obtain each k and F_{break} value. The details of spring constant calculation are described elsewhere ¹². The breaking force was the maximum force a virus particle could withstand before mechanical failure, as indicated by a significant drop in the force–distance curve. The breaking force was measured directly after AFM cantilever calibration using glass surface indentation.

3.5 Quantitative Western Blot

To quantify the UL25 copy number we ran a Western Blot, which is a qualitative and semi-quantitative technique for protein analysis. To perform a Western Blot on virus samples, the viruses are first boiled in the presence of a reducing agent (stabilized dithiothreitol, which binds to the proteins to prevent disulfide binding), and a surfactant (sodium dodecyl sulfate, a negatively charged molecule which coats the proteins). This unfolds all the proteins, blocks intramolecular and intermolecular binding, and gives the proteins a net negative charge proportional to their molecular weight. The individual proteins making up the virus are then separated spatially using gel electrophoresis; the samples are loaded into wells on the top of a polyacrylamide gel and subjected to an applied electric field (E points to the top of the gel). The electric field creates an electric force on the negatively-charged proteins, which respond by separating from large (near the top of the gel) to small (near the bottom of the gel) proteins as the sample migrates through the gel. After running the gel, the proteins are “blotted” onto a nitrocellulose membrane by lying the gel underneath the membrane and applying a transverse electric field (that is, E points from the bottom of the gel to the top). This electric field pulls the negatively charged proteins out of the gel and onto the membrane above. This membrane is then treated in the following way to probe for specific proteins in the sample:

- 1) **Blocking:** the membrane is soaked in “blocking buffer” (Rockland NIR Blocking Buffer – a solution of a proprietary protein formulation diluted in Tris buffered saline), which blocks unoccupied binding sites on the membrane so they can’t soak up antibodies. The proteins used in blocking buffer are specially designed NOT to bind to antibodies and not to be excited by infrared light. This is done to decrease the background intensity and increase the sensitivity of the experiment.
- 2) **Binding of primary antibody:** the membrane is soaked in a solution of primary antibody, allowing the antibody to bind specifically to a protein of interest. Antibodies are obtained by exposing a host to the protein of interest to induce an immune response, then collecting the resulting material from the host. For example, the antibody which binds to the UL25 protein was collected from a mouse which was injected with a large amount of purified UL25 protein. The mouse had an immune response to the injection and produced antibodies that bind to, in an effort to fight off, the foreign UL25 proteins. The mouse is then bled and the antibodies are harvested as a concentrated protein solution. Such a protein is called Mouse α UL25. The Mouse α UL25 in this study, called A11E4, was provided compliments of Dr. Jay Brown.
- 3) **Binding of the secondary antibody:** the membrane is soaked in a secondary antibody, which binds specifically to the primary antibody and has an infrared tag. The secondary antibody used in this work to bind to the UL25 primary antibody (Mouse α UL25, described above), was called Goat α Mouse IRDye 800 CW.
- 4) **Infrared scanning:** The secondary antibody, when exposed to an infrared wavelength of 800nm, emits a strong fluorescent signal. This is taken advantage of with infrared scanning, which creates an image of your gel with the only visible bands being the ladder (with an excitation wavelength of 700nm) and those bands corresponding to the specific protein being probed (following the same example from steps 2 and 3, this would be the UL25 protein). The intensity of this emitted signal can be measured to quantify the amount of the specific protein being probed.
- 5) **Strip & repeat:** after scanning, all the non-blotted proteins (present from the blocking buffer, primary antibody, and secondary antibody soaks) are removed using a “stripping buffer” (Restore PLUS Western Blot Stripping Buffer). Steps 1-4 are repeated with different primary and secondary antibodies to probe for other specific proteins in the samples. In our case, the second protein probed for was UL38 (using the primary antibody Rabbit α UL38 NC2, compliments of Dr. Fred Homa, and the secondary antibody Goat α Rabbit IRDye 800 CW).

After all the blotting, soaking, and scanning are done the Western Blot is ready for analysis. We actually performed two Western Blots for this system. The first was performed in 2015 and the second, with an

extended concentration range, was performed in 2017. The results of both are summarized below in Figure 3.25.

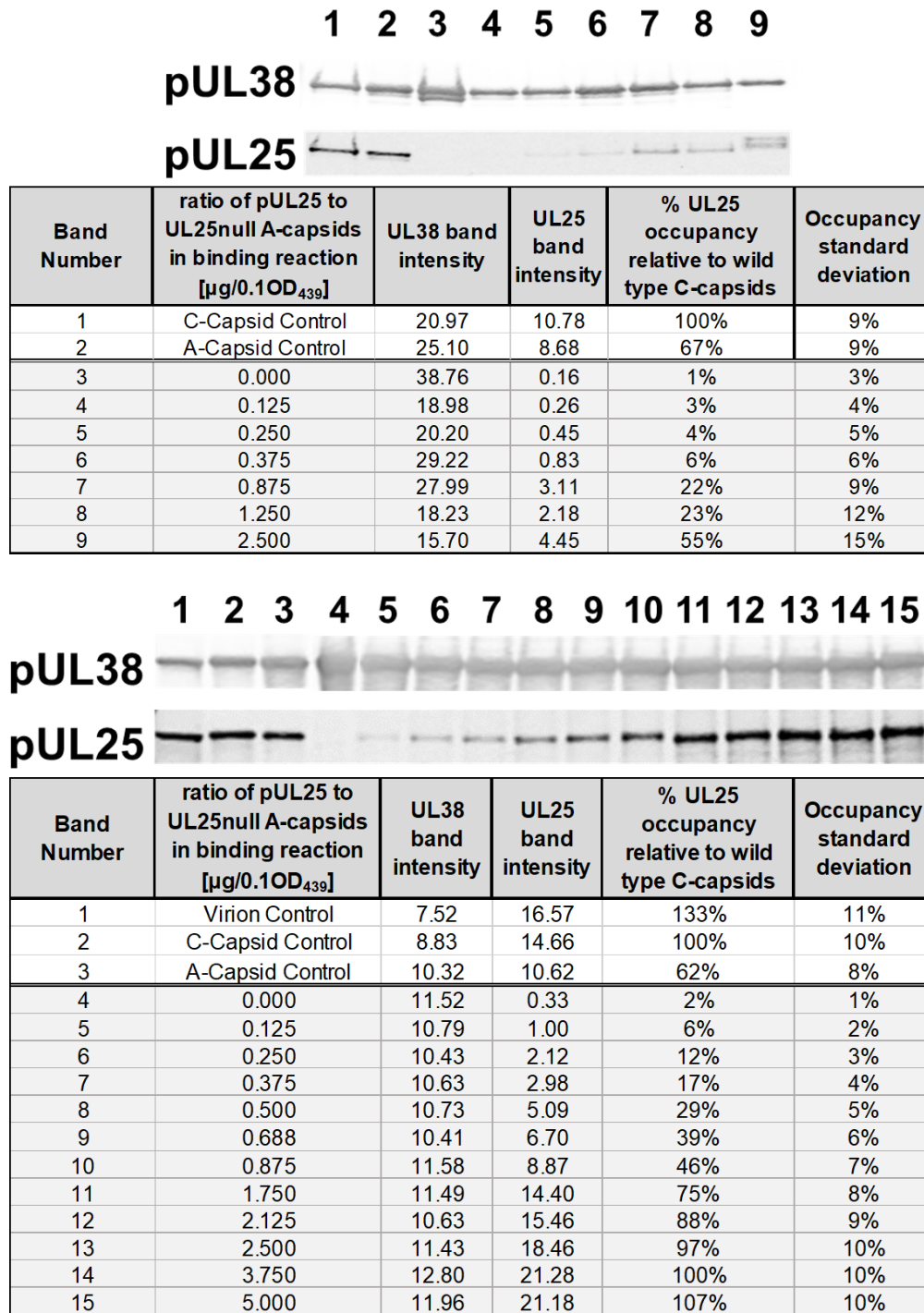


Figure 3.25: The images and quantified results of the two Western Blot's performed in 2015 (top) and 2017 (bottom). The 2017 blot extended to a much larger concentration range to observe the expected saturation of the binding reactions.

By measuring the intensity of each protein band, the protein concentration can be quantified. Knowing that each capsid has the same number of copies of UL38, we can reason that any differences in the UL38 band intensities arises from differences in the number of capsids present in that sample. Small differences in sample concentration can change the measured intensity significantly, so to make accurate copy number comparison a load normalization must be done. We take care of this by calculating ratios of the UL38 band intensities for samples relative to a control (here, we chose wild type C-capsids as the control). Call the ratio $a = \text{UL38}_{\text{sample}}/\text{UL38}_{\text{wt A-capsid}}$. Next, we consider differences in the UL25 band intensities. Any differences in these bands are due to different amounts of UL25 present in the samples; this is affected by both the number of capsids in each sample as well as, for the binding reaction samples, the relative number of UL25 proteins bound per capsid. If the loads were identical (that is, if the ratio a was equal to 1 for all samples) we could compare the UL25 bands in a straightforward way by simply calculating the ratio $b = \text{UL25}_{\text{sample}}/\text{UL25}_{\text{wt A-capsid}}$. However, in real-world experiments the loads are never identical. This is where the previously calculated ratio a comes in. By taking a third and final ratio, b/a , we normalize any differences in the UL25 band intensity by differences in load.

An example can be instructive here: in the 2017 blot above, I can see by comparing UL38 bands that lane 9 is significantly darker than lane 2. To be precise, lane 9 has an intensity $10.41/8.83 = 1.18\text{X}$ higher than the intensity of lane 2. This indicates that there are 118 capsids in lane 9 for every 100 capsids in lane 2. Conversely, in the UL25 bands it looks like the intensity for lane 9 is actually significantly lighter than that in lane 2. Again, to be precise, the lane 9 intensity is $6.7/14.66 = 0.46\text{X}$ the intensity in lane 2. That means there are only 46 copies of UL25 in lane 9 for every 100 copies in lane 2.

I can use the two ratios calculated above to normalize the loads and estimate the relative copy number per capsid. I do that by saying, for example, that lane 2 has 100 capsids and thus lane 9 has 118 capsids (based on the UL38 bands). Then I would make an assumption that says since lane 2 has 100 C-capsids and cryo-EM reconstructions show that there are 60 copies of UL25 per C-capsid, that lane 2 has 6000 copies of UL25 (the exact number of copies per capsid is not important in this calculation – it does not affect the final result at all. I say 60 copies only to illustrate the math at work here). Given that and the fact that lane 9 has only 46 copies of UL25 for every 100 copies in lane 2 (from the UL25 band intensity

ratio calculated above), I could surmise that there are $0.46 \times 6000 = 2760$ UL25 copies in lane 9. Since we also know that there are 118 capsids in lane 9, we can conclude that the copy number is $2760/118 = 23$ (assuming that the C-capsid copy number is 60). In our results, we did not assume a copy number for a particular type of capsid (since this is currently under debate), but instead calculated a % UL25 occupancy relative to a control (here, I chose the wild type C-capsids as the control). The results are shown in Figure 3.26.

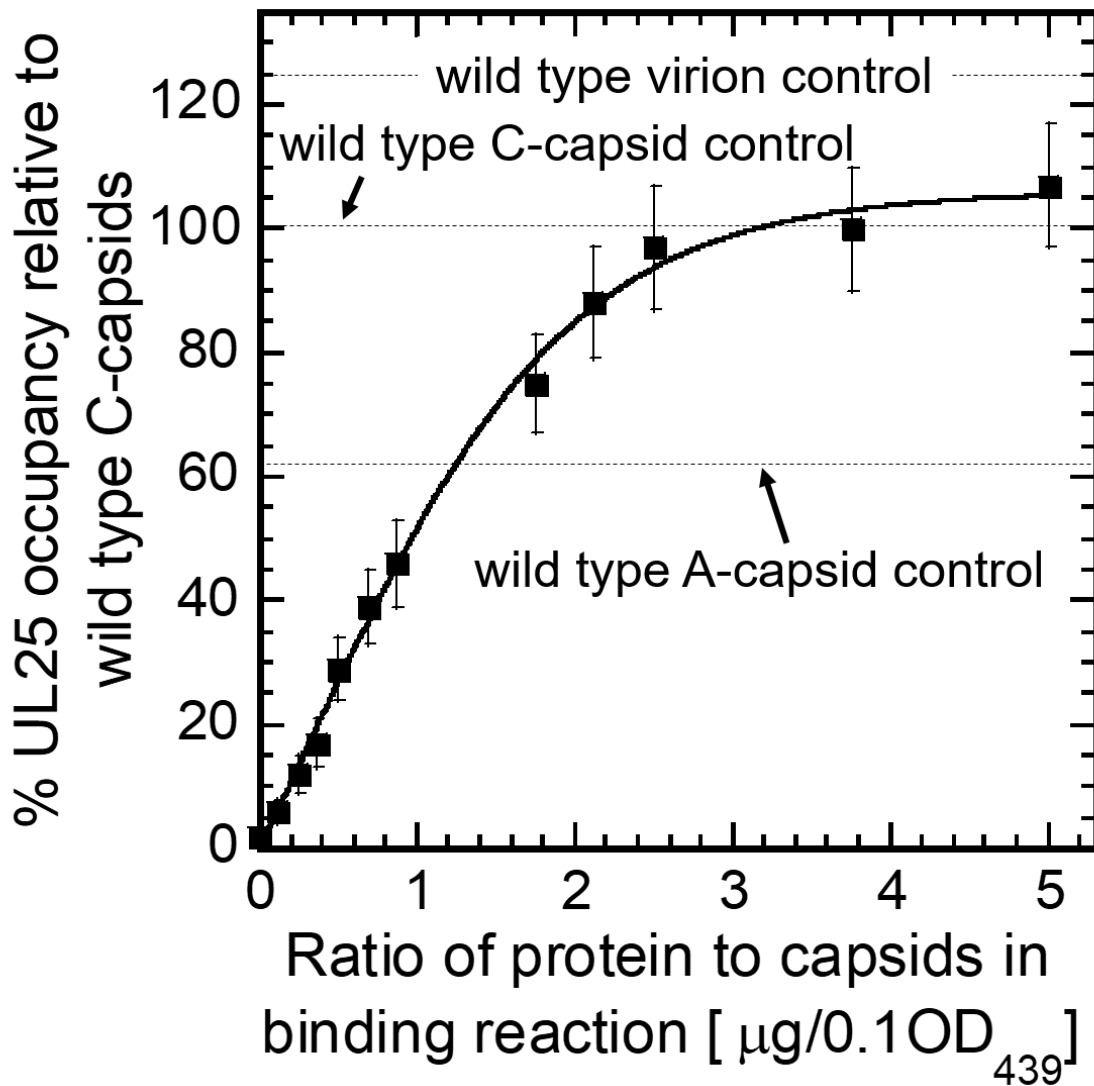


Figure 3.26: The Western Blot was analyzed for UL38 (all capsids have 375 copies of UL38, so difference in band intensities are due to differences in sample concentration – comparing all UL38 bands to a reference band allows quantification of those differences) and UL25. The UL25 bands have varying intensities proportional to the amount of protein present in the binding reaction. Doing this experiment allows for accurate measurements of the relative amounts of UL25 bound per capsid.

References

1. Streletzky, K. A.; McKenna, J. T.; Mohieddine, R., Spectral Time Moment Analysis of Microgel Structure and Dynamics. *J Polym Sci Part B Polym Phys* **2008**, *46*, 771-781.
2. Zimm, B. H., Apparatus and Methods for Measurement and Interpretation of the Angular Variation of Light Scattering; Preliminary Results on Polystyrene Solutions. *J Chem Phys* **1948**, *16*, 1099.
3. Hammouda, B., Probing Nanoscale Structures-the Sans Toolbox. *National Institute of Standards and Technology* **2008**.
4. Freeman, K. G.; Behrens, M. A.; Streletzky, K. A.; Olsson, U.; Evilevitch, A., Portal Stability Controls Dynamics of DNA Ejection from Phage. *J Phys Chem B* **2016**, *120*, 6421-6429.
5. Ghoorchian, A.; Vandemark, K.; Freeman, K.; Kambow, S.; Holland, N. B.; Streletzky, K. A., Size and Shape Characterization of Thermoreversible Micelles of Three-Armed Star Elastin-Like Polypeptides. *J Phys Chem B* **2013**, *117*, 8865-8874.
6. Sae-Ueng, U.; Li, D.; Zuo, X.; Huffman, J. B.; Homa, F. L.; Rau, D.; Evilevitch, A., Solid-to-Fluid DNA Transition inside Hsv-1 Capsid Close to the Temperature of Infection. *Nat Chem Biol* **2014**, *10*, 861-867.
7. Huet, A.; Makhov, A. M.; Huffman, J. B.; Vos, M.; Homa, F. L.; Conway, J. F., Extensive Subunit Contacts Underpin Herpesvirus Capsid Stability and Interior-to-Exterior Allostery. *Nature structural & molecular biology* **2016**.
8. Lander, G. C.; Johnson, J. E.; Rau, D. C.; Potter, C. S.; Carragher, B.; Evilevitch, A., DNA Bending-Induced Phase Transition of Encapsidated Genome in Phage Lambda. *Nucleic Acids Res* **2013**, *41*, 4518-4524.
9. Svergun, D. I.; Koch, M. H. J.; Timmins, P. A.; May, R. P., Part II: Data Analysis Methods. In *Small Angle X-Ray and Neutron Scattering from Solutions of Biological Macromolecules*, First Edition ed.; Oxford University Press: Oxford, 2013.
10. Liu, T.; Sae-Ueng, U.; Li, D.; Lander, G. C.; Zuo, X.; Jönsson, B.; Rau, D.; Shefer, I.; Evilevitch, A., Solid-to-Fluid-Like DNA Transition in Viruses Facilitates Infection. *Proceedings of the National Academy of Sciences* **2014**, *111*, 14675-14680.
11. Ivanovska, I.; Wuite, G.; Jonsson, B.; Evilevitch, A., Internal DNA Pressure Modifies Stability of Wt Phage. *Proc Natl Acad Sci U S A* **2007**, *104*, 9603-9608.
12. Ivanovska, I. L.; de Pablo, P. J.; Ibarra, B.; Sgalari, G.; MacKintosh, F. C.; Carrascosa, J. L.; Schmidt, C. F.; Wuite, G. J., Bacteriophage Capsids: Tough Nanoshells with Complex Elastic Properties. *Proc Natl Acad Sci U S A* **2004**, *101*, 7600-7605.
13. Hutter, J. L.; Bechhoefer, J., Calibration of Atomic-Force Microscope Tips. *Review of Scientific Instruments* **1993**, *64*, 1868.

Chapter 4: Controlled capsid destabilization (DNA ejection)

4.1 Introduction

4.1.1 Why are dynamics important?

Viral fitness¹⁻² is a quantifiable measure of the ability of a virus to transmit from host to host through infection, replication, and survival in the extracellular environment. Improvements in viral fitness are guided by evolutionary trade-offs, like balancing virion stability between infection events against the virions' ability to rapidly uncoat during infection³⁻⁵. The way these trade-offs are balanced determines the timescales of each step of the viral replication cycle. Consider for example the optimization of host-lysis time; short lysis times promote the rapid spread of infection, but longer lysis times allow more new virions to form in each infection cycle⁶. Thus the timescales present in the viral replication cycle influence the success of viral infections, and studies of each dynamic process within the cycle contribute to our understanding of how viruses spread⁷⁻¹¹.

4.1.2 Studying dynamics of specific viral processes

Understanding of viral dynamic processes has been advanced through *in vitro* experiments, which allow for isolation of particular steps in the replication cycle^{7, 11-14}. For example, viral DNA ejection is often studied *in vitro* using phage λ because its membrane receptor, LamB, can be successfully isolated while preserving its function¹⁵⁻¹⁸. When bound to LamB, phage λ ejects its 48.5 kbp of dsDNA by harnessing the tens of atmospheres of DNA pressure stored in its capsid. This ability to trigger DNA ejection *in vitro* allows scientists to focus on particular DNA ejection steps (like the initiation of ejection and the time required for translocation) with highly controlled systems in the absence of other kinetic processes occurring in the background.

4.1.3 Early work on viral DNA ejection dynamics

The first bulk studies of viral DNA ejection dynamics, as measured with light scattering, were published in 2005. The first researchers to employ this technique¹⁹⁻²⁰ used bacteriophage T5, another dsDNA virus with internal DNA pressure, as a model system: by adding the T5 receptor FhuA to a solution of T5 phages, they triggered ejection *in vitro* and monitored the subsequent decrease in intensity. In 2007 this technique was extended phage λ : DNA ejection was triggered by adding LamB to a population of phage λ particles, and the time-resolved decrease in scattered light intensity was recorded^{15-16, 21}. These

techniques found an equilibration time of tens of minutes, which was puzzling considering results from single-molecule experiments on DNA ejection dynamics.

Single molecule studies show that both phage-receptor binding times^{13,22} and the time for complete DNA translocation from a single λ phage were shown to be on the order of seconds¹⁷⁻¹⁸. These observations, while both repeatable and easily explained by the enormous internal DNA pressure powering ejection, were in sharp contrast with the much slower dynamics as measured with LS. To reconcile these order of magnitude time-scale inconsistencies, it was suggested²¹ that LS may measure the dynamics of DNA ejection events within the population of DNA-filled phages rather than the dynamics of single-phage DNA translocation (Figure 4.1). Interpreting the data this way suggests a stochastic delay in initiation of DNA ejection, resulting in a timescale of tens of minutes for genome ejection from an entire population of phages.

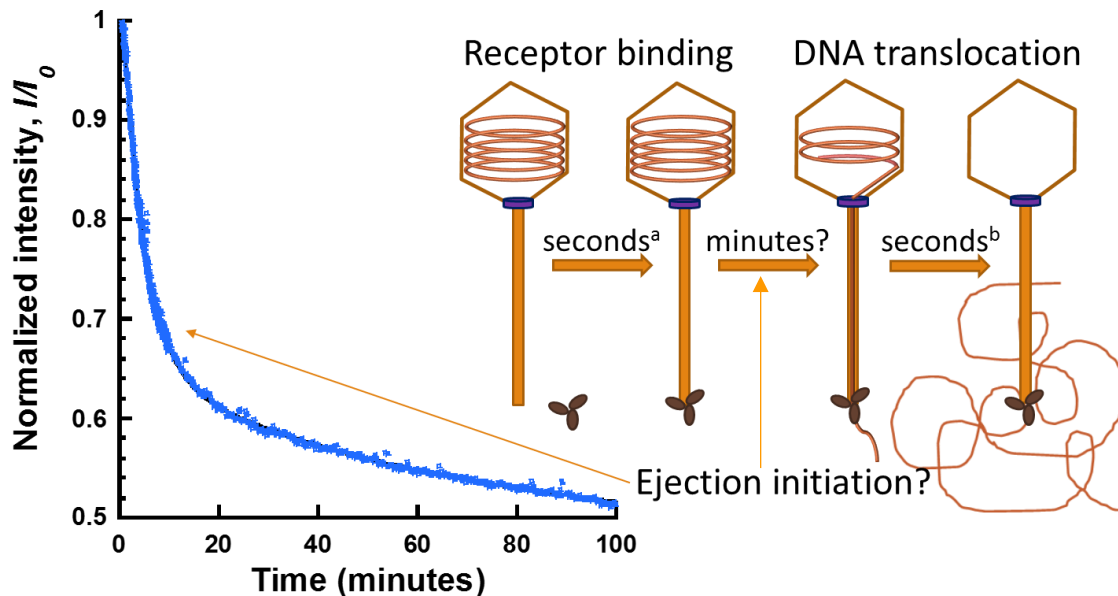


Figure 4.1: The slow dynamics measured by LS do not match the dynamics of receptor binding or DNA translocation, which are both on the order of seconds. Does LS instead measure a minutes-long lag time between receptor binding and initiation of DNA ejection/translocation?

In the next section I combine results from time-resolved experiments with light scattering, small angle X-ray scattering (SAXS), and cryo-electron microscopy (cryo-EM) to prove what the pioneering LS papers speculated – that LS measures the population dynamics of DNA ejection, which are on tens of minutes timescale determined by the temperature-dependent lag between receptor binding and DNA

ejection. These results confirm experimentally, for the first time for phage λ , that the bi-exponential decay in the light scattering intensity observed when LamB is added to phage λ is caused primarily by stochastic DNA ejection events.

4.2 Stochastic ejection of DNA from a population of bacteriophages

As mentioned above, the first step of this project was to establish what exactly is being measured with bulk techniques like light scattering and x-ray scattering. Using these two techniques alone, we could not conclusively prove that we were measuring the population dynamics of DNA ejection. However, by comparing the dynamics measured with the two bulk techniques to those measured with a single molecule technique (cryo-electron microscopy), it became clear that the stochastic nature of DNA ejection events causes the observed slow dynamics. Below I show the results of each experiment separately first, then combined.

4.2.1 LS-measured DNA ejection dynamics: experiment and theory

In an LS measurement of bulk DNA ejection dynamics from a bacteriophage population, the intensity (I) of light scattered by DNA-filled phage particles decreases immediately after mixing with an excess of the solubilized phage receptor^{15-16, 19}. Consider first the raw data from a time-resolved LS DNA ejection measurement, several examples of which are shown in Figure 4.2A. The most apparent result from this plot is that the final I/I_0 value depends on the amount of encapsidated DNA. To explain this we consider, from a theoretical standpoint, why intensity decays during DNA ejection. The observed decay in intensity when LamB is added to the phage solution is the sum of many ($\sim 1E11$, in these experiments) discrete decreases in intensity caused by stochastic single-particle DNA ejections²³. A single phage DNA ejection can be understood using the small-molecule approximation of the Zimm equation²⁴, which relates intensity (I) to molecular weight (M_w) and radius of gyration (R_g): $I \propto M_w / (1 + \frac{1}{3}q^2 R_g^2 + \dots)$, where q is the scattering vector $q = \frac{4\pi n_0}{\lambda} \sin \frac{\theta}{2}$, with index of refraction of solvent n_0 , light wavelength λ , and scattering angle θ . The intensity from a single phage is the sum of I_{capsid} , the constant intensity due to the capsid, and $I_{DNA}(R_g)$, the changing intensity contributed by DNA as it transitions from encapsidated to ejected: $I = I_{capsid} + I_{DNA}(R_g)$.

In Figure 4.2B we use these equations to theoretically track, throughout the ejection process, the normalized intensity, I/I_0 , where I_0 is intensity of the capsid plus the intensity of the encapsidated DNA

(both with $R_g = 30\text{nm}$ and $M_w \sim 31\text{MDa}$) and I is the intensity of the capsid plus the intensity of ejected DNA as it relaxes into solution. For 100% λ -DNA phage, the starting state of capsid and encapsidated DNA has approximately equal intensity contributions from both components [since $I_{\text{capsid}} \approx I_{\text{DNA}(30\text{nm})}$]. On the other hand, the ending state is determined nearly entirely by the intensity contribution from the empty capsid [since $I_{\text{capsid}} \gg I_{\text{DNA}(1\mu\text{m})}$]²³. Thus the normalized intensity drops from $I/I_0 = 1$ before ejection, to $I/I_0 \approx I_{\text{capsid}} / [I_{\text{capsid}} + I_{\text{DNA}(30\text{nm})}] \approx 0.5$ after DNA ejection and relaxation (Figure 4.2B, black line).

Similar calculations were made for phage mutants with less DNA (specifically, with 94% λ -DNA and 78% λ -DNA). In these cases, since according to the Zimm equation above $I_{\text{DNA}(30\text{nm})}$ is proportional to DNA M_w , the capsid scattering always dominates the signal even when DNA is encapsidated [$I_{\text{capsid}} > I_{\text{DNA}(30\text{nm})}$]. Thus, the decrease in normalized intensity is smaller, and I/I_0 after DNA ejection and relaxation is larger (≈ 0.52 for 94% λ -DNA and ≈ 0.56 for 78% λ -DNA, blue and red lines, respectively, on Figure 4.2B).

Notably, the final I/I_0 values predicted theoretically for each phage are in good quantitative agreement with those extrapolated from LS measurements of DNA ejection events (Figure 4.2A). This makes sense... since LS is sensitive to the number of DNA-filled phages, each experiment will always start at 1 (all filled phages) and end at the predicted value (all empty phages).

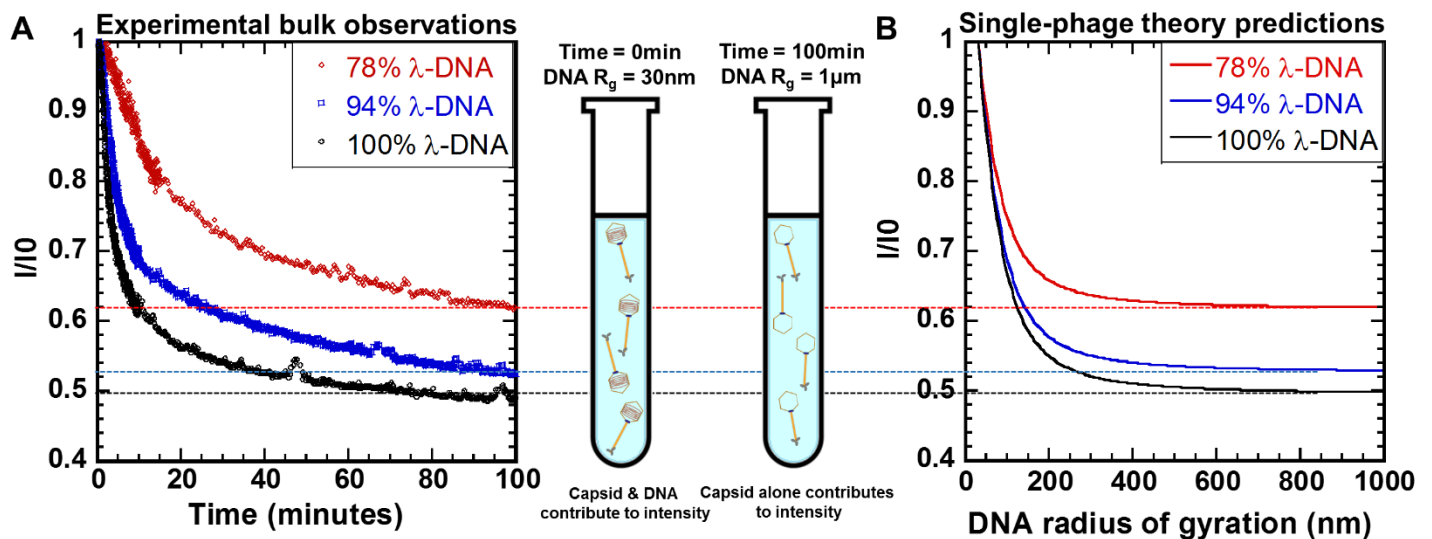


Figure 4.2: The magnitude of the measured decay in normalized intensity depends only on the amount of DNA originally packaged into the phage (A). This magnitude can be predicted theoretically with the Zimm equation by considering the intensity decay caused by a single phage ejection (B). The bulk measurement is the sum of many such discrete decreases in intensity, such that the transition from all filled to all empty capsids yields a drop in normalized intensity which is quantitatively comparable to the single-phage theory.

These calculations are informative, but they do not answer the question of whether the LS-sensitive dynamic process is synchronized ejection from all phages or stochastic ejection events from the population. The beginning and ending points are accurately predicted by single-phage theory, but the theory sheds no light on what happens in between the initial and final states. The question we need to answer next is: what mechanism causes the intensity decay? Is it a slow, synchronized ejection from all phages together (in disagreement with single-molecule studies on DNA translocation) or the more likely stochastic ejection events (Figure 4.3)?

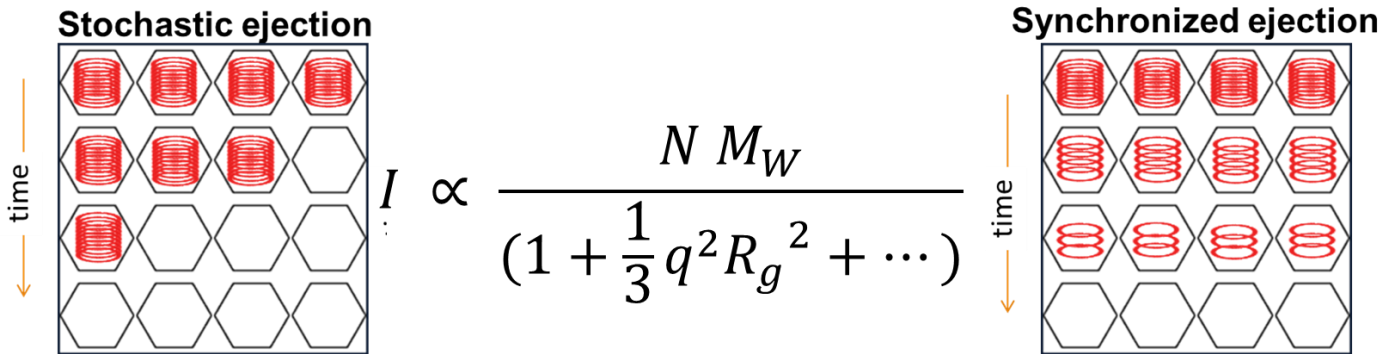


Figure 4.3: The Zimm equation (center) can equally well explain either stochastic ejection (left) or synchronized ejection (right). Additional experiments are needed to confidently decide.

4.2.2 LS-measured DNA ejection dynamics: understanding the whole curve

Before we move to combining LS with other experiments, let's take a closer look at the LS data itself. LS data is well described by a bi-exponential fit, $\Delta I = A e^{-t/\tau_{fast}} + (1 - A) e^{-t/\tau_{slow}}$, with two characteristic time constants $\tau_{fast} = 6.0 \pm 0.1$ minutes and an order of magnitude slower $\tau_{slow} = 49.5 \pm 2.0$ minutes. The pre-exponential factor A is ~ 0.75 , showing that 75% of the scattering intensity change is associated with the much faster process described by τ_{fast} , while the process described by τ_{slow} contributes only 25% of the overall intensity change. In the next sections, we demonstrate experimentally for the first time that the primary scattering intensity decay described by τ_{fast} is caused by stochastic DNA ejection events occurring after binding of LamB receptor to phage λ .

The much slower secondary decay process, described by τ_{slow} , we believe is the slow relaxation of ejected DNA into solution. Considering again the Zimm equation, we look more closely at the contributions to intensity from a single DNA molecule and a single phage capsid as a function of the DNA's radius of gyration. Figure 4.4 shows that the overall intensity contributed by a single phage (black line) decreases during DNA ejection; while the empty capsid provides a constant background intensity, the DNA contribution

to intensity drops from ~ 0.5 to 0 (red line) as DNA transitions from encapsidated ($R_g \sim 30\text{nm}$) to ejected and fully relaxed ($R_g \sim 1\mu\text{m}$). As explained above, initially the capsid ($M_{W,capsid} = 31 \times 10^6 \text{ Da}$)²⁵ and DNA ($M_{W,DNA} = 32 \times 10^6 \text{ Da}$)²⁶, both with $R_g \sim 31\text{nm}$ (λ -capsid radius)²⁷, contribute nearly equally to the total scattering intensity (Figure 3.4, point A on the black curve). After binding with receptor, DNA is ejected from the capsid into the surrounding buffer solution, leaving the empty capsid as the dominant scattering object.

The rapidly ejected DNA, while considerably less dense than encapsidated DNA, likely contributes transiently to the scattering signal since it can exist initially in a semi-condensed state before relaxing into the buffer (condensed ejected DNA coils with $R_g \sim 55\text{nm}$ are observed occasionally in cryo-EM micrographs as shown in Figure 4.4, point B). This condensed ejected DNA state may be created when the $\sim 20\mu\text{m}$ contour length of DNA is rapidly ejected from the tip of the phage tail within seconds¹⁷, which is significantly faster than DNA diffusion away from the phage¹⁶. This rapid ejection/slow diffusion may cause the DNA to wrap around itself at the tip of the tail, burying the free end within a dense and growing ball of ejected DNA. Therefore, the ejected DNA may contribute to the intensity until relaxing to its random coil state ($\sim 1\mu\text{m}$ ²⁸⁻²⁹). At this point the DNA contributes negligibly to the scattering signal and the total intensity plateaus at around $I \sim 0.5$, with the empty capsid alone as the constant source of scattered light intensity (Figure 4.4, point C on the black curve).

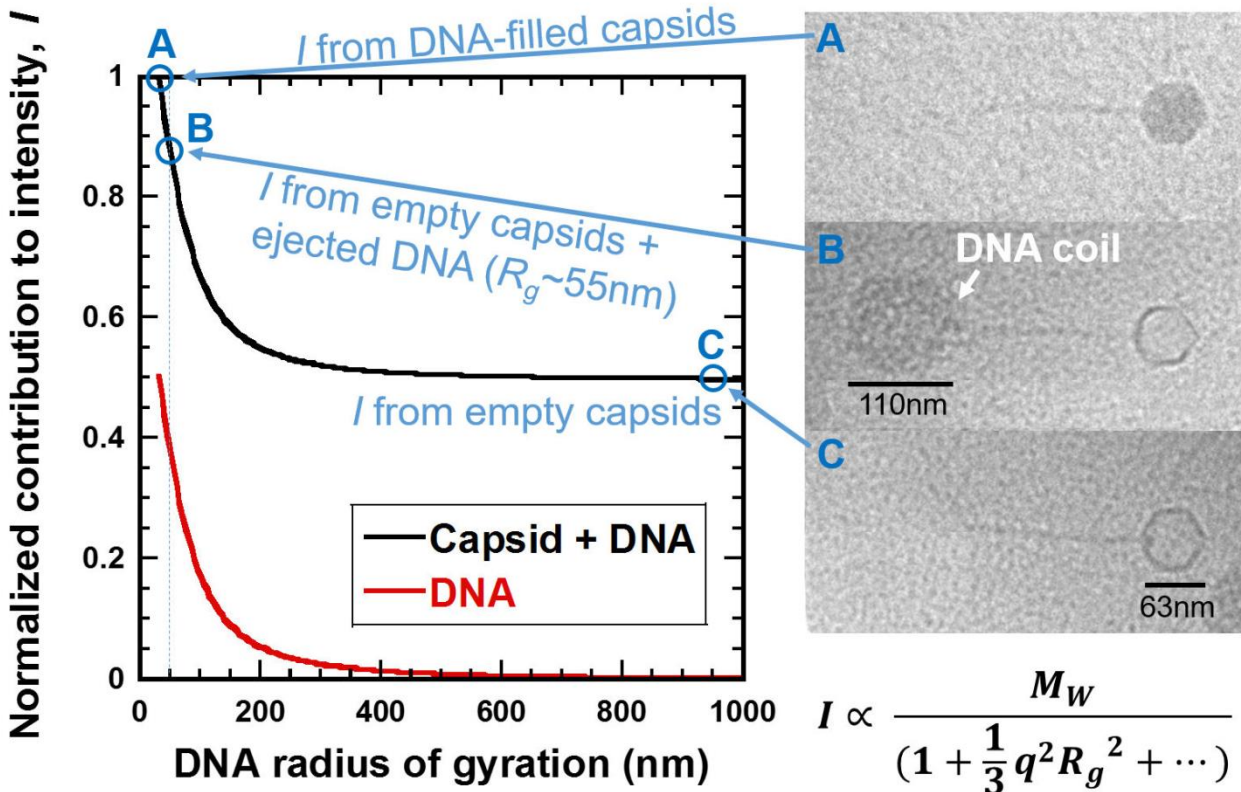


Figure 4.4: A theoretical estimate, based on Eq. 2, of DNA's changing contribution to intensity through the ejection process from a single phage. Point A represents the DNA-filled capsid, where the equally massive DNA and capsid contribute equally to the total intensity. The total intensity is normalized by this point, when both the capsid and DNA have $R_g \sim 31\text{nm}$. Point B represents the intensity immediately after ejection, when DNA may be tightly condensed ($R_g \sim 55\text{nm}$, estimated from the cryo-EM micrograph corresponding to point B and therefore still a significant contributor to the total intensity). Finally, point C represents the final scenario when DNA has fully relaxed and no longer contributes to the total intensity. At this point the intensity is due to empty capsids alone, which contribute constant intensity throughout the ejection process.

Because of low contrast between vitreous ice and DNA, only highly condensed DNA can be visualized by cryo-EM. Therefore, for the thousands of imaged phage particles, the ejected DNA coils present at the tail of phage particle, as seen in Figure 4.4B, are often not visible (on the other hand larger, microns-scale globules of condensed DNA were commonly observed and appear to be aggregates of DNA ejected from many phages). Despite the infrequent observation of tightly condensed single DNA chains, however, it is likely (based on the fact that DNA translocation happens orders of magnitude faster than DNA diffusion) that all ejected DNA molecules are at least loosely condensed immediately after ejection. These initially condensed ejected DNA molecules could contribute transiently to the scattering intensity before fully relaxing in solution (as illustrated in Figure 4.4). The relaxation dynamics of the ejected DNA may be as slow as reptation dynamics of an entangled DNA chain and thus an upper bound for relaxation time can

be estimated with a self-diffusion coefficient of $\sim 6 \times 10^{-3} \mu\text{m}^2/\text{s}^{30-31}$. Therefore, the relaxation-diffusion of a single ejected DNA from $\sim 55\text{nm}$ (tightly coiled) to $\sim 1\mu\text{m}$ (relaxed random-coil) could take up to ~ 35 minutes. This suggests that the LS-measured t_{slow} of ~ 49 minutes could be indeed associated with the relaxation/self-diffusion of ejected DNA molecules.

4.2.3 SAXS-measured DNA ejection dynamics

We use time-resolved SAXS measurements (under conditions identical to the LS experiment described in the preceding section) to provide our first support for the stochastic ejection behavior observed with LS for phage λ . The curves have a complex shape determined by capsid structure (Figure 4.5A). Like LS, SAXS measured scattering intensity is sensitive to the changing density of DNA (for SAXS it is electron density, which is proportional to mass density) during the ejection and relaxation processes. For small particles, SAXS intensity I at scattering vector $q \approx 0$ is proportional to M_w , and thus this $I(q \approx 0)$ value decreases as the DNA ejection from phage and DNA coil relaxation-diffusion processes proceed. We plot the normalized change in $I(q \approx 0)$ versus time in Figure 4.5. Unsurprisingly (since it is essentially the same measurement with a different technique) this curve looks quite similar to the LS curve.

We also analyzed the data in more detail by using linear combination fits, which show that the sample at intermediate times is a mixture of DNA-filled and empty phages. To do this, each intermediate-time I versus q curve is fit with a unique linear combination: $I(t) = f(t) \times I_{initial} + (1 - f(t)) \times I_{final}$. The high quality of these fits (Figure 4.5 yellow curves) confirms that the curves at intermediate times are mixtures of filled and empty capsids. The fitting parameter $f(t)$, is proportional to the fraction, $F(t)$, of DNA-containing capsids in the sample by $F(t) = 0.8f(t)$, which takes into account the DNA ejection by $\sim 20\%$ of phages in the first 1.5 minutes of the experiment. This calculated fraction of filled phages, $F(t)$ is plotted as the red diamonds in Figure 4.5.

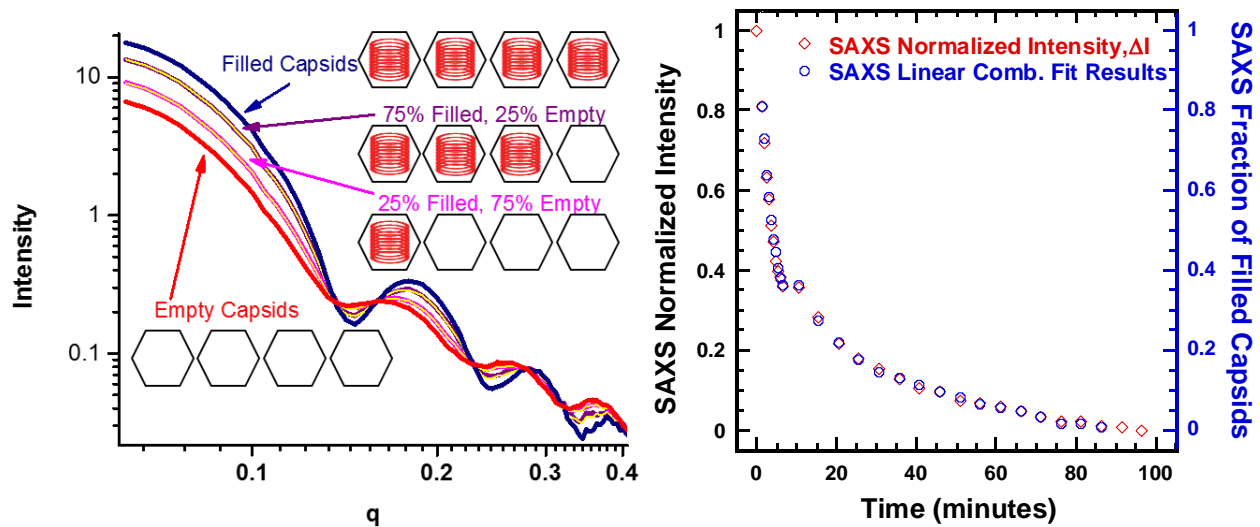


Figure 4.5: The q -dependence of the measured intensity in SAXS has a complex shape determined by the capsid and DNA structure. The DNA structure changes as DNA transitions from encapsidated to ejected and diffused, and thus the shape of the curve also changes throughout this process. In (A) we used the initial curve (blue, measured before triggering ejection) and the final curve (red, measured 100 minutes after triggering ejection) in linear combinations to fit the intermediate curves (magenta and pink, with yellow fits on top). The weight of the initial curve in each fit reveals what fraction of phages were DNA-filled in each intermediate curve. This fraction is plotted in (B), along with the normalized low- q intensity (which is, in principle, data identical to that collected with an LS experiment).

The unique shape of the SAXS intensity curve is determined by the capsid structure and encapsidated DNA structure; thus, as the DNA structure changes during the transition from encapsidated to ejected, the resulting shape of the scattering curve will also change. We used this fact above to “fit” intermediate curves to a linear combination of initial (all DNA-filled capsids) and final (all empty capsids) states, yielding a fraction of DNA-filled capsids at each intermediate step. We took this shape-analysis a step further by comparing the experimentally measured curves to theoretically predicted models.

The unique dependence of I versus q comes, more specifically, from the scattering length density distribution, $\rho(r)$, of scattering objects³². For DNA-filled bacteriophage capsids, this dependence can be approximated with core-shell models where the shell is the capsid and the core is the DNA. In Figure 4.6 we compare the q -dependence near the first minimum for our time-resolved experimental SAXS data with two ejection models (synchronized and stochastic ejection) generated with core-shell modelling (all modelling details are described in the SAXS section of Chapter 2). The two ejection models are: 1) stochastic ejection (illustrated in Figure 4.6A, top) and 2) synchronized ejection (illustrated in Figure 4.6A, bottom). Stochastic ejection is modelled with linear combinations of modelled curves for DNA-filled and solvent-filled protein shells; the results are shown in Figure 4.6C middle panel, where the weighting of each

curve is described by the ratio Filled:Empty. Synchronized ejection is modelled by using only a model for DNA-filled protein shells, but changing the density of DNA filling the core; the modelled curves are shown in Figure 4.6C bottom panel, with DNA density described by “% DNA inside”. For reference, the experimental data (zoomed into the same q range) is shown in Figure 4.6C top panel.

Several important observations can be made from this comparison. First, we notice a systematic shift toward lower q -values in the position of the first minimum in the synchronized ejection model which is not present in either the experimental data or the stochastic ejection. Furthermore, we observe so-called isosbestic points, or points of constant intensity at fixed q values, on both sides of the first minimum in both the experimental data and the stochastic ejection model (indicated with dotted lines in Figures 4.6C top and middle panels), but not in the synchronized ejection model. Isosbestic points indicate that a sample contains a changing mixture of two distinct scattering species³³ (here, DNA-filled capsids and empty capsids), where changes in the concentrations of each species are linearly related (i.e. one DNA filled-capsid becomes one empty capsid). The existence of isosbestic points in the experimental data and the stochastic ejection model strongly support our conclusion that the sample is an evolving mixture of populations of DNA-filled and empty capsids rather than a uniform sample of synchronously DNA-ejecting particles (i.e., identical partially filled capsids).

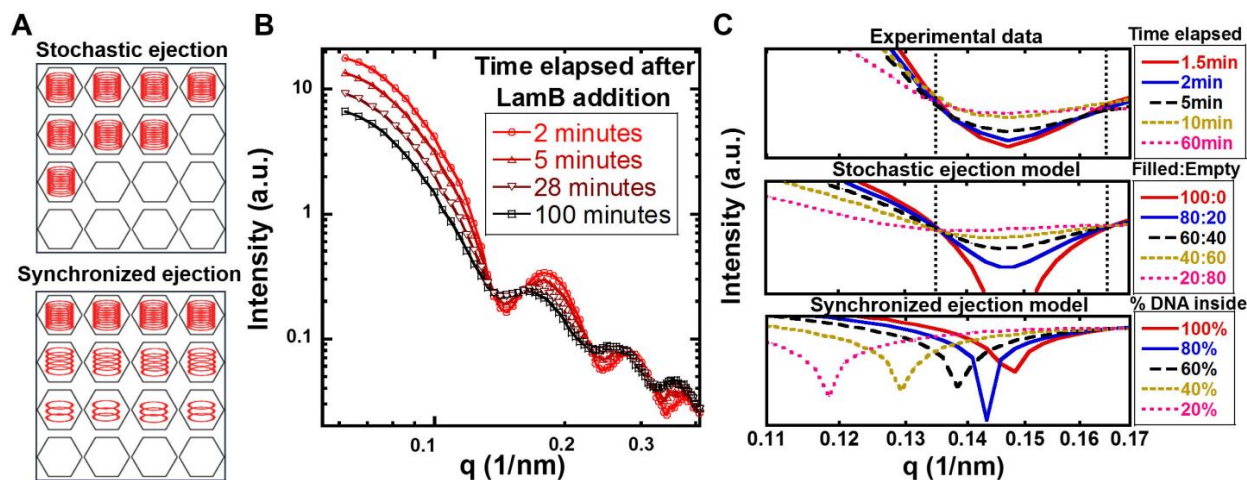


Figure 4.6: (A) An illustration of stochastic ejection events versus synchronized ejection. (B) The measured SAXS I versus q data (lines connecting points to guide the eye) shows that $I(q \approx 0)$ decreases during the DNA ejection and diffusion processes, indicating that the average molecular weight of scattering particles decreases as the system progresses toward one with all empty capsids and diffuse DNA. (C) The presence of fixed intensity points at certain q values (isosbestic points) and an unchanged q -position of the first minimum in the experimental SAXS curves progressing with time indicates that the sample is a mixture of DNA-filled and empty phages. The experimental SAXS curves versus time are compared to core-shell models of stochastic ejection events and synchronized ejection. Our data agrees well with the stochastic ejection model.

4.2.4 Cryo-TEM-measured DNA ejection dynamics

The final technique used in our pursuit to uncover what is measured with bulk DNA ejection experiments, like LS, was cryo-transmission electron microscopy. With cryo-EM we were able to trigger ejection by adding LamB (with conditions identical to those which LS and SAXS experiments were performed under), then stop the ejection process in its tracks by flash-freezing an aliquot of the sample at a chosen time. When the sample is frozen, all biological activity is suspended – receptor-bound DNA-filled phages which still contain their DNA will not eject as long as the sample remains frozen. To gain a unique insight into the population dynamics of DNA ejection, as stopped the ejection process by freezing at nine different time-points. The results of this time-sampling are shown in Figure 4.7 below.

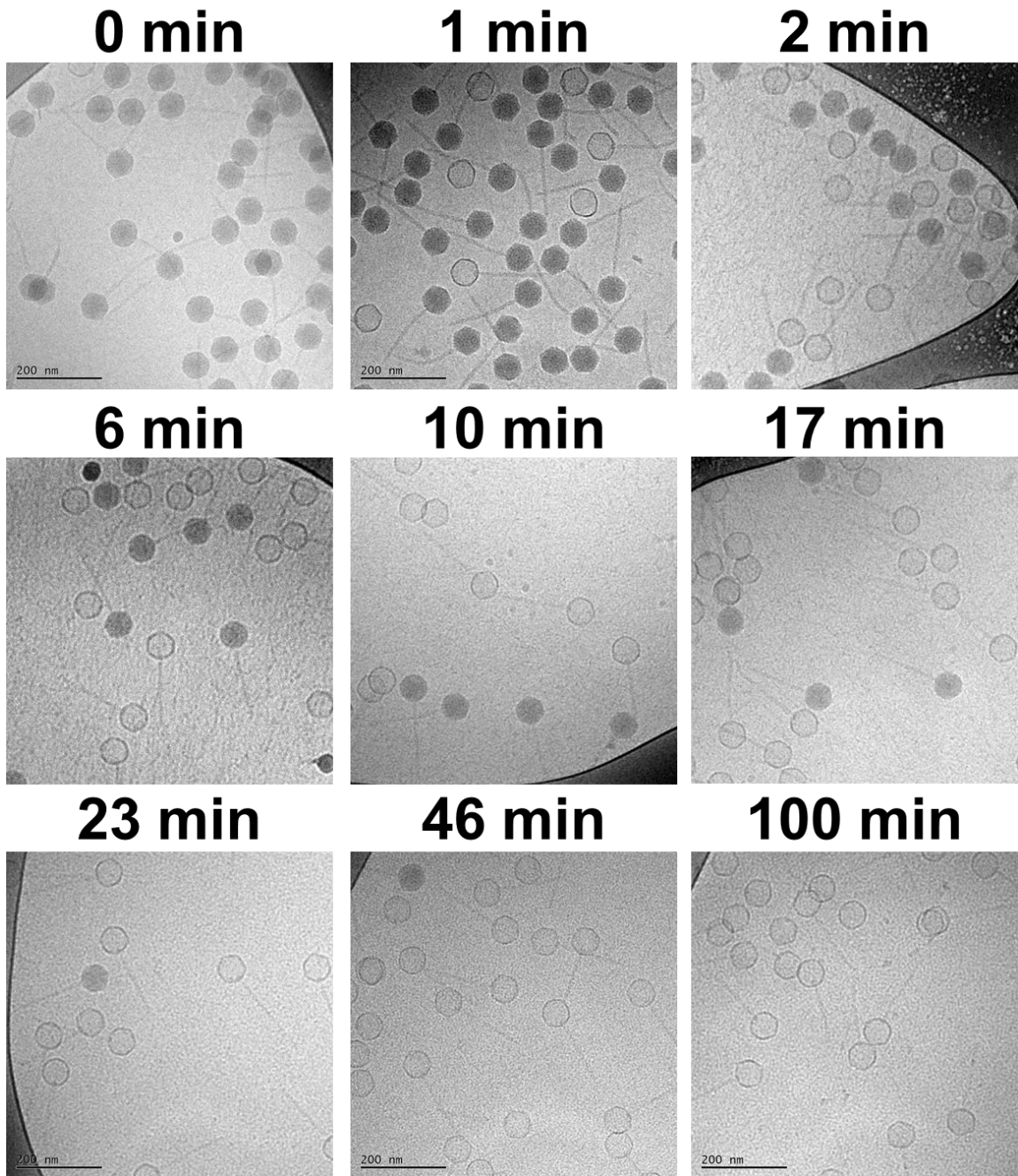


Figure 4.7: Representative cryo-TEM micrographs for every timepoint sampled show that the number of DNA-filled phages decreases with time in a stochastic fashion. A significant number of phages still remain filled with DNA for tens of minutes after binding to the receptor – in agreement with LS dynamics.

For each time-point sampled with cryo-TEM, we measured 500-800 unique particles and determined whether they were filled or empty. In Figure 4.8B we show the quantified results of this single-

molecule ejection dynamics test – the number of DNA-filled phages decreases exponentially, with a characteristic time of 6.4 ± 1.5 minutes (in good agreement with the LS-measured 6.0 ± 0.1 minutes).

In addition to DNA-filled and empty phages, many micrographs (particularly at shorter times) showed a considerable number of “in-between” phages (Figure 4.8A). We can only assume these are partially-filled particles frozen at just the right moment such that we caught a “snapshot” of the ejection burst. Since we know the DNA-translocation process is short-lived (only ~10 seconds), the chance of catching and freezing the event is small. In fact, that chance is proportional to the number of phages ejecting per unit time...that is, the derivative of the ejection event dynamics. Since the decay of fully-filled particles as a function of time is exponential, we would expect the decay of partially-filled particles to also be exponential with the same time constant. Indeed, when we counted up these partially-filled particles for each time point we found again a single exponential decay with a time constant of 5.8 ± 1.2 minutes.

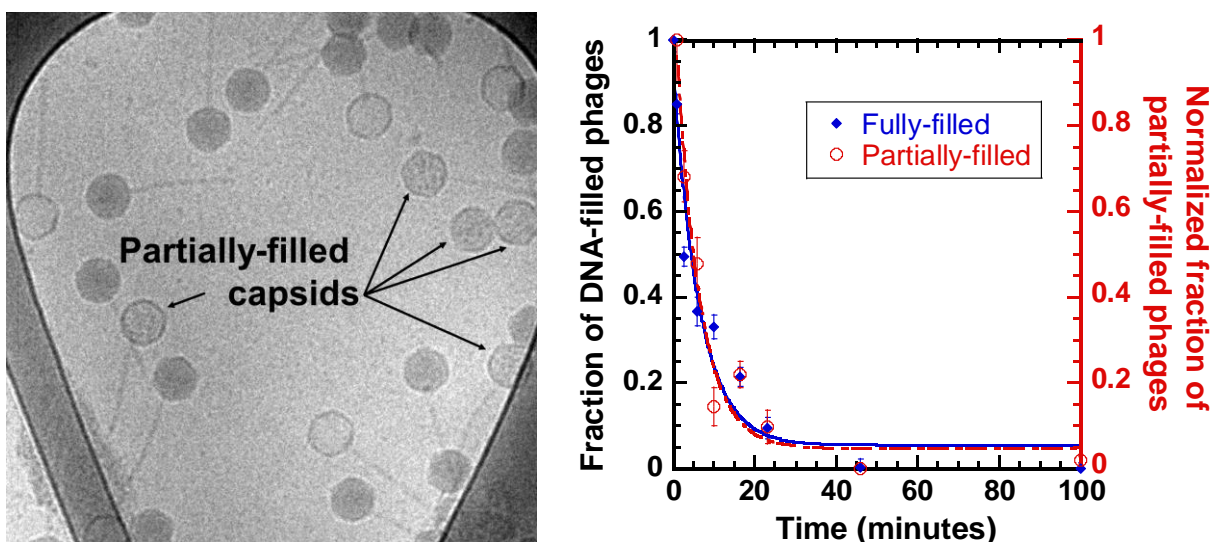


Figure 4.8: (A) At shorter times a significant number of phages cannot be classified as DNA-filled OR fully empty – they seem to be partially filled, as if caught and frozen exactly in the moment of a DNA ejection burst. (B) Analysis shows that the fraction of both fully- and partially-filled phages (normalized to start at 1) decay exponentially with a time constant of ~6 minutes, in excellent agreement with the fast time constant measured in LS experiments.

4.2.5 Combining all to show stochastic DNA ejection behavior

We have now see, independently, the results of three unique experiments which measure the dynamics of DNA ejection from phage λ . All that remains is to present the results together and show that the combined data proves that the DNA ejection event is stochastic, and that the minutes-long average lag time created by this stochasticity is responsible for the slow decay of the measure LS ejection dynamics. Figure 4.9 shows these results plotted together (LS and SAXS data is normalized from 0 to 1 for comparison

with cryo-TEM data). The plot shows that DNA ejection is a stochastic process quantified by the single-exponential cryo-EM data and by the fast process time constant, τ_{fast} , of the bi-exponential decays measured with LS and SAXS.

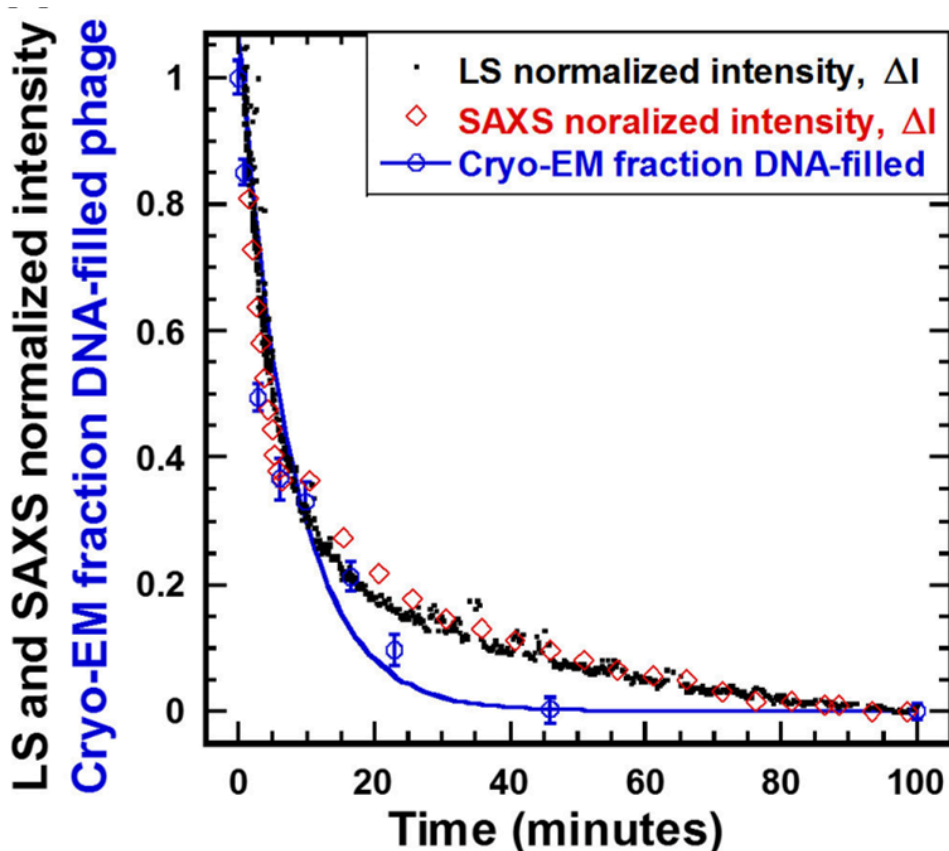


Figure 4.9: All three techniques show an exponential decay process with a time constant of ~6 minutes. This is the average lag time between receptor binding and DNA ejection.

While the stochastic ejection events constitute a single-exponential process (as confirmed by our cryo-EM data here as well as previously reported fluorescence microscopy^{17, 34} results), bulk experiments like LS are also sensitive to secondary processes such as the diffusion of ejected DNA (discussed in Section 4.2.1). Thus the quantification of stochastic DNA ejection dynamics is improved by accounting for such background processes during data analysis of bulk measurements. Similar observations of LS-measured stochastic DNA ejection events in vitro have also been made for bacteriophage T5²². T5, however, pauses during its genome translocation process³⁵, unlike λ which ejects continuously.

The minutes-long stochastic delay in phage λ genome ejection (despite essentially instantaneous phage-receptor binding^{13, 22}) is orders of magnitude longer than the time necessary for λ DNA translocation¹⁷ and is on a similar time-scale as the one-step phage replication cycle⁷. It may therefore play a significant role in the overall phage population dynamics during infection. Yet, the mechanism leading to the stochasticity has not been investigated and remains unclear. In the next section we investigate the nature of the ejection stochasticity by using our LS-based assay to analyze the effect of portal vertex thermal stability^{5, 36} on dynamics of viral ejection events.

4.3 What causes the lag between receptor binding and DNA ejection initiation?

The results of the previous section, summarized in Figure 4.9, demonstrate that the LS-measured time constant τ_{fast} corresponds to the average lag-time for initiation of DNA ejection. We now use our LS-assay to investigate the mechanism leading to the minutes-long delay in dynamics of initiation of DNA ejection events. As described in the introduction, pressure driven DNA ejection out from bacteriophage capsids occurs through a portal vertex, which connects the phage tail to the capsid³⁷. The same portal vertex is also the pathway for motor-assisted DNA packaging during virion assembly³⁸. It has been suggested that once the DNA is packaged, the pressurized genome is retained within the capsid by the action of a portal “plug” protein³⁹⁻⁴² and/or by the portal ring/neck structure forming a valve blocking the DNA from exiting⁴³⁻⁴⁶. Here we refer to these structures as a *portal vertex* or *portal* that prevents spontaneous DNA loss which results in inactivation of phage particles.

4.3.1 Portal as the Achilles' heel of phage lambda

Bauer et al³⁶ recently demonstrated that portal vertex stability is determined by the delicate force balance between the portal vertex strength and the internal DNA pressure. That work showed that the force balance can be perturbed either *mechanically*, by an increase in the capsid's DNA pressure, or *thermally* by destabilizing the portal structure at higher temperatures³⁶. At a critical level of thermo-mechanical destabilization, the portal opens and DNA is ejected, even in the absence of a specific phage receptor⁵. Another study⁵ from Bauer et al (results reproduced in Figure 4.10), found that such heat-triggered DNA ejection from wild-type (WT) DNA length phage λ occurs at $\sim 70^\circ\text{C}$. On the other hand, the temperature for heat-triggered DNA ejection for an underpackaged λ mutant (with 78% of WT DNA length, resulting in a lower DNA pressure of 15 atm compared to 25 atm in a WT DNA phage λ ⁴⁷) is nearly 5°C higher⁵. Since

the mutant is otherwise identical to the WT phage, this shift up in DNA ejection temperature suggests that the heat-triggered ejection mechanism relies on mechanical destabilization of the portal exerted by DNA pressure in the capsid.

In the same study⁵, the authors measured the heat-triggered ejection from WT phage P22 and a P22 mutant with a weakened portal complex (keeping the packaged DNA length and therefore pressure unchanged). Indeed, the temperature for heat-triggered ejection was $\sim 5^\circ\text{C}$ smaller for the weakened-portal P22. These findings strongly suggest that heat-triggered ejection occurs when the portal opens due to critical destabilization by heat and DNA pressure. In the following sections we argue that receptor-triggered ejection is also sensitive to the critical thermo-mechanical destabilization necessary to open the portal. However, receptor binding significantly lowers the threshold for this critical destabilization, allowing DNA ejection events to proceed at a rate high enough for efficient infection. The details supporting this argument are below.

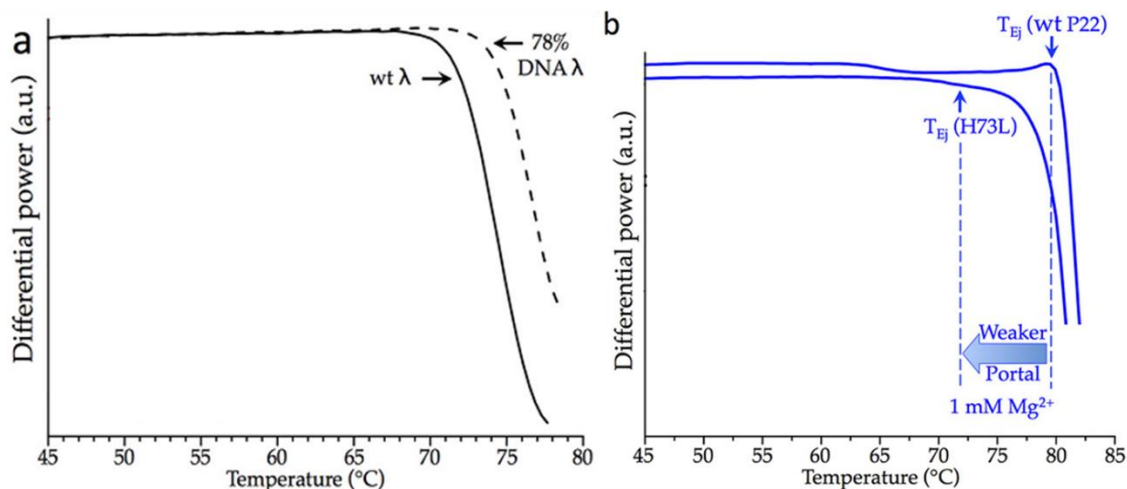


Figure 4.10: Our recent publication³⁶ showed that DNA ejection can be triggered, in the absence of the virus receptor, though heat. The temperature of ejection is determined by the thermo-mechanical stability of the portal complex. This stability is reduced for viruses with larger internal pressure (for example, comparisons of 100% and 78% λ -DNA phages in A) or for viruses with weakened portal complexes (for example, comparisons of wild type P22 and its H73L mutant with a modified portal).

4.3.2 Temperature-induced destabilization of the portal

In this work the DNA ejection through the portal from WT phage λ is triggered by addition of LamB receptor under physiological conditions mimicking those of *in vivo* infection. As described in the previous

section, despite the addition of a specific phage λ receptor, the DNA ejection does not occur instantaneously and simultaneously from all phage particles. Instead we found a significant stochastic lag-time preceding ejection events. In this section I discuss how the rate of DNA ejection events increases with increasing temperature.

Figure 4.11 shows the results of LS ejection dynamics experiments at a range of temperatures from 15°C to 45°C, for both wild type (100% λ -DNA) phage and 78% λ -DNA phage (note that 78% λ -DNA phage is produced by removing 22% of the λ which is non-essential for viral replication. The mutant can still efficiently package DNA⁴⁸ and undergo lytic growth⁴⁹). The data presented here is stretched from 0 to 1 to allow for direct comparison between 100% and 78% λ -DNA phages (which, due to their smaller DNA content, exhibit a less dramatic change in intensity throughout the ejection process, as shown in Section 4.2.1). The details of this normalization are described Chapter 2. The data show that the population dynamics of DNA ejection, for both phages, becomes dramatically faster as temperature is increased from 15°C to 45°C.

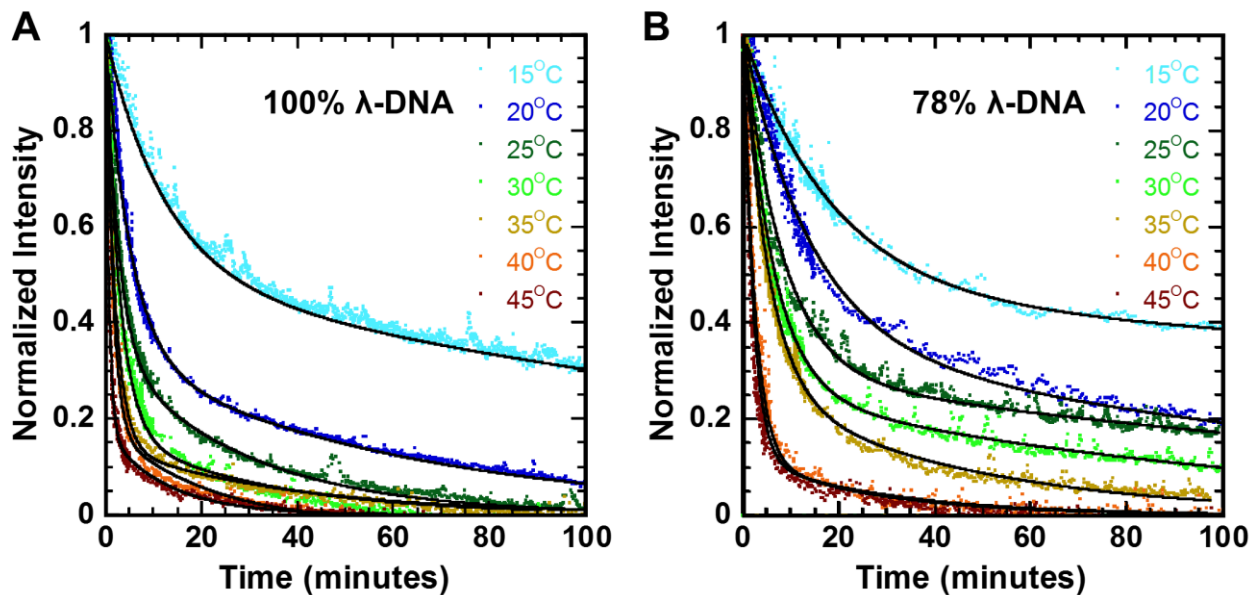


Figure 4.11: (A) and (B) show intensity curves for 100% λ -DNA and 78% λ -DNA (all in TM-20), which demonstrate the striking effect of temperature on population dynamics of DNA ejection. Faster dynamics are a result of temperature-induced destabilization of the portal complex, which leaves the portal more prone to quickly opening upon receptor binding.

As temperature is the only parameter changed in these sets of experiments, the data gives unique insight into what direct effect temperature has on the physical-chemical process of DNA ejection. We know from the heat-triggered DNA ejection experiments of Bauer et al.^{5, 36} that DNA ejection can occur at high temperatures, even in the absence of LamB, when the portal opens in response to a critical thermo-mechanical stress exerted on it from the DNA and the environment. While increasing the temperature destabilizes the portal vertex structure against the internal DNA stress^{5, 36}, it does not affect the average internal DNA pressure on the capsid walls. Figure 4.12 shows recently reported^{34, 50} SAXS data for (A) DNA interaxial spacing as a function of temperature measured inside WT phage λ and (B) osmotic pressure as a function of DNA interaxial spacing measured for bulk DNA (both experiments were done with identical buffer conditions as LS-measurements). Figure 4.12A shows that average interaxial spacing of encapsidated DNA is constant with temperature while Figure 4.12B confirms the temperature independent relationship between pressure and interaxial DNA-DNA spacing, between 5 and 50°C at interaxial spacings corresponding to that of viral capsids⁵¹⁻⁵³. These plots together suggest that the average internal DNA pressure within a capsid is unchanged with temperature. Thus, by increasing the temperature we isolate the effect of thermal destabilization of the portal vertex on ejection dynamics while keeping the capsid DNA pressure unaffected.

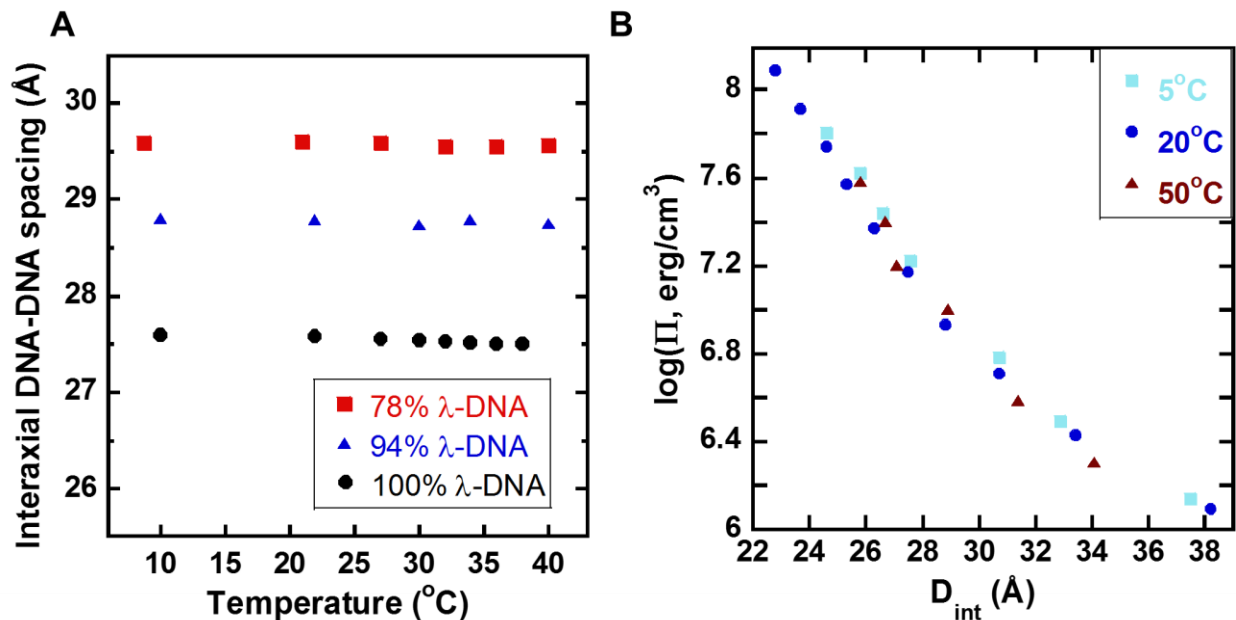


Figure 4.12: (A) shows that the interaxial spacing between neighboring DNA strands is independent of temperature for the phages studied here, while (B) indicates that, at least for bulk DNA, DNA pressure for a fixed interaxial spacing is independent of temperature. Data in (A)³⁴ and (B)⁵⁰ have been reprinted from our recent publications, and error bars are the size of the points.

So we see that by controlling temperature, and consequently the thermal stability of the portal complex, the population dynamics of DNA ejection dynamics can be controlled. This is already an empirically known fact – researchers have, for many years⁵⁴, taken advantage of slow population dynamics at low temperatures by pre-incubating phages with their receptor at 4°C prior to experiments. Such treatment allows binding of the two components but, due to the high thermal stability of the portal complex, significant DNA ejection does not occur until the temperature is raised. Indeed, extrapolations of our data (based on the linear fits to the Arrhenius plots discussed in the next section) suggest that, when bound to LamB, the half-life of DNA-filled λ phages at 4°C is long-lived (15 minutes for 100% λ -DNA and nearly an hour for 78% λ -DNA).

4.3.3 Pressure-induced destabilization of the portal

While the plots in the previous section show unequivocally that DNA ejection dynamics depend strongly on temperature, the shapes of the curves also suggest that genome length influences the observed dynamics. This trend becomes clearer when the normalized intensity as a function of time is plotted for different genome lengths at a constant temperature, as in Figure 4.13. This plot demonstrates that phages packaged with more DNA, and thus storing more internal energy as DNA pressure, have both sharper initial intensity decays and smaller final baselines (indicating fewer DNA-filled phages remain 100 minutes after receptor binding). These characteristics both indicate faster DNA ejection dynamics. This difference in dynamics is quantified by fitting the normalized data to a biexponential curve (described in Materials and Methods), from which we extract the half-life of DNA-filled phages.

The results of curve fitting are shown in Figure 4.13B, which illustrates a pronounced dependence of the half-life on genome length. Indeed, the half-lives measured for 78% λ -DNA phages are approximately two times longer than those measured for 100% λ -DNA phages throughout much of the temperature range. While measured less extensively, the population dynamics of 94% λ -DNA phages also fit the pattern: the measured dynamics at 20 and 25°C are consistently between those of 78% and 100% λ -DNA phages. This plot also shows again, in a more quantitative manner, the strong dependence of dynamics on temperature: for both 100% and 78% λ -DNA phages, the half-life of receptor-bound DNA-filled phages exhibits a striking order of magnitude increase as temperature drops from 45°C to 15°C.

It is interesting, when considering the factor of two difference in $\tau_{1/2}$ for 78% and 100% λ -DNA phages, to also consider the factor of two difference in pressure for these phages⁴⁷ (measured pressures of ~15atm and ~30atm for 78% and 100% λ -DNA phages, respectively). This relationship between pressure and half-life suggests that the measured half-life is inversely proportional to the internal DNA pressure which powers ejection. Such a scenario could explain why strongly underpacked mutants (with genome lengths smaller than 75% λ -DNA) are relatively non-infectious⁵⁵; a sufficiently low pressure may increase the half-life, and thus decrease the rate of DNA ejection events, to the point that infection is too inefficient to succeed.

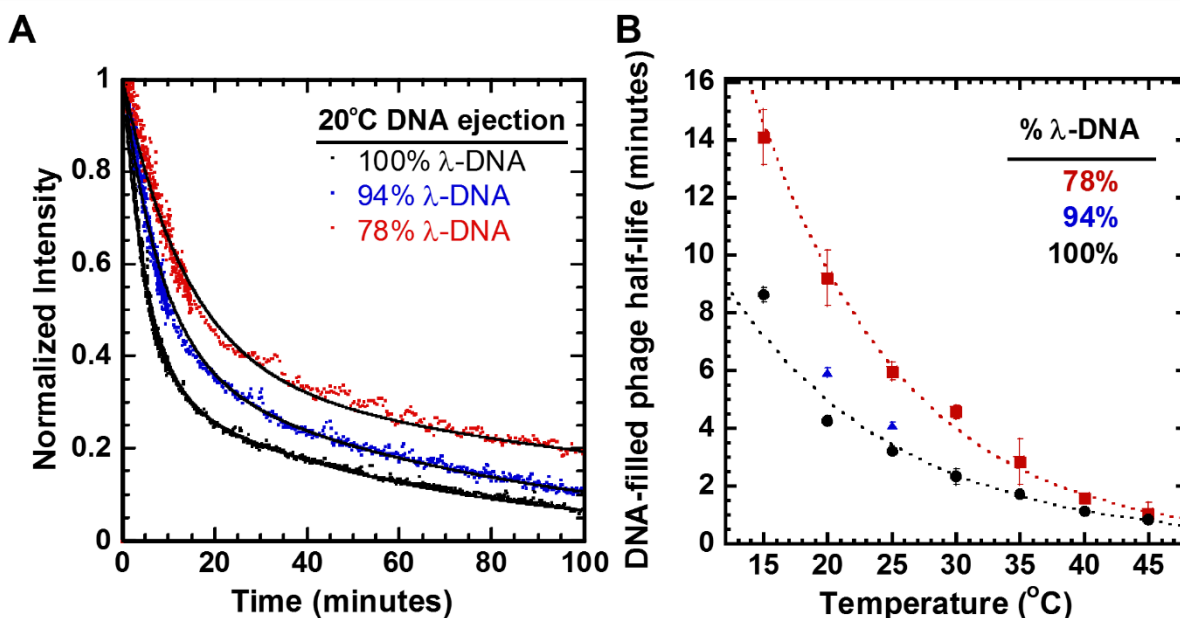


Figure 4.13: DNA ejection dynamics are faster for more highly pressurized phages, as evidenced in (A) by the sharper initial intensity decay and smaller baseline; and in (B) by the quantified half-life of DNA-filled phages. All experiments in this figure were performed in TM-20. Curves in (B) are drawn only to guide the eye.

To identify the source of the observed factor of two in half-lives measured for 78% and 100% λ -DNA, I calculated the activation energy associated with the ejection event by fitting the data to the linearized Arrhenius equation, $\ln(1/\tau_{fast}) = \frac{-E_a}{k_B T} + \ln A$. (Note that I included only 20°C to 45°C data in the fit, since the 15°C falls far the linear trend and, furthermore, there have been reports that ejection is blocked at 15°C). The Arrhenius plot is shown in Figure 4.14A for 78% and 100% λ -DNA phages in TM-20, and the results are summarized for all parameters in Table 4.1. The results show that there is a small but statistically significant difference between the slopes for the different genome lengths: to eject DNA, 78% λ -DNA

phages in TM-20 must overcome an activation energy barrier of 1.13×10^{-19} J/virion, or $26.3 \text{ k}_B T_{37^\circ\text{C}}$ thermal energy units, compared with the smaller barrier of 0.86×10^{-19} J/virion, or $20.0 \text{ k}_B T_{37^\circ\text{C}}$, which 100% λ -DNA phages are subject to.

Thus a decrease in genome length from 100% to 78% λ -DNA decreases the pressure by a factor of two and increases the ejection activation energy barrier by about 31%. This in turn increases the half-life of receptor-bound, DNA-filled phages by a full factor of two. To understand this result we return to our knowledge that DNA pressure pushing on the capsid walls and portal complex destabilizes the portal, making it more prone to opening. In terms of energies, this means that a smaller DNA pressure corresponds to a less energetic initial state of the DNA. This leaves the phage further from the transition state and increases the activation energy barrier preventing ejection (illustrated in Figure 4.14B).

As mentioned above, such a pressure-dependent energy barrier has already been observed for heat-triggered DNA ejection, where the temperature is increased until there is sufficient thermal energy to open the portal, even in the absence of receptor^{5, 36}. In that case, the authors found that such heat-triggered DNA ejection from 100% λ -DNA phages occurs at $\sim 70^\circ\text{C}$ while for 78% λ -DNA phages the temperature of ejection is nearly 5°C higher. This shift up in heat-triggered DNA ejection temperature corresponds to a larger activation energy: for 100% λ -DNA phages the measured activation energy is $3.5\text{E-}19$ J/virion ($82 \text{ k}_B T_{37^\circ\text{C}}$), while it is $4.9\text{E-}19$ J/virion ($114 \text{ k}_B T_{37^\circ\text{C}}$) for 78% λ -DNA phages (TM-20, illustrated in Figure 4.14B and summarized in Table 4.1). This suggests that the heat-triggered ejection mechanism relies both on thermal destabilization as well as mechanical destabilization by DNA pressure exerted on the portal complex. When there is less DNA pressure available to destabilize the portal complex, the phage must consume more energy from the environment to thermally destabilize the portal and eject DNA.

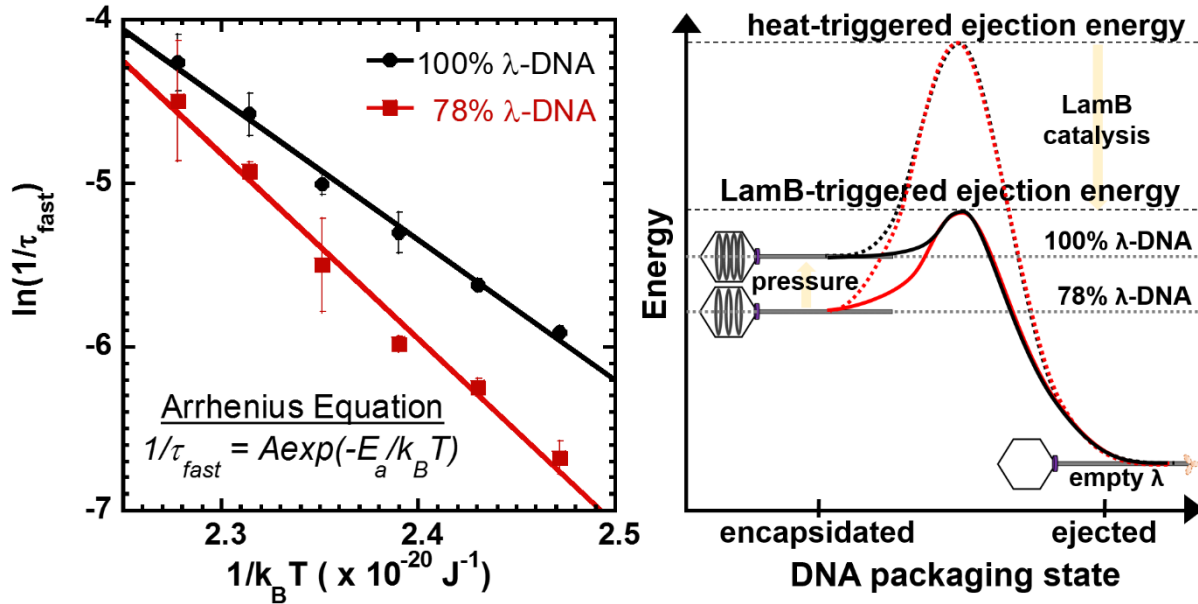


Figure 4.14: (A) The measured rates of ejection are analyzed with the Arrhenius equation to extract the DNA ejection activation energy, which depends on pressure. Since the underpacked 78% λ -DNA phage has a lower initial energy state compared to 100% λ -DNA phage, it must consume more energy from the environment to reach the transition state and open the portal to allow DNA ejection. This concept is illustrated in the cartoon (B), along with a similar effect observed for heat-triggered ejection (energy levels are not drawn to scale).

We suggest that a similar mechanism is present in receptor-triggered ejection as well, but with the caveat that the energy level of the transition state is greatly reduced when the receptor is introduced. This receptor-mediated ~ 4 -fold decrease in the energy level of the transition state allows DNA ejection to occur efficiently at physiological temperatures—the receptor acts as a catalyst for the ejection reaction to occur.

Table 4.1

		5mM	20mM
E_a for receptor-triggered ejection ($k_B T_{37^\circ C}$ thermal energy units)	100%	20.4 ± 1.2	20.0 ± 0.8
	78%	28.0 ± 1.8	26.3 ± 1.5
E_a for heat-triggered ejection* ($k_B T_{37^\circ C}$ thermal energy units)	100%	79 ± 5	82 ± 12
	78%	86 ± 9	114 ± 14
Half-life at 4°C (min) (extrapolated from Arrhenius plot)	100%	15	15
	78%	59	50

*Heat-triggered ejection activation energies are reprinted from Bauer et al³⁶.

4.3.4 Electrostatic DNA-DNA friction and ejection dynamics

In addition to varying the temperature and genome length, we also varied the $MgCl_2$ concentration, another parameter known to influence DNA pressure. Internal DNA pressure is determined by the balance

between bending energy and electrostatic interaction energy of the encapsidated DNA^{53, 56}. Increasing salt concentration can change this balance; the added divalent salt molecules screen more negative charges along the length of DNA, reducing the DNA-DNA electrostatic repulsion. In phages where the DNA is less tightly packaged (such as 78% λ -DNA phage), this reduction in interstrand repulsion allows neighboring DNA strands to move closer together, relieving some of the bending stress and leading to a less pressurized state of encapsidated DNA⁵⁷⁻⁵⁸. With this in mind, we varied the $MgCl_2$ concentration between 5mM and 20mM to probe its effect on DNA ejection population dynamics.

We were surprised to find that, at least in the Mg^{2+} concentration range studied here, ionic strength seemingly has no impact on the measured ejection event dynamics or energetics (see Figure 4.15 and Table 4.1). However, with the genome-length dependence of the dynamics as a reference, this can make sense: while for 78% and 100% λ -DNA phages there is a factor of two difference in pressure which causes a factor of two difference in dynamics, there is no equivalently large difference in pressure when changing the Mg^{2+} concentration between 5 and 20mM. Decreasing the genome length from 100% to 78% λ -DNA leaves a lot more space in the capsid for the genome to expand into; this greatly reduces both the bending energy and the electrostatic interaction energy, leading to the factor of two decrease in pressure⁴⁷. On the other hand, for 100% λ -DNA phages, increasing salt concentration may indeed reduce electrostatic repulsion but, since the DNA interaxial spacing is already very small, this charge screening does not reduce the DNA-spacing (or, consequently, the bending energy) and thus the pressure is left unchanged. For 78% λ -DNA phages the picture is somewhat different due to the significantly larger interaxial spacing between neighboring DNA strands. In this underpacked mutant, increasing salt screening by adding more Mg^{2+} does decrease DNA-DNA interaxial spacing and relax some of the bending stress. However this decrease is small (only about 0.3\AA ⁵⁷) and, according to our estimates based on osmotic pressure versus interaxial spacing for bulk DNA⁵⁷⁻⁵⁸, should correspond to a reduction in DNA pressure of only $\sim 1-2\text{atm}$ ⁵⁸. Thus, instead of a decrease of $\sim 15\text{atm}$ (as observed when genome length is decreased), increasing salt concentration from 5 to 20mM only decreases the pressure by a few atm. Thus, we would expect that increasing the salt concentration would produce a correspondingly smaller (order of magnitude smaller) increase in half-life compared to decreasing the genome length; that is, instead of half-life increasing by 100% (as genome length is changed from 100% to 78% λ -DNA), we might expect to see the half-life

increase by just 10% for 78% λ -DNA phages as salt concentration increases from 5mM to 20mM. Such a small change in dynamics is likely not perceivable in this experiment, where each half-life value has an error of $\sim 10\%$.

However, it could also be that there is a more interesting lesson hidden within this seemingly static data. Grayson et al¹⁷ showed that DNA friction, measured during real-time observations of single phage λ ejections, is $\sim 2X$ larger for 100% λ -DNA phages than it is for 78% λ -DNA phages when the phages are fully packaged. This suggests that DNA friction is proportional to DNA pressure, and thus DNA mobility (and DNA's ability to quickly eject) is inversely proportional to pressure. Therefore, in our dynamics data for 78% λ -DNA phages in 5mM and 20mM, we may see a competition between two dynamic effects of reduced pressure caused by salt screening. According to a pressure-driven dynamics point of view, salt-screening should lead to slower dynamics. However, according to a friction-driven dynamics point of view, salt-screening should lead to faster dynamics. It is possible that these two effects are both present in our dynamics data presented here, and cancel each other out to yield the measured salt-independent dynamics.

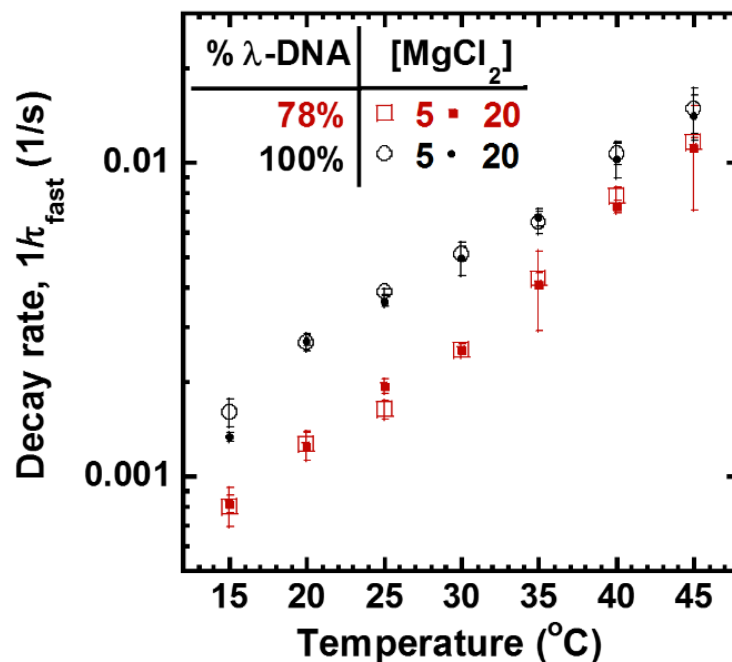


Figure 4.15: The population dynamics of DNA ejection as studied with light scattering show no dependence on salt concentration, even for 78% λ -DNA which does have a slight reduction in pressure as $MgCl_2$ is increased from 5mM to 20mM. This could be an inability of the experiment to resolve such small changes in dynamics, or it could be an indication of competing effects of pressure-driven versus friction-driven dynamics.

4.4 Ejection dynamics and viral fitness

The measured activation energy value for initiation of receptor-triggered DNA ejection is, in units of $kT_{\text{body}}/\text{phage}$ (at $T_{\text{body}} = 37^\circ\text{C}$): ~ 20 for 100% λ -DNA phage, ~ 28 for 78% λ -DNA phage. This energy is required for the critical thermo-mechanical destabilization that causes the portal to open. It is interesting to note that this energy barrier is ~ 4 times smaller than that associated with the heat-triggered DNA ejection without a receptor⁵, indicating that receptor binding significantly lowers the threshold for critical thermo-mechanical destabilization of the portal. Our data shows that at 40°C (close to the optimum temperature for infection of $\sim 37^\circ\text{C}$), the introduction of receptor leads to a 600 times decrease in the half-life of infectious phage λ particles (without LamB, $t_{1/2} = 7.5$ hours⁵, while with LamB $t_{1/2} = 45$ seconds, see Figure 4.13B).

Despite the receptor binding, the energy barrier for portal opening and initiation of DNA ejection remains more than an order of magnitude larger than the average molecular thermal energy⁵⁹ (~ 1.5 kT), which prevents instantaneous and synchronized DNA ejection from all phage particles. Thus, there is apparently a fail-safe double mechanism to keep DNA inside the capsid – ejection requires both receptor binding and portal opening caused by critical thermo-mechanical destabilization of the portal. This portal complex opening may be associated with removal of the so-called portal plug structure leading to ejection^{39, 41, 44} or with other conformational changes. Since keeping the DNA inside the virus is of the utmost importance for viral survival between infection events, it is not surprising that there is an energy barrier for DNA ejection, even in the presence of susceptible cells. A small energy barrier for ejection initiation, which can be overcome by thermal energy, ensures that DNA ejection events occur at a high rate at physiological temperatures but are limited at low temperatures where cellular replication machinery is inefficient.

Indeed, it is interesting to note that the activation energy measured here for receptor-triggered phage DNA ejection ($\sim 20kT_{\text{body}}$) is similar to the activation energy (measured in the same temperature range) of $\sim 22kT_{\text{body}}$ regulating the growth of the λ host, *E. coli*⁶⁰. This suggests that the phage is tuned to respond to temperature changes the same way as its host does—ensuring that rates of infection are highest when the host reproductive machinery is most efficient.

Virion metastability is one of the central concepts in virology⁶¹. It implies that the virus, in order to successfully replicate, must be sufficiently *stable* to prevent spontaneous release of its genome outside the cell between infection events, and at the same time be *unstable* enough to release its genome during

infection. Viral particles are therefore not inert structures and have not attained the minimum free energy conformation, separated by an energetic or kinetic barrier, prior to cell attachment and entry⁶¹. Thus viral structure, and in particular the delicate force balance between DNA pressure and portal strength, plays an active role in genome delivery to the host cell. The metastable state of the portal vertex in the capsid provides a paradigm of physical adaptation of viruses to the physiologic environment of their host.

4.5 Conclusions

In this work we employ a unique combination of time-resolved techniques involving both single-molecule (cryo-EM) and bulk (LS and SAXS) analysis to reveal the stochastic behavior of DNA ejection events from phage λ . Specifically, we quantify the average lag-time between receptor binding and initiation of DNA ejection from a population of phage. The lag-time is described by a characteristic time constant which is derived from the bi-exponential fit to the time-resolved LS data. While DNA translocation from a single phage λ particle occurs on the time scale of seconds¹⁷, our measured lag-time for deactivation of a phage population is on the order of minutes. This slower rate of DNA ejection events likely influences the overall replication dynamics of the infectious cycle *in vivo*, which is on a minutes to hours time-scale⁶⁻¹¹. Therefore, we investigate the mechanism leading to this delayed and stochastic genome ejection behavior.

We measure population dynamics of DNA ejection events at variable temperatures between 15 and 45°C. By thermally destabilizing the portal vertex on the capsid, through which DNA ejection occurs, we found that ejection dynamics increases by 15 times when the temperature is increased 3 times (lag-time decreases from ~7.5 minutes at 15°C to ~30 seconds at 45°C). We have previously found that portal vertex stability is influenced by both temperature and internal pressure of the encapsidated DNA^{5, 36}. In our investigated temperature interval, the internal DNA pressure remains unaffected³⁴ while the portal is thermally destabilized.

Furthermore, due to the strong temperature dependence of DNA ejection rate we are able to deduce the activation energy required to initiate ejection. We found that phages with greater internal DNA have a smaller activation energy barrier for ejection – this correlates well with our conclusion that DNA ejection occurs when the portal opens in response to a critical thermo-mechanical stress. The measured energy barrier for receptor-triggered ejection is four-fold smaller than the energy barrier to release phage DNA through thermal portal destabilization alone without phage LamB receptor present.

Nevertheless, even with receptor binding, the energy barrier for ejection is an order of magnitude higher than the thermal molecular energy⁵⁹. These findings suggest a fail-safe double protection mechanism at the portal vertex preventing spontaneous DNA ejection. The requirement to bind to the receptor blocks premature ejection away from the host, which would surely lead to viral demise. The requirement to overcome a residual activation energy barrier, even after receptor binding, prevents ejection in suboptimal environmental conditions (such as low temperature). In such conditions, even if the DNA did enter the host, the host cell machinery may not operate well enough to reproduce viral DNA. Our data shows that viruses already bound to the receptor can hold onto their DNA for tens of minutes if the temperature is too low!

Besides the requirement for susceptible cells with phage receptors, the thermal regulation of the portal stability also plays a significant role for viral genome delivery. That is, temperature must be sufficiently high (e.g. ~37°C corresponding to favorable replication environment in *E. coli* cells) in order for virus uncoating to take place with high efficiency. This facilitates rapid spread of infection, improving the viral fitness^{1, 3, 6}.

References

1. Wargo, A. R.; Kurath, G., Viral Fitness: Definitions, Measurement, and Current Insights. *Curr Opin Virol* **2012**, *2*, 538-545.
2. Handel, A.; Lebarbenchon, C.; Stallknecht, D.; Rohani, P., Trade-Offs between and within Scales: Environmental Persistence and within-Host Fitness of Avian Influenza Viruses. *Proc Biol Sci* **2014**, *281*.
3. Goldhill, D. H.; Turner, P. E., The Evolution of Life History Trade-Offs in Viruses. *Curr Opin Virol* **2014**, *8*, 79-84.
4. De Paepe, M.; Taddei, F., Viruses' Life History: Towards a Mechanistic Basis of a Trade-Off between Survival and Reproduction among Phages. *PLoS Biol* **2006**, *4*, e193.
5. Bauer, D. W.; Evilevitch, A., Influence of Internal DNA Pressure on Stability and Infectivity of Phage Λ . *J Mol Biol* **2015**, *427*, 3189-3200.
6. Wang, I. N., Lysis Timing and Bacteriophage Fitness. *Genetics* **2006**, *172*, 17-26.
7. Ellis, E. L.; Delbrück, M., The Growth of Bacteriophage. *J Gen Physiol* **1938**, *22*, 356-384.
8. Hershey, A. D.; Chase, M., Independent Functions of Viral Protein and Nucleic Acid in Growth of Bacteriophage. *J Gen Physiol* **1952**, *36*, 39-56.
9. Wang, I. N.; Dykhuizen, D. E.; Slobodkin, L. B., The Evolution of Phage Lysis Timing. *Evol Ecol* **1996**, *10*, 545-558.
10. Arkin, A.; Ross, J.; McAdams, H. H., Stochastic Kinetic Analysis of Developmental Pathway Bifurcation in Phage Λ Infected *Escherichia Coli* Cells. *Genetics* **1998**, *149*, 1633-1648.
11. Gallet, R.; Kannyo, S.; Wang, I. N., Effects of Bacteriophage Traits on Plaque Formation. *BMC Microbiol* **2011**, *11*, 181.
12. Roa, M.; Scandella, D., Multiple Steps During the Interaction between Coliphage Lambda and Its Receptor Protein in Vitro. *J Virol* **1976**, *72*, 182-194.
13. Schwartz, M., Reversible Interaction between Coliphage Lambda and Its Receptor Protein. *J Mol Biol* **1975**, *99*, 185-201.
14. Mangenot, S.; Hochrein, M.; Radler, J.; Letellier, L., Real-Time Imaging of DNA Ejection from Single Phage Particles. *Curr Biol* **2005**, *15*, 430-435.
15. Lof, D.; Schillen, K.; Jonsson, B.; Evilevitch, A., Forces Controlling the Rate of DNA Ejection from Phage Lambda. *J Mol Biol* **2007**, *368*, 55-65.
16. Lof, D.; Schillen, K.; Jonsson, B.; Evilevitch, A., Dynamic and Static Light Scattering Analysis of DNA Ejection from the Phage Lambda. *Phys Rev E Stat Nonlin Soft Matter Phys* **2007**, *76*, 011914.
17. Grayson, P.; Han, L.; Winther, T.; Phillips, R., Real-Time Observations of Single Bacteriophage Lambda DNA Ejections in Vitro. *Proc Natl Acad Sci U S A* **2007**, *104*, 14652-14657.
18. Wu, D.; Van Valen, D.; Hu, Q.; Phillips, R., Ion-Dependent Dynamics of DNA Ejections for Bacteriophage Lambda. *Biophys J* **2010**, *99*, 1101-1109.
19. de Frutos, M.; Letellier, L.; Raspaud, E., DNA Ejection from Bacteriophage T5: Analysis of the Kinetics and Energetics. *Biophys J* **2005**, *88*, 1364-1370.
20. de Frutos, M.; Brasiles, S.; Tavares, P.; Raspaud, E., Effect of Spermine and Dnase on DNA Release from Bacteriophage T5. *Eur Phys J E Soft Matter* **2005**, *17*, 429-434.
21. Raspaud, E.; Forth, T.; Sao-Jose, C.; Tavares, P.; de Frutos, M., A Kinetic Analysis of DNA Ejection from Tailed Phages Revealing the Prerequisite Activation Energy. *Biophys J* **2007**, *93*, 3999-4005.
22. Chiaruttini, N.; de Frutos, M.; Augarde, E.; Boulanger, P.; Letellier, L.; Viasnoff, V., Is the in Vitro Ejection of Bacteriophage DNA Quasistatic? A Bulk to Single Virus Study. *Biophys J* **2010**, *99*, 447-455.
23. Freeman, K. G.; Behrens, M. A.; Streletzky, K. A.; Olsson, U.; Evilevitch, A., Portal Stability Controls Dynamics of DNA Ejection from Phage. *J Phys Chem B* **2016**.
24. Zimm, B. H., Apparatus and Methods for Measurement and Interpretation of the Angular Variation of Light Scattering; Preliminary Results on Polystyrene Solutions. *J Chem Phys* **1948**, *16*, 1099.
25. Kaiser, A. D.; Hogness, D. S., The Transformation of *Escherichia Coli* with Deoxyribonucleic Acid Isolated from Bacteriophage Λ dg. *J Mol Biol* **1960**, *1960*, 392-415.
26. Davidson, N.; Szybalski, W., Physical and Chemical Characteristics of Lambda DNA. In *The Bacteriophage Lambda*, Hershey, A. D., Ed. Cold Spring Harbor: New York, 1971; pp 45-82.
27. Lander, G. C.; Evilevitch, A.; Jeembaeva, M.; Potter, C. S.; Carragher, B.; Johnson, J. E., Bacteriophage Lambda Stabilization by Auxiliary Protein Gpd: Timing, Location, and Mechanism of Attachment Determined by Cryo-Em. *Structure* **2008**, *16*, 1399-1406.

28. Robertson, R. M.; Laib, S.; Smith, D. E., Diffusion of Isolated DNA Molecules: Dependence on Length and Topology. *Proc Natl Acad Sci U S A* **2006**, *103*, 7310-7314.
29. Smith, D. E.; Perkins, T. T.; Chu, S., Dynamical Scaling of DNA Diffusion Coefficients. *Macromolecules* **1996**, *29*, 1372-1373.
30. Smith, D. E.; Perkins, T. T.; Chu, S., Self-Diffusion of an Entangled DNA Molecule by Reptation. *Phys Rev Lett* **1995**, *75*, 4146-4149.
31. Maier, B.; Radler, J., Conformation and Self-Diffusion of Single DNA Molecules Confined to Two Dimensions. *Phys Rev Lett* **1999**, *82*, 1911-1914.
32. Svergun, D. I.; Koch, M. H. J.; Timmins, P. A.; May, R. P., Part II: Data Analysis Methods. In *Small Angle X-Ray and Neutron Scattering from Solutions of Biological Macromolecules*, First Edition ed.; Oxford University Press: Oxford, 2013.
33. Moore, J. W.; Pearson, R. G.; Frost, A. A., *Kinetics and Mechanism*. 3rd ed.; Wiley: New York, 1981.
34. Li, D.; Liu, T.; Zuo, X.; Li, T.; Qiu, X.; Evilevitch, A., Ionic Switch Controls the DNA State in Phage Lambda. *Nucleic Acids Res* **2015**, *43*, 6348-6358.
35. De Frutos, M.; Leforestier, A.; Livolant, F., Relationship between the Genome Packing in the Bacteriophage Capsid and the Kinetics of DNA Ejection. *Biophys Rev Lett* **2014**, *09*, 81-104.
36. Bauer, D. W.; Li, D.; Huffman, J.; Homa, F. L.; Wilson, K.; Leavitt, J. C.; Casjens, S. R.; Baines, J.; Evilevitch, A., Exploring the Balance between DNA Pressure and Capsid Stability in Herpesviruses and Phages. *J Virol* **2015**, *89*, 9288-9298.
37. Bazinet, C.; King, J., The DNA Translocating Vertex of Dsdna Bacteriophage. *Annu Rev Microbiol* **1985**, *39*, 109-129.
38. Johnson, J. E.; Chiu, W., DNA Packaging and Delivery Machines in Tailed Bacteriophages. *Curr Opin Struct Biol* **2007**, *17*, 237-243.
39. Olia, A. S.; Casjens, S.; Cingolani, G., Structure of Phage P22 Cell Envelope-Penetrating Needle. *Nat Struct Mol Biol* **2007**, *14*, 1221-1226.
40. Catalano, C. E.; Cue, D.; Feiss, M., Virus DNA Packaging: The Strategy Used by Phage λ . *Mol Microbiol* **1995**, *16*, 1075-1086.
41. Perucchetti, R.; Parris, W.; Becker, A.; Gold, M., Late Stages in Bacteriophage λ Head Morphogenesis: In Vitro Studies on the Action of the Bacteriophage λ D-Gene and W-Gene Products. *Virology* **1988**, *165*, 103-114.
42. Tang, J.; Lander, G. C.; Olia, A.; Li, R.; Casjens, S.; Prevelige, P.; Cingolani, G.; Baker, T. S.; Johnson, J. E., Peering Down the Barrel of a Bacteriophage Portal: The Genome Packaging and Release Valve in P22. *Structure* **2011**, *19*, 496-502.
43. Lander, G. C.; Tang, L.; Casjens, S.; Gilcrease, E. B.; Prevelige, P.; Poliakov, A.; Potter, C. S.; Carragher, B.; Johnson, J. E., The Structure of an Infectious P22 Virion Shows the Signal for Headful DNA Packaging. *Science* **2006**, *13*, 1791-1795.
44. Lhuillier, S.; Gallopin, M.; Gilquin, B.; Brasiles, S.; Lancelot, N.; Letellier, G.; Gilles, M.; Dethan, G.; Orlova, E. V.; Couprie, J.; et al., Structure of Bacteriophage Spp1 Head-to-Tail Connection Reveals Mechanism for Viral DNA Gating. *Proc Natl Acad Sci U S A* **2009**, *106*, 8507-8512.
45. Padilla-Sanchez, V.; Gao, S.; Kim, H. R.; Kihara, D.; Sun, L.; Rossmann, M. G.; Rao, V. B., Structure-Function Analysis of the DNA Translocating Portal of the Bacteriophage T4 Packaging Machine. *J Mol Biol* **2014**, *426*, 1019-1038.
46. Leiman, P. G.; Chipman, P. R.; Kostyuchenko, V. A.; Mesyanzhinov, V. V.; Rossmann, M. G., Three-Dimensional Rearrangement of Proteins in the Tail of Bacteriophage T4 on Infection of Its Host. *Cell* **2004**, *118*, 419-429.
47. Grayson, P.; Evilevitch, A.; Inamdar, M. M.; Purohit, P. K.; Gelbart, W. M.; Knobler, C. M.; Phillips, R., The Effect of Genome Length on Ejection Forces in Bacteriophage Lambda. *Virology* **2006**, *348*, 430-436.
48. Feiss, M.; Fisher, R.; Crayton, M.; Egner, C., Packaging of the Bacteriophage λ Chromosome: Effect of Chromosome Length. *Virology* **1977**, *77*, 281-293.
49. Feiss, M.; Adyha, S., Isolation of Plaque-Forming, Galactose-Transducing Strains of Phage Lambda. *Genetics* **1972**, *71*, 189-206.
50. Liu, T.; Sae-Ueng, U.; Li, D.; Lander, G. C.; Zuo, X.; Jonsson, B.; Rau, D. C.; Schefer, I.; Evilevitch, A., Solid-to-Fluid-Like DNA Transition in Viruses Facilitates Infection. *Proc Natl Acad Sci U S A* **2015**, *112*, 14675-14680.

51. Tzlil, S.; Kindt, J. T.; Gelbart, W. M.; Ben-Shaul, A., Forces and Pressures in DNA Packaging and Release from Viral Capsids. *Biophys J* **2003**, *84*, 1616-1627.
52. Evilevitch, A.; Lavelle, L.; Knobler, C. M.; Raspaud, E.; Gelbart, W. M., Osmotic Pressure Inhibition of DNA Ejection from Phage. *Proc Natl Acad Sci U S A* **2003**, *100*, 9292-9295.
53. Purohit, P. K.; Kondev, J.; Phillips, R., Mechanics of DNA Packaging in Viruses. *Proc Natl Acad Sci U S A* **2003**, *100*, 3173-3178.
54. MacKay, D. J.; Bode, V. C., Events in Lambda Injection between Phage Adsorption and DNA Entry. *Virology* **1976**, *72*, 154-166.
55. Feiss, M.; Fisher, R. A.; Crayton, M. A.; Egner, C., Packaging of the Bacteriophage Lambda Chromosome: Effect of Chromosome Length. *Virology* **1977**, *77*, 281-293.
56. Tzlil, S.; Kindt, J. T.; Gelbart, W. M.; Ben-Shaul, A., Forces and Pressures in DNA Packaging and Release from Viral Capsids. *Biophys J* **2003**, *84*, 1616-1627.
57. Qiu, X.; Rau, D. C.; Parsegian, V. A.; Fang, L. T.; Knobler, C. M.; Gelbart, W. M., Salt-Dependent DNA-DNA Spacings in Intact Bacteriophage λ reflect Relative Importance of DNA Self-Repulsion and Bending Energies. *Physical Review Letters* **2011**, *106*.
58. Rau, D. C.; Lee, B.; Parsegian, V. A., Measurement of the Repulsive Force between Polyelectrolyte Molecules in Ionic Solution: Hydration Forces between Parallel DNA Double Helices. *Proc Natl Acad Sci U S A* **1984**, *81*, 2621-2625.
59. Swendsen, R. H., *An Introduction to Statistical Mechanics and Thermodynamics*. Oxford University Press: New York, 2012.
60. Herendeen, S. L.; VanBogelen, R. A.; Neidhardt, F. C., Levels of Major Proteins of *Escherichia Coli* During Growth at Different Temperatures. *J Bacteriol* **1979**, *139*, 185-194.
61. Flint, S. J., *Principles of Virology*. 3rd ed. ed.; ASM Press ; [Oxford : Blackwell, distributor]: Washington, D.C., 2009.

Chapter 5: Critical capsid stability (DNA packaging and retention)

In the previous chapter, we discussed the role of internal DNA pressure in the dynamics of DNA ejection dynamics. This tens of atmospheres of pressure is responsible for powering the initiation of DNA ejection – more pressure equals more stored energy which puts the virus closer to the transition state where the portal opens. Thus, greater internal DNA pressure corresponds to a smaller activation energy barrier blocking DNA ejection and a faster rate of ejection events. This information shows that DNA pressure is essential for successful viral survival and replication. However, storing the tens of atmospheres of DNA pressure within a shell made completely of protein is no easy feat. Consider, for example, the strength required of a standard car tire. Car tires must hold only a few atmospheres of pressure – a full order of magnitude less than virus shells! This raises the question of how exactly viruses are able to retain their pressurized loads. What structural and chemical requirements are there to make these shells so tough? In this chapter, we explore that question using human herpes simplex virus type-1 (HSV-1) as a model system (for more details on HSV-1, see Chapter 2).

5.1 DNA packaging and retention in HSV-1

Since DNA packaging and retention is essential for the survival of viruses, it is of particular interest to study the physical properties enabling this replication step. If HSV-1 DNA packaging during replication is successful, infectious DNA-containing C-capsids are formed. Two dead-end products, A- and B-capsids, are also formed. A-capsids, formed when packaging is initiated but aborted, are empty. B-capsids, which never initiate packaging, still contain the cleaved scaffold proteins inside¹. When DNA packaging begins, these scaffold proteins are removed to make space for DNA.

5.2.1 Procapsid expansion caused by pressure buildup

Similar to the packaging process undergone in bacteriophages, herpesvirus DNA is initially packaged into a particle called a procapsid. The procapsid is slightly smaller, fragile, spherically icosahedral, and loosely assembled². These features are in sharp contrast to the fully-packaged mature capsid, which is a larger, stronger, highly angular icosahedron with tight contact between all capsid proteins. The transition from procapsid to mature capsid is a consequence of DNA pressure. As DNA is packaged into the procapsid, the pressure grows and pushes out on the walls of the procapsid. Toward the end of packaging, this pressure causes expansion of the procapsid into the more icosahedral shape of the mature

capsid. This expanded intermediate is not, on its own, stable and must be reinforced by auxiliary proteins to form the fully matured DNA-containing capsid. Next, we discuss the roles of proteins known to be essential for DNA packaging and retention.

5.2.2 Proteins needed to form the mature HSV-1 capsid

The mature HSV-1 capsid is comprised of seven proteins: VP5, VP19C, VP23, VP26, and the proteins encoded by the genes UL25, UL17 and UL6 (hereafter, these gene names will be used to refer to their respective proteins). VP5 is the major capsid protein and the structural subunit of the capsomers, including 150 hexons (six copies of VP5, each decorated with one copy of VP26 at the tip) and 12 pentons (five copies of VP5)³⁻⁴. These capsomers are connected by 320 triplexes, which are heterodimers with one copy of VP19C and two copies of VP23³. This combination of pentons and hexons creates the icosahedral shape of the capsid, with six five-fold, ten three-fold, and fifteen two-fold rotation axes. Eleven of the twelve points of five-fold symmetry are marked by pentons, and the twelfth is occupied by the portal complex (12 copies of UL6) through which viral DNA is packaged and ejected. The pentons are each externally bound to the capsid vertex-specific component (CVSC), which is described in detail in a recent publication⁵, several figures from which have been adapted as Figure 5.1. The CVSC, specifically UL25, has been found to bind to the capsid pentons⁶⁻⁹.

Studying the role of each of these capsid proteins is key to understanding the physical characteristics of capsids. Of particular interest are the capsid proteins related to the packaging and retention of the pressurized viral genome. HSV-1 gene deletion studies¹⁰⁻¹⁶ have identified several proteins which must be present for successful packaging and retention of the pressurized viral genome. Most of these proteins are required for the initiation of DNA packaging. The exception is UL25, which is not essential for *initiation* of packaging but must be present during its final steps^{7, 10, 17-19}. UL25 gene deletion mutants¹⁸ (called UL25null), are capable of initiating DNA packaging and cleavage of DNA concatemers, but are not capable of forming infectious, DNA-filled virions¹⁰. However, UL25 mutants do produce an excess of empty A-capsids and unpackaged concatemers of DNA (they also produce, as all strains, scaffold containing B-capsids). This suggests that DNA packaging is attempted, but fails.

5.2.3 The biochemical basis for UL25 reinforcement

Structural studies of HSV-1 and its UL25null mutant have shown that five copies of UL25 bind, as part of the CVSC, between each capsid penton its five neighboring hexons, as well as the connecting triplex proteins underneath^{6-7, 18, 20-21}. Figure 5.1 specifies the locations of UL25 copies, as reported in a recent publication⁵. Since UL25 binds externally to the capsid (indeed, plugging holes in the procapsid), and since it is required for completion but not initiation of DNA packaging, it was suggested that UL25 may help stabilize the capsid against the large DNA pressure exerted on it during and after packaging^{17, 22}. In support of this, it has been shown¹⁷ that UL25null *is* capable of packaging shortened DNA chains (though this process is highly inefficient) which would exert less pressure on the capsid. This suggests that no part of the packaging process is chemically disrupted by the removal of UL25.

All together, these results suggest that the failure of UL25 mutants to produce DNA-filled C-capsids is due to reduced mechanical strength caused by the lack of UL25 reinforcement. Our previous study used AFM to reveal that UL25 increases the overall stability of capsids, even in the absence of a packaged genome²³. In that publication, we showed that UL25-null A- and B-capsids are more easily deformed than the wild-type (wt) A- and B-capsids, suggesting that UL25 acts to “cement” the capsid structure and provide structural reinforcement. Based on this difference in structural strength, we wondered if the failure of UL25null capsids to package DNA is caused by the insufficient capsid strength to retain that pressurized load?

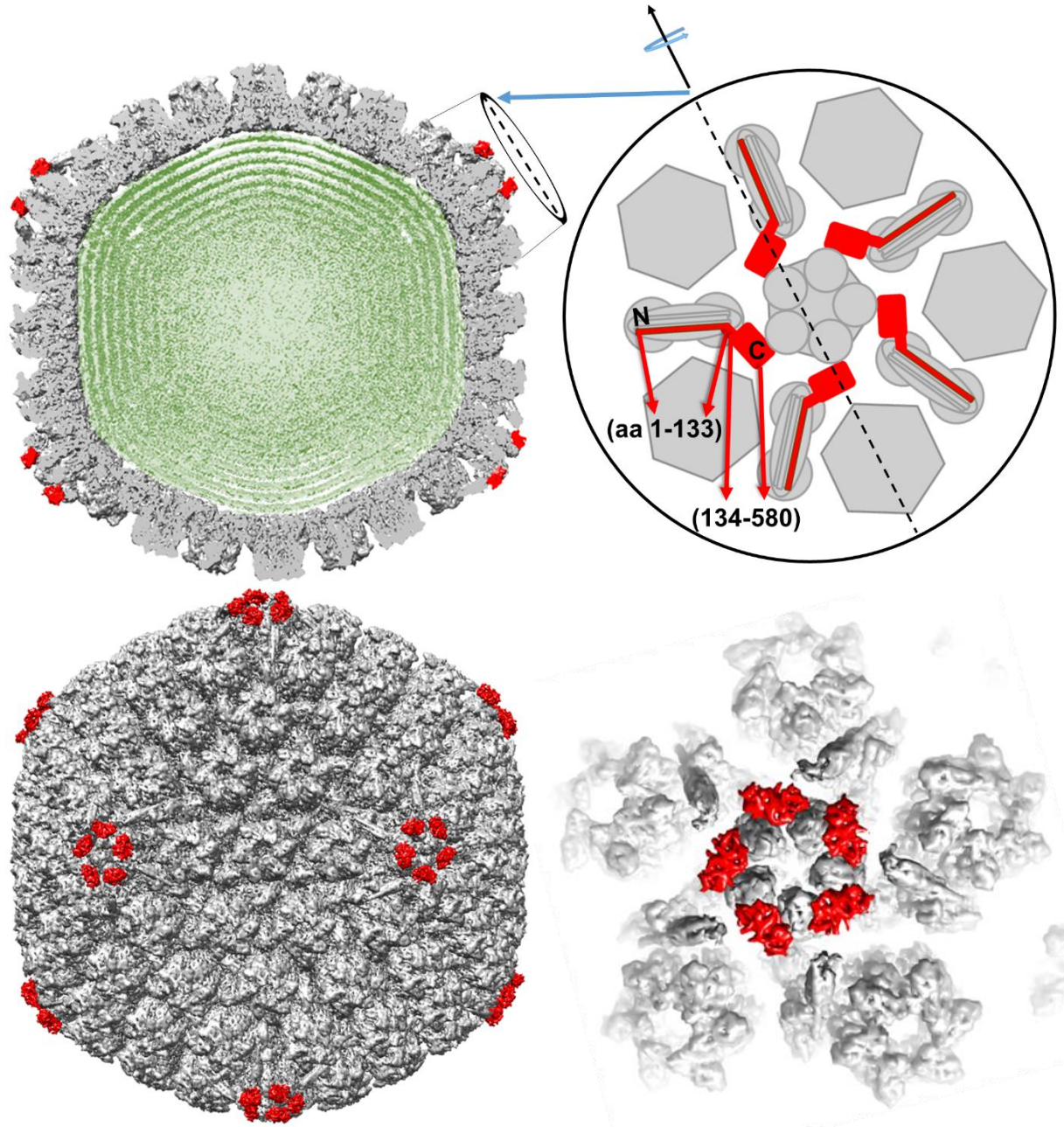


Figure 5.1: A recent publication⁵ showing the high resolution structure of the HSV-1 determined the exact structure of the CVSC. The cryo-EM reconstruction (EMDB 6386) is reproduced here with my own fitting of UL25 into the capsid density map. The diagrams show the position of UL25 (red) on the capsids. In particular, note that the 133 most N-terminal amino acids of UL25 are part of a bundle of proteins connecting triplexes and hexamers. The C-terminal amino acids, on the other hand, interact with the capsid penton.

5.3 Post-assembly mechanical reinforcement by UL25

As mentioned above, our lab recently published the first mechanical studies of UL25 reinforcement using atomic force microscopy (AFM)²³. Figure 5.2 shows the approach for such a measurement: a viral

capsid is first located and imaged with the AFM tip. The imaging serves to accurately locate the middle of the capsid, where the tip is next positioned. The final step is to “ramp”, or push, on the center of the capsid and collect so-called force curves from which to extract mechanical data. From the slope of the force curve we measure the spring constant, k (N/m), while from the sharp break in linearity of the curve we measure breaking force, F_{break} (nN). The ratio of F_{break} to k yields the indentation of the capsid before breakage (nm). The details of these measurements and necessary calculations are described in Chapter 2.

Our lab first set out to measure whether or not wild-type capsids (containing at least 60 copies of UL25) were, in fact, mechanically stronger than UL25null capsids. Since the A- and B- capsids formed by UL25null mutants are essentially identical in structure (just lacking the UL25 proteins) to wild type A- and B- capsids, my labmate Udom Sae-Ueng was able to directly compare the k and F_{break} values obtained for each to determine what effect UL25 had on capsid strength²³. The data are shown in Table 5.1 below, along with the same data for wild type C-capsids for comparison. As shown, both the stiffness (k) and breaking force are significantly smaller for UL25null capsids (both A- and B-capsids) proving that UL25 is essential for mechanical reinforcement of the capsid.

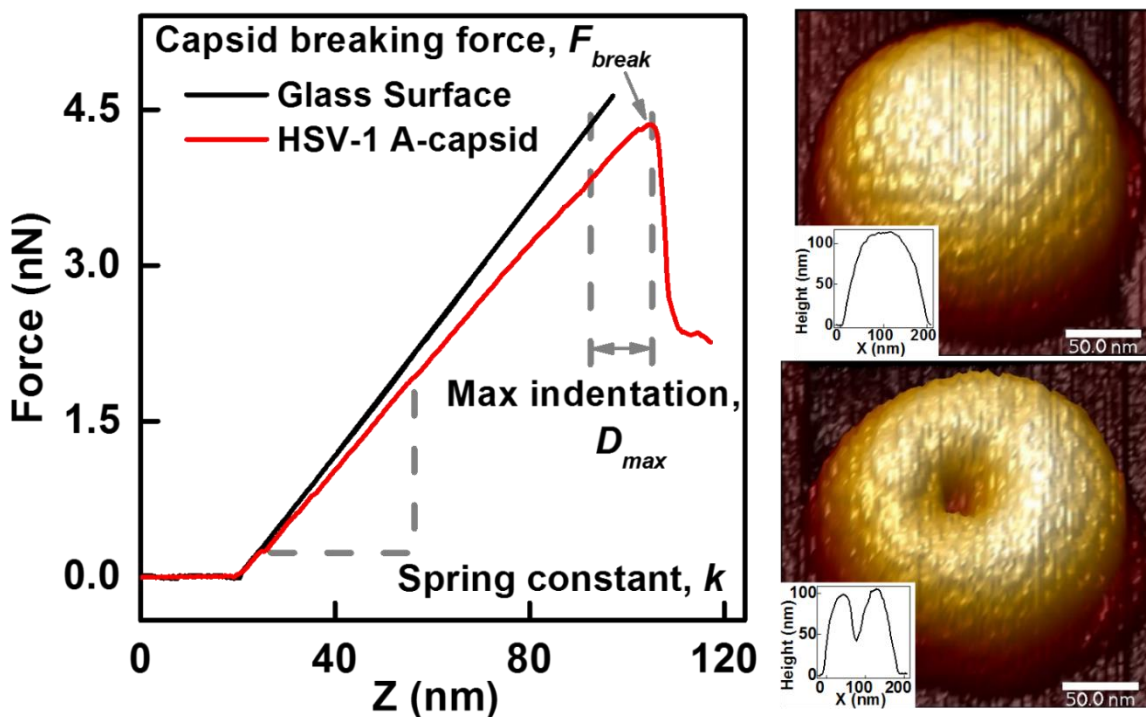


Figure 5.2: The plot on the right is a representative force curve, showing the origin of k and F_{break} measurements in our AFM experiments. The physical meaning of the indentation, which we calculate from the ratio of F_{break} to k , is also shown. The AFM images on the right show an HSV-1 capsid before and after breaking.

Beyond just comparing WT capsids to UL25null capsids, Sae-Ueng et al²³ also considered the amount of UL25 present in each type of WT capsid. It is known that the amount of bound UL25 for each capsid type varies as $UL25_{B-capsid} \ll UL25_{A-capsid} < UL25_{C-capsid}$ ¹⁸. The measured stiffness and breaking forces follow this trend, with the B-capsid being mechanically weakest and the A-capsid being strongest. This effect is most pronounced in the breaking force, which changes by nearly 2nN between wild type B- and C- capsids.

Table 5.1: UL25 mechanically reinforces A- and B- capsids*

Capsid Type	F_{break} (nN)	k (N/m)	Breaking Indentation (nm) ^a
WT C	5.7 ± 0.2	0.35 ± 0.01	16
WT A	5.3 ± 0.2	0.34 ± 0.01	16
UL25null A	3.4 ± 0.2	0.27 ± 0.01	13
WT B	3.9 ± 0.2	0.33 ± 0.01	12
UL25null B	3.0 ± 0.2	0.26 ± 0.01	12

*Data reproduced from Sae-Ueng et al²³

5.4 Mechanism of UL25 reinforcement

The selective binding of UL25 around the pentons is significant. Subject to enormous lateral and radial stresses, the pentons are thought to be the mechanically weakest point of any icosahedral capsid²⁴⁻²⁸. Its placement at this weak point suggests that UL25 stabilizes the capsid by specifically reinforcing these areas. This section of the thesis describes my contribution to this project, which was an effort to identify a mechanism of mechanical reinforcement by UL25.

In this section, each viral mutant sample varies in either the number of full-length UL25 monomers bound per capsid or, in the case of fully occupied capsids, the amino acid length of bound UL25 monomers. The results, discussed in five sections, indicate that even minor alterations to UL25 reinforcement destabilize the capsid enough to prevent DNA retention. To bridge the gap between measurements in the lab and physiological realities, we measure the mechanical strength of WT A-capsids at a range of temperatures, from lab environment (22°C) through physiological temperatures (37°C) and up to 50°C. We find that A-capsids at high temperatures have the same low breaking force as UL25null A-capsids and pentonless WT C-capsids. The similar breaking forces suggest similar mechanical failings for these capsids, none of which is strong enough to retain a pressurized genome.

5.4.1: Full occupancy for full mechanical reinforcement

To explore the effect of the number of complete UL25 proteins bound per capsid, we set up *in vitro* binding reactions with UL25null A-capsids and varying amounts of purified UL25. We used a quantitative

western blot (results and analysis described in Chapter 3 and summarized in Figure 5.2 below) to map the amount of UL25 present in the binding reaction to the resulting UL25 percent occupancy relative to wild type C-capsids. We found that the binding affinity is much stronger when UL25 binding sites (the ~60 sites near the pentons where UL25 is found on wild type capsids) are still exposed; that is, the binding curve saturates when the number of copies per capsid reaches the wild type C-capsid value.

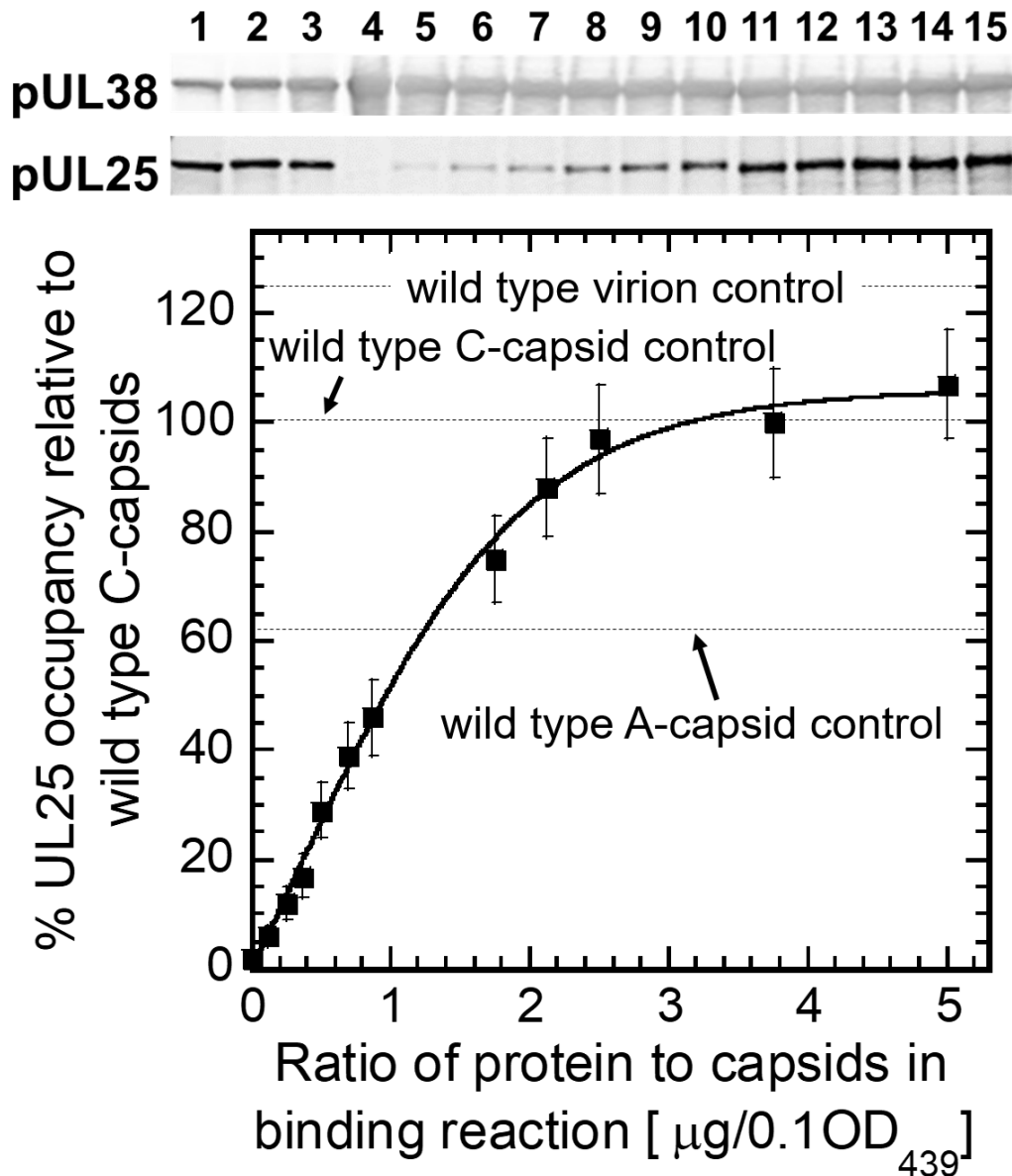


Figure 5.3: We studied the role of UL25 copy number per capsid by preparing binding reactions between UL25null A-capsids and purified UL25 protein. Analysis with quantitative Western Blots yielded the relative occupancy of UL25 on the capsids.

After quantifying the relative occupancy of UL25 binding sites, we performed AFM measurements on a selection of those binding reaction samples. Recall that these are UL25null A-capsids which have been partially occupied by the reinforcement protein UL25. As is therefore expected, the data shows partial reinforcement for the binding reaction samples. Increases in the relative occupancy are matched by increases in both k and F_{break} throughout the range of binding reaction samples. Wild type A-capsids, with a slightly larger relative occupancy than the largest binding reaction measured, have a correspondingly slightly larger mechanical strength. Similarly, wild type C-capsids are the strongest of all the HSV-1 capsid samples measured here, and also have the largest number of UL25 copies bound per capsid. These results, summarized in Table 5.2 and Figure 5.4, indicate that UL25 protein binding to the capsid is essential for viral capsid strength and stability

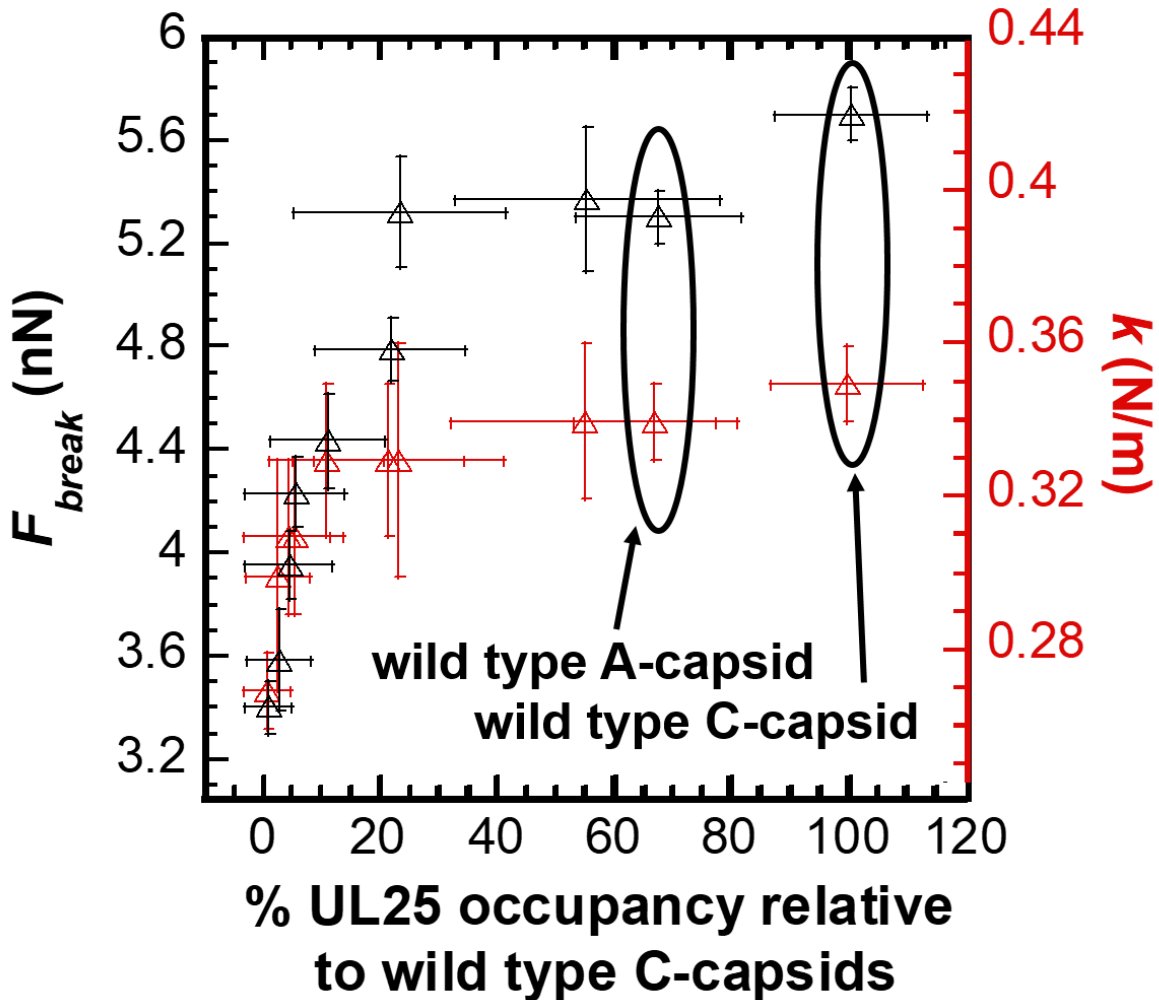


Figure 5.4: Mechanical strength as a function of UL25 copy number. Increasing the relative occupancy of UL25 per capsid increases both F_{break} and k , with both saturating as full occupancy is achieved.

While both k and F_{break} increase with UL25 copy number, they do not increase at the same rate; that is, $\Delta F_{break}/\Delta k > 1$. This detail presents itself as a 24% (12.6nm to 15.6nm) increase in the maximum indentation, $D_{max} = F_{break}/k$ (see Figure 5.5 and the numbers in Table 5.2). A capsid's stiffness determines the ease of deformation. The capsid breaks when it is deformed enough to break the bonds holding capsid proteins together. Therefore increases in k , F_{break} , and D_{max} with increasing UL25 occupancy on the capsid suggest that capsid becomes overall more resistant to deformation. When deformations do occur the protein bonds can withstand stronger forces and larger displacements before breaking. By binding to the vertex capsomeres and triplex proteins, UL25 reinforces the bonds holding the capsid together.

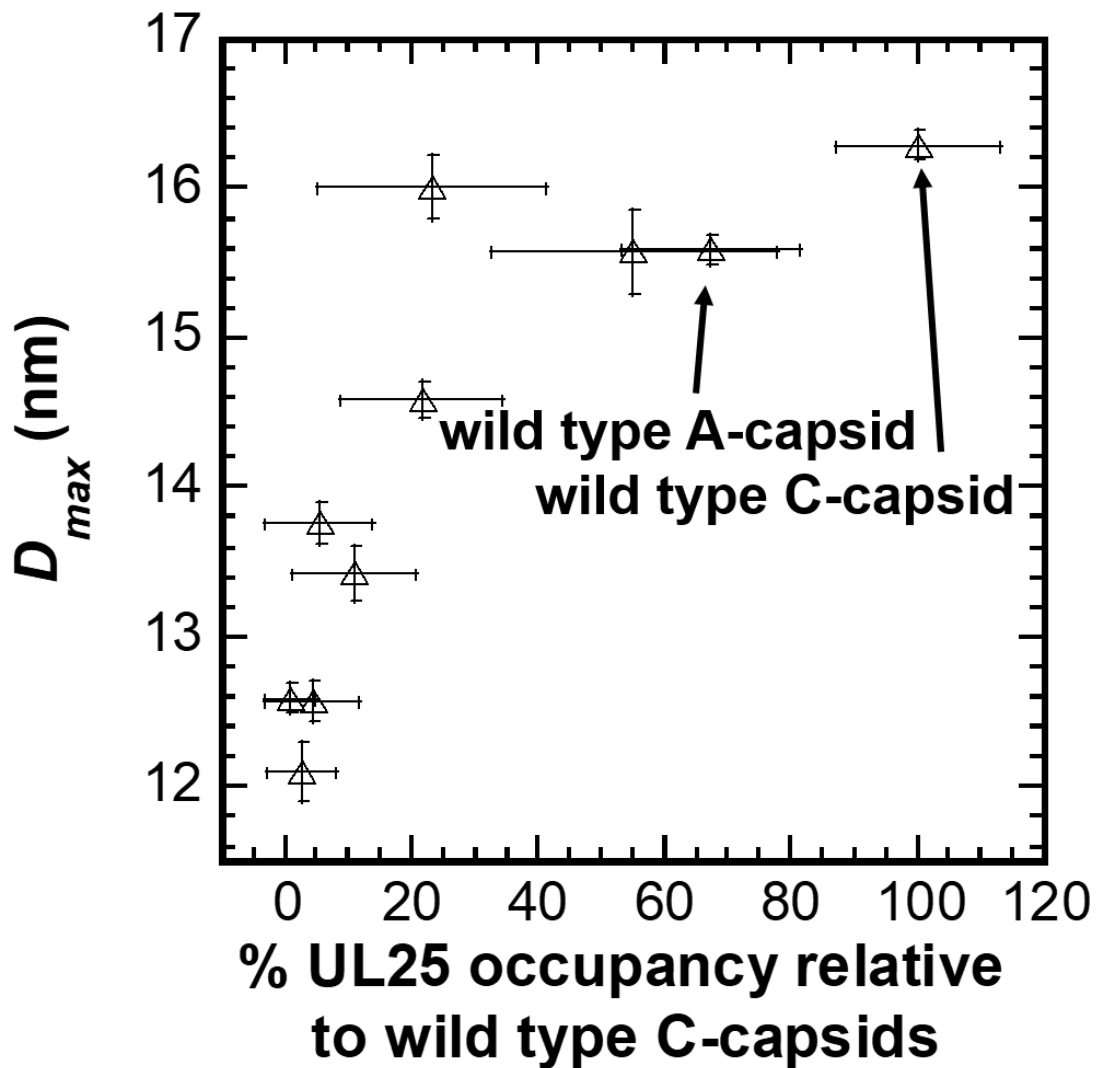


Figure 5.5: The maximum indentation before breakage increases as the capsid gains additional mechanical reinforcement from bound UL25 protein. The UL25 helps hold together the capsid subunits against increasing force and deformation.

Table 5.2: Breaking force, stiffness, and maximum indentation as a function UL25 occupancy

pUL25 in binding reaction [$\mu\text{g}/0.1\text{OD}_{439}$]	UL25 % occupancy relative to wild type A-capsids*	k (N/m)	F_{break} (nN)	D_{max} (nm)**
C-Capsid Control	100%	0.35 ± 0.01	5.7 ± 0.1	16.3 ± 0.6
A-Capsid Control	67%	0.34 ± 0.01	5.3 ± 0.1	15.6 ± 1.3
0.000	1%	0.27 ± 0.01	3.4 ± 0.1	12.6 ± 0.9
0.125	3%	0.30 ± 0.03	3.6 ± 0.2	12.1 ± 0.9
0.250	4%	0.31 ± 0.02	4.0 ± 0.1	12.6 ± 1.0
0.375	6%	0.31 ± 0.02	4.2 ± 0.1	13.8 ± 1.0
0.500	11%	0.33 ± 0.02	4.4 ± 0.2	13.4 ± 1.7
0.875	22%	0.33 ± 0.02	4.8 ± 0.1	14.6 ± 1.1
1.250	23%	0.33 ± 0.03	5.3 ± 0.2	16.0 ± 0.7
2.500	55%	0.34 ± 0.02	5.4 ± 0.3	15.6 ± 0.5

* Determined by Western Blot, described in much greater detail in Chapter 3 Section 5.

** Breaking indentation, D_{max} , is calculated as the ratio of F_{break} to k .

We also investigated the mechanical strength of mutant A- and B- capsids with modified UL25 genes that express incomplete UL25 proteins (the produced proteins are identical to the wild-type UL25 except that a particular number of amino acids has been cut off the C-terminal end of the protein). In these samples, all capsids are fully saturated with UL25 proteins during viral production *in vivo*...that is, no binding reaction is required. See Table 5.3 for the names, mutation details, and replication products of each sample. The results of this study will be discussed in the following three sections.

Table 5.3: Mutation, strain name, and capsids produced

Mutation	Strain name	Capsids produced
UL25-null	vFH439	A, B
UL25 104s*	KUL25NS	A, B
UL25 212s	vFH416	A, B
UL25 560s	vFH418	A, B
UL25 577s	vFH518	A, B, C
Wild-type (WT)	KOS	A, B, C
UL25 Δ 1-50	vFH421	A, B

*s = stop codon

5.4.2: No binding = no reinforcement

The first data to consider, summarized in Table 5.4, concerns the UL25 Δ 1-50 mutant capsids, which express UL25 protein without the first 50 amino acids. For this mutant, A- and B- capsids have the same stiffness and breaking force as UL25null A- and B- capsids. Previous studies have shown that the

first 50 amino acids of UL25 are both necessary and sufficient for in vitro binding with UL25null capsids ⁷. With the first 50 amino acids deleted, the protein cannot bind. On the other hand, UL25 containing ONLY the first 50 amino acids can bind. Our results, which show no reinforcement when the first 50 amino acids are deleted, confirm that the expressed mutant UL25 Δ 1-50 protein does bind to the capsids.

Table 5.4: Breaking forces and stiffness of the UL25 mutant capsids whose UL25 does not bind to the capsids compared to UL25-null capsids.

Virus	F_{break} (nN)	k (N/m)
UL25 Δ 1-50 B-capsid	3.1 ± 0.1	0.27 ± 0.01
UL25-null B-capsid	3.0 ± 0.1	0.26 ± 0.01
UL25 Δ 1-50 A-capsid	3.4 ± 0.1	0.27 ± 0.01
UL25-null A-capsid	3.4 ± 0.1	0.27 ± 0.01

5.4.3: Only full-length UL25 can fully reinforce the capsid

Now consider the remaining mutants, the mechanical properties of which are summarized in Table 5.5 and plotted in Figure 5.6. For A-capsids of these mutants, k increases 22% (from 0.27N/m to 0.33N/m) when the number of UL25 amino acids increases from 0 (UL25null) to 104, then remains constant upon further increase in the number of amino acids. This suggests that binding at the pentons of *any* length of UL25 “locks” the capsid structure in place, making it stiffer against small probing forces. The length of the UL25 protein, thus the number of bonds between UL25 and the capsid, does not affect capsid stiffness.

On the other hand, the A-capsid F_{break} increases 32% (from 3.4nN to 4.5nN) when #aa increases from 0 (UL25null) to 104, then continues to increase an additional 18% (from 4.5nN to 5.3nN) as #aa increases up to 580 (WT). In contrast with the effects on k , increasing the number of amino acids past 104 does indeed increase F_{break} of the capsids. The longer the monomer is, the more available sites it has to bind to the capsid. This increases the number of bonds between neighboring capsomeres. This does not affect k , since stiffness is a reflection of the capsid structure being “locked” or “unlocked” against small forces. When the probing force increases to breaking magnitudes, however, the presence of more bonds per protein does make it more difficult to pull the capsomeres apart and break the capsid.

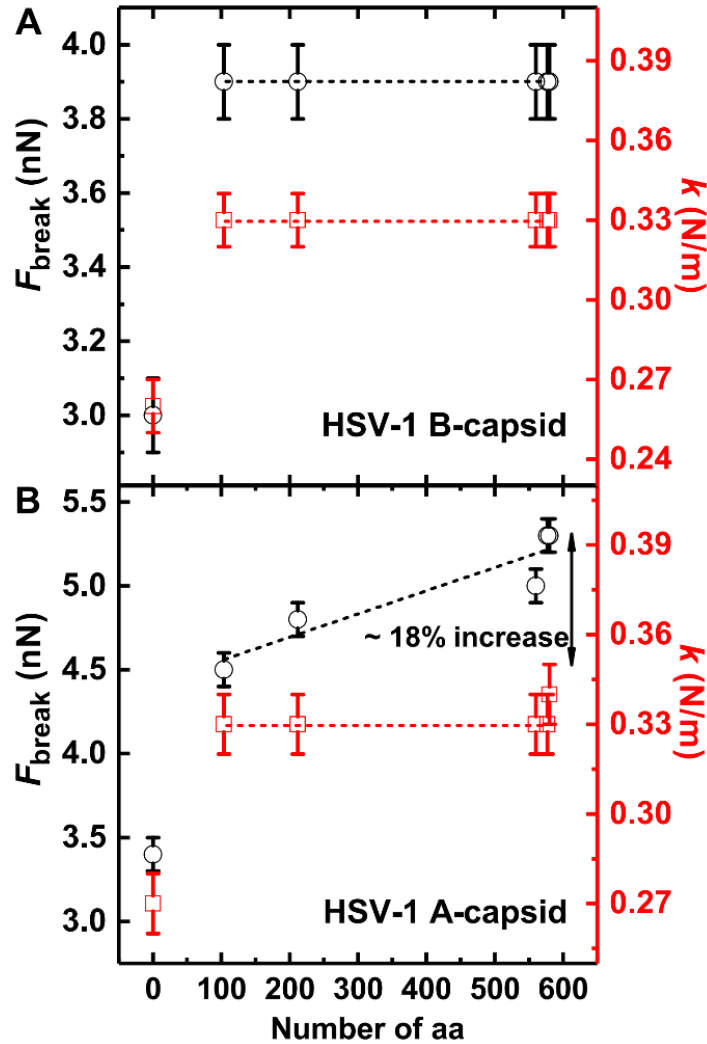


Figure 5.6: Mechanical strength of HSV-1 UL25 mutant capsids as a function of the number of amino acids (aa) of UL25 that are expressed. For both B-capsids (Fig. 3A) and A-capsids (Fig. 3B), spring constant and breaking force increase significantly when the number of aa increases from 0 (UL25null) to 104. For B-capsids, breaking force and stiffness both remain constant after 104 aa. For A-capsids, while stiffness is unchanged after 104aa, breaking force continues to increase as the number of aa increases.

For mutant B-capsids, k and F_{break} both increase when the number of UL25 amino acids increases from 0 (UL25null) to 104, and both also remain constant upon further increase in the number of amino acids. So again, like with A-capsids, the B-capsids stiffen from the “lock” of any bond with UL25. Unlike the A-capsids, however, F_{break} of mutant B-capsids does not increase further with increase in protein length/number of available bonds. This suggests that not all segments of the UL25 monomer bind to the B-capsid, even when the full length monomer is present. One explanation could be that the B-capsid does not have open sites to accept the UL25 bond. This scenario could be explained by the fact that B-capsids never expel the protein scaffold or initiate DNA packaging. These actions, which do occur for A-capsids, may trigger a capsid conformational change which exposes additional binding sites for UL25. A similar process, called timed-binding, has been observed in dsDNA viruses such as bacteriophage lambda,

where DNA packaging triggers the opening of hydrophobic sites for gpD, a minor capsid protein, to attach and increase the phage capsid strength to retain the packaged DNA^{23, 29}. Alternatively, B-capsids may

simply have a lower binding affinity for UL25 than A-capsids. The reality may be a combination of these effects or a consequence of something else entirely.

Table 5.5: Breaking forces and stiffness of the five UL25 mutant capsids and wt capsids where wt capsids contain 580-amino-acid UL25.

Virus	F_{break} (nN)	k (N/m)
UL25-null B-capsid	3.0 ± 0.1	0.26 ± 0.01
UL25-104s B-capsid	3.9 ± 0.1	0.33 ± 0.01
UL25-212s B-capsid	3.9 ± 0.1	0.33 ± 0.01
UL25-560s B-capsid	3.9 ± 0.1	0.33 ± 0.01
UL25-577s B-capsid	3.9 ± 0.1	0.33 ± 0.01
WT B-capsid	3.9 ± 0.1	0.33 ± 0.01
UL25-null A-capsid	3.4 ± 0.1	0.27 ± 0.01
UL25-104s A-capsid	4.5 ± 0.1	0.33 ± 0.01
UL25-212s A-capsid	4.8 ± 0.1	0.33 ± 0.01
UL25-560s A-capsid	5.0 ± 0.1	0.33 ± 0.01
UL25-577s A-capsid	5.3 ± 0.1	0.33 ± 0.01
WT A-capsid	5.3 ± 0.1	0.34 ± 0.01
UL25-577s C-capsid	5.8 ± 0.1	0.35 ± 0.01
WT C-capsid	5.7 ± 0.1	0.35 ± 0.01

5.5 Quantifying the critical mechanical strength needed for DNA retention

Finally we illustrate in Fig. 5.7 that only the mutant UL25-577s, which expresses all but the last 3 amino acids of UL25, can form infectious DNA-containing C capsids. Since 577s and WT A-capsids have the same maximum breaking force (while all other UL25 mutant strains have a smaller breaking force), we conclude that 577s can form DNA-containing C-capsids because of its high mechanical strength. This indicates that critical mechanical reinforcement, or the mechanical strength required for the capsid to retain its pressurized DNA, is achieved only when the number of UL25 amino acids is equal to or greater than 577. Therefore nearly all (except the last 3) amino acids are essential for the capsid stability required for infection. This relationship strongly suggests that a highly tuned mechanical strength is directly correlated with DNA packaging in the capsid and viral replication. Previous studies have found that mutant capsids with truncated UL25 can indeed retain shortened genome lengths but not the full genome length¹⁷. All of these data combined suggest that the WT genome length, the length and structure of UL25, and overall

capsid structure are highly specified to balance all of the forces involved in packaging, retaining, and ejecting the viral genome for survival and replication.

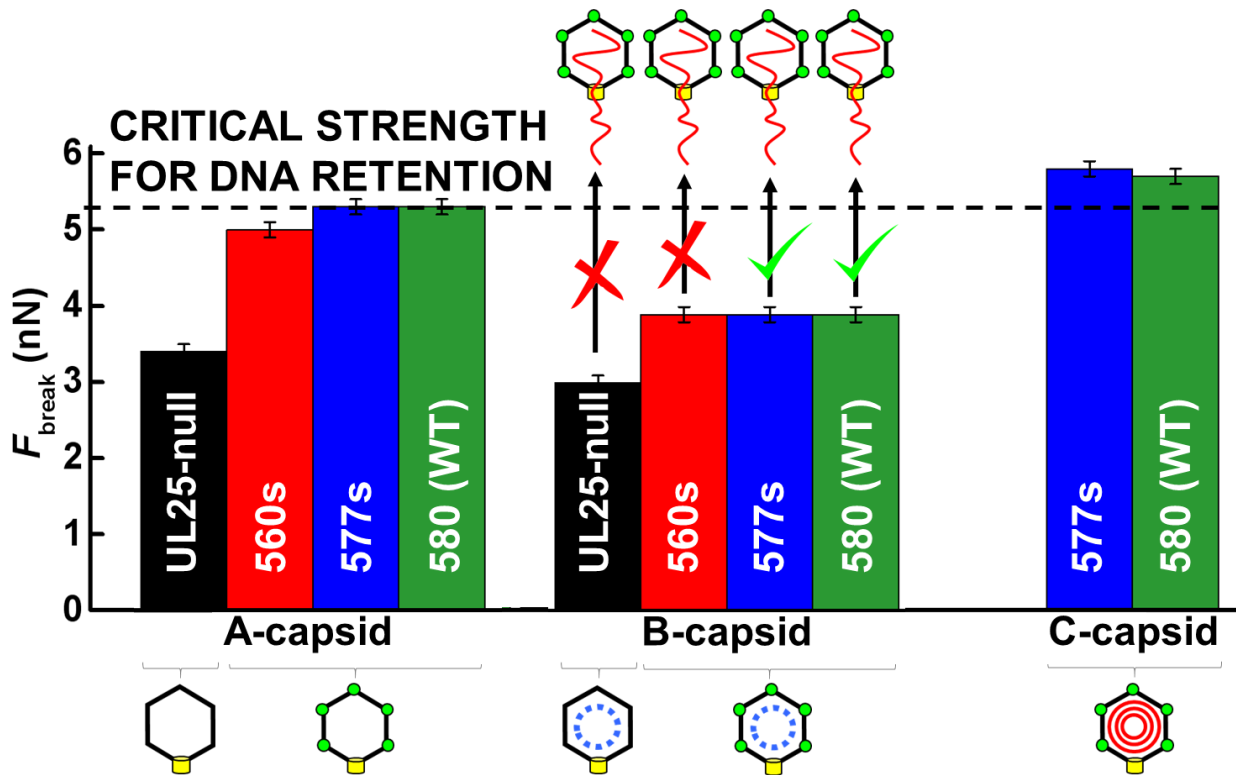


Figure 5.7: F_{break} of A-, B-, and C-capsids from four strains are compared. B-capsids are the precursor to both A- and C-capsids... A-capsids are formed from failed packing, while C-capsids are successfully packed. Of the four strains shown, only the UL25 mutant 577s and the wild type virus can package DNA and form infectious virions. Since 577s and WT A-capsids have the same F_{break} (while all other UL25 mutant strains are weaker), we conclude that 577s, with nearly full-length UL25, can form DNA-containing C-capsids due to its mechanical reinforcement by UL25.

5.6 Capsid softening at high temperatures causes mechanical failure

Finally, to bridge the gap between measurements in the lab and physiological realities, we probed the mechanical strength of WT A-capsids at a range of temperatures, from lab environment (22°C) through physiological temperatures (37°C) and up to 50°C. Our interest in high temperature capsid mechanical strength is motivated by the recent finding by Bauer et al that DNA filled C-capsids break at 52°C and eject the pressurized genome³⁰. The breakage, we posited, is due to combined thermal destabilization of the capsid and mechanical destabilization by the DNA pressure inside. These sources of destabilization were confirmed by the several-degrees higher breakage temperature measured for the less pressurized HSV mutant with 91% of the WT genome packaged.

We now report in more detail on the thermal destabilization by measuring the breaking force of WT and UL25null A-capsids as a function of temperature. Figure 5.8 shows that at low temperatures A-capsid breaking force is constant, but as the capsids approach physiological temperatures (37°C) they soften dramatically (from 5.4nN to 4.2nN); when brought to 50°C the A-capsids undergo a second significant weakening (down to 3.6nN). We believe that this sharp decrease in breaking force at 50°C is the thermal destabilization of the capsid which, when coupled with mechanical destabilization by pressurized DNA, ruptures the C-capsids at high temperatures. To support this conclusion we note that UL25null A-capsids, which we know to be too mechanically weak/unstable to retain the DNA, have the same low breaking force as the heated WT A-capsids. Indeed, this breaking force is also identical to that measured at room temperature for pentonless HSV-1 C-capsids treated with 2.0M GuHCl²⁵. The similarities in breaking force suggest structural and mechanical similarities between the capsid systems considered here; capsids weakened by either rupturing due to extreme heat, chemical extraction of pentons, or the absence of penton reinforcement by UL25 are all too unstable to retain a pressurized genome. This strongly suggests that UL25 stabilization of its five-fold vertices is essential for the capsid to withstand the internal mechanical pressure by the packaged DNA, which is in turn essential for viral survival and replication.

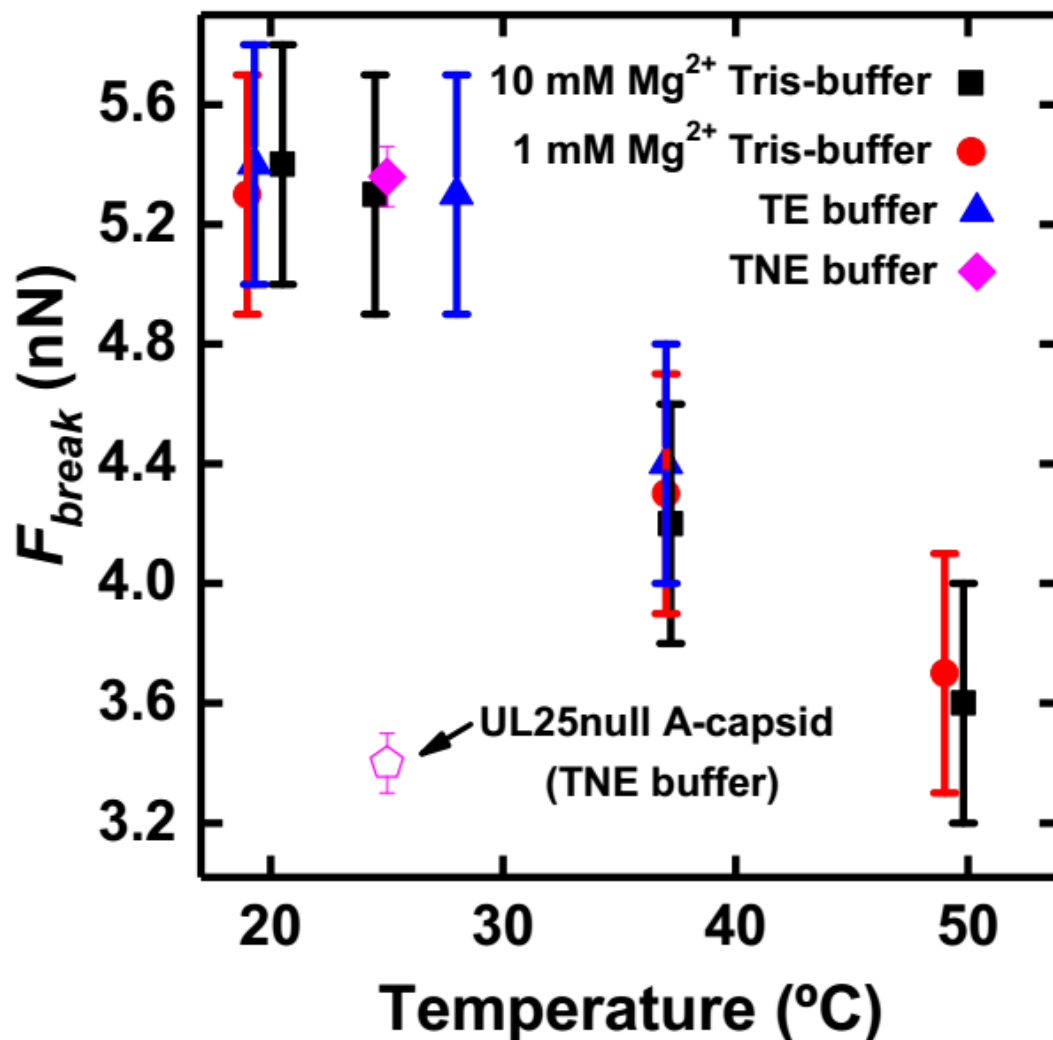


Figure 5.8: Viral breaking force as a function of temperature, for wild type A-capsids in various buffers and UL25null A-capsids. For wild type A-capsids: at low temperatures breaking force is constant, but as the capsids approach physiological temperatures (37C) they soften dramatically; when brought to 50C, where we have previously reported a temperature-induced rupturing of C-capsids, the A-capsids undergo a second significant weakening. We believe that this sharp decrease in breaking force at 50C is thermal destabilization of the capsid which, when coupled with mechanical destabilization by pressurized DNA, ruptures the C-capsids at high temperatures. To support this conclusion we note that UL25null A-capsids, which we know to be too mechanically weak/instable to retain the DNA, has the same low breaking force as the heated wt A-capsids.

5.7 Conclusions

In conclusion, we confirm that UL25 monomers strengthen the HSV-1 capsid by reinforcing its weakest point-the pentons. *In vitro* binding of UL25 to UL25null HSV-1 A-capsids mechanically reinforces the capsids by increasing spring constant and breaking force. The amount of reinforcement depends on the occupancy of UL25 binding sites. When all available sites (~60 on a wild type C-capsid) are bound with

UL25, the critical mechanical strength is achieved. A capsid with unoccupied UL25 binding sites is mechanically vulnerable – it is less stiff against small forces and particularly less resistant to hard applied breaking forces.

We find that saturating capsid reinforcement with near-full or full-length protein monomers allows successful DNA packaging and retention in HSV-1 capsids. Modification of the UL25 gene to express truncated proteins *in vivo* results in dead-end products and mechanically weaker capsids. As the number of amino acids expressed increases and the UL25 protein approaches its wild type length (580 amino acids), the capsid mechanical strength increases. When the number of amino acids reaches 577 (with only the last 3 amino acids present in wt UL25 removed) the breaking force is restored to that of wild type HSV-1 A-capsids. Importantly, among the mutant capsids expressing truncated UL25 proteins, only the mutant expressing 577 amino acids can successfully package and retain DNA to form infectious C-capsids. The fact that only the UL25-577s mutant is able to successfully form C-capsids suggests that packaging and retention of DNA is highly tuned to the mechanical strength of the wild type capsids. Even minor alterations to the capsid—a few missing copies of UL25 at the pentons or deletion of more than 3 amino acids from the end of UL25—significantly reduce the capsid's mechanical strength. It is therefore clear that the capsid has evolved, like so many natural systems, to optimize its performance with no excess materials. Each piece of the capsid serves a vital purpose and is necessary for viral survival and eventual infectivity.

Finally, we show that WT A-capsids soften with temperature, to the point of being as mechanically weak at 50°C as UL25null A-capsids and pentonless WT C-capsids, neither of which can retain the pressurized DNA. This confirms that thermal destabilization of the capsid contributes to the heat-induced rupturing of WT C-capsids at 52°C. All of these capsids, which are too mechanically unstable to retain a pressurized genome, have a unique weakness at the pentons. This adds to the growing body of evidence suggesting that the penton is the Achille's heel of the capsid, and that its reinforcement by UL25 protein is essential for viral survival and replication.

References

1. Homa, F. L.; Brown, J. C., Capsid Assembly and DNA Packaging in Herpes Simplex Virus. *Reviews in Medical Virology* **1997**, *7*, 107-122.
2. Trus, B. L.; Booy, F. P.; Newcomb, W. W.; Brown, J. C.; Homa, F. L.; Thomsen, D. R.; Steven, A. C., The Herpes Simplex Virus Procapsid: Structure, Conformational Changes Upon Maturation, and Roles of the Triplex Proteins Vp19c and Vp23 in Assembly. *Journal of molecular biology* **1996**, *263*, 447-462.
3. Newcomb, W. W.; Trus, B. L.; Booy, F. P.; Steven, A. C.; Wall, J. S.; Brown, J. C., Structure of the Herpes Simplex Virus Capsid. Molecular Composition of the Pentons and the Triplexes. *Journal of molecular biology* **1993**, *232*, 499-511.
4. Zhou, Z. H.; Dougherty, M.; Jakana, J.; He, J.; Rixon, F. J.; Chiu, W., Seeing the Herpesvirus Capsid at 8.5 Å. *Science* **2000**, *288*, 877-880.
5. Huet, A.; Makhov, A. M.; Huffman, J. B.; Vos, M.; Homa, F. L.; Conway, J. F., Extensive Subunit Contacts Underpin Herpesvirus Capsid Stability and Interior-to-Exterior Allostery. *Nature structural & molecular biology* **2016**.
6. Trus, B. L.; Newcomb, W. W.; Cheng, N.; Cardone, G.; Marekov, L.; Homa, F. L.; Brown, J. C.; Steven, A. C., Allosteric Signaling and a Nuclear Exit Strategy: Binding of UI25/UI17 Heterodimers to DNA-Filled Hsv-1 Capsids. *Mol Cell* **2007**, *26*, 479-489.
7. Cockrell, S. K.; Huffman, J. B.; Toropova, K.; Conway, J. F.; Homa, F. L., Residues of the UI25 Protein of Herpes Simplex Virus That Are Required for Its Stable Interaction with Capsids. *J Virol* **2011**, *85*, 4875-4887.
8. Toropova, K.; Huffman, J. B.; Homa, F. L.; Conway, J. F., The Herpes Simplex Virus 1 UI17 Protein Is the Second Constituent of the Capsid Vertex-Specific Component Required for DNA Packaging and Retention. *J Virol* **2011**, *85*, 7513-7522.
9. Dai, X. H.; Gong, D. Y.; Wu, T. T.; Sun, R.; Zhou, Z. H., Organization of Capsid-Associated Tegument Components in Kaposi's Sarcoma-Associated Herpesvirus. *Journal of virology* **2014**, *89*, 12694-12702.
10. McNab, A. R.; Desai, P.; Person, S.; Roof, L. L.; Thomsen, D. R.; Newcomb, W. W.; Brown, J. C.; Homa, F. L., The Product of the Herpes Simplex Virus Type 1 UI25 Gene Is Required for Encapsidation but Not for Cleavage of Replicated Viral DNA. *J Virol* **1998**, *72*, 1060-1070.
11. al-Kobaisi, M. F.; Rixon, F. J.; McDougall, I.; Preston, V. G., The Herpes Simplex Virus UI33 Gene Product Is Required for the Assembly of Full Capsids. *Virology* **1991**, *180*, 380-388.
12. Lamberti, C.; Weller, S. K., The Herpes Simplex Virus Type 1 Cleavage/Packaging Protein, UI32, Is Involved in Efficient Localization of Capsids to Replication Compartments. *J Virol* **1998**, *72*, 2463-2473.
13. Lamberti, C.; Weller, S. K., The Herpes Simplex Virus Type 1 UI6 Protein Is Essential for Cleavage and Packaging but Not for Genomic Inversion. *Virology* **1996**, *226*, 403-407.
14. Patel, A. H.; Rixon, F. J.; Cunningham, C.; Davison, A. J., Isolation and Characterization of Herpes Simplex Virus Type 1 Mutants Defective in the UI6 Gene. *Virology* **1996**, *217*, 111-123.
15. Salmon, B.; Cunningham, C.; Davison, A. J.; Harris, W. J.; Baines, J. D., The Herpes Simplex Virus Type 1 UI17 Gene Encodes Virion Tegument Proteins That Are Required for Cleavage and Packaging of Viral DNA. *J Virol* **1998**, *72*, 3779-3788.
16. Tengelsen, L. A.; Pederson, N. E.; Shaver, P. R.; Wathen, M. W.; Homa, F. L., Herpes Simplex Virus Type 1 DNA Cleavage and Encapsidation Require the Product of the UI28 Gene: Isolation and Characterization of Two UI28 Deletion Mutants. *J Virol* **1993**, *67*, 3470-3480.
17. Stow, N. D., Packaging of Genomic and Amplicon DNA by the Herpes Simplex Virus Type 1 UI25-Null Mutant Kul25ns. *J Virol* **2001**, *75*, 10755-10765.
18. Newcomb, W. W.; Homa, F. L.; Brown, J. C., Herpes Simplex Virus Capsid Structure: DNA Packaging Protein UI25 Is Located on the External Surface of the Capsid near the Vertices. *J Virol* **2006**, *80*, 6286-6294.
19. Cockrell, S. K.; Sanchez, M. E.; Erazo, A.; Homa, F. L., Role of the UI25 Protein in Herpes Simplex Virus DNA Encapsidation. *J Virol* **2009**, *83*, 47-57.
20. Ogasawara, M.; Suzutani, T.; Yoshida, I.; Azuma, M., Role of the UI25 Gene Product in Packaging DNA into the Herpes Simplex Virus Capsid: Location of UI25 Product in the Capsid and Demonstration That It Binds DNA. *J Virol* **2001**, *75*, 1427-1436.

21. Conway, J. F.; Cockrell, S. K.; Copeland, A. M.; Newcomb, W. W.; Brown, J. C.; Homa, F. L., Labeling and Localization of the Herpes Simplex Virus Capsid Protein UI25 and Its Interaction with the Two Triplexes Closest to the Penton. *J Mol Biol* **2010**, *397*, 575-586.
22. McNab, A. R.; Desai, P.; Person, S.; Roof, L. L.; Thomsen, D. R.; Newcomb, W. W.; Brown, J. C.; Homa, F. L., The Product of the Herpes Simplex Virus Type 1 UI25 Gene Is Required for Encapsidation but Not for Cleavage of Replicated Viral DNA. *Journal of virology* **1998**, *72*, 1060-1070.
23. Sae-Ueng, U.; Liu, T.; Catalano, C. E.; Huffman, J. B.; Homa, F. L.; Evilevitch, A., Major Capsid Reinforcement by a Minor Protein in Herpesviruses and Phage. *Nucleic Acids Res* **2014**, *42*, 9096-9107.
24. Zandi, R.; Reguera, D., Mechanical Properties of Viral Capsids. *Physical Review E* **2005**, *72*.
25. Roos, W. H.; Radtke, K.; Kniesmeijer, E.; Geertsema, H.; Sodeik, B.; Wuite, G. J., Scaffold Expulsion and Genome Packaging Trigger Stabilization of Herpes Simplex Virus Capsids. *Proc Natl Acad Sci U S A* **2009**, *106*, 9673-9678.
26. Roos, W. H.; Gibbons, M. M.; Arkhipov, A.; Uetrecht, C.; Watts, N. R.; Wingfield, P. T.; Steven, A. C.; Heck, A. J.; Schulten, K.; Klug, W. S.; et al., Squeezing Protein Shells: How Continuum Elastic Models, Molecular Dynamics Simulations, and Experiments Coalesce at the Nanoscale. *Biophys J* **2010**, *99*, 1175-1181.
27. Hernando-Perez, M.; Pascual, E.; Aznar, M.; Ionel, A.; Caston, J. R.; Luque, A.; Carrascosa, J. L.; Reguera, D.; de Pablo, P. J., The Interplay between Mechanics and Stability of Viral Cages. *Nanoscale* **2014**, *6*, 2702-2709.
28. Carrasco, C.; Carreira, A.; Schaap, I. A.; Serena, P. A.; Gomez-Herrero, J.; Mateu, M. G.; de Pablo, P. J., DNA-Mediated Anisotropic Mechanical Reinforcement of a Virus. *Proc Natl Acad Sci U S A* **2006**, *103*, 13706-13711.
29. Medina, E.; Nakatani, E.; Kruse, S.; Catalano, C. E., Thermodynamic Characterization of Viral Procapsid Expansion into a Functional Capsid Shell. *Journal of molecular biology* **2012**, *418*, 167-180.
30. Bauer, D. W.; Li, D.; Huffman, J. B.; Homa, F. L.; Wilson, K.; Leavitt, J. C.; Casjens, S. R.; Baines, J. D.; Evilevitch, A., Exploring the Balance between DNA Pressure and Capsid Stability in Herpes and Phage. *J Virol* **2015**, pii: JVI.01172-15. [Epub ahead of print].

Chapter 6: Conclusions and future perspectives

Physical virology is a recent endeavor to use physics-based theories, modelling techniques, and experimental methods to contribute in a unique way to the study of viruses. Traditionally, viruses have been studied in clinical or biological laboratory settings; these classic studies established the foundations¹⁻⁵ of virology and uncovered countless essential details that shape our understanding of these unique particles. Centuries of impressive work by doctors and molecular biologists, combined with the unifying universal threat viruses pose to humans, have generated in recent decades an interest in studying virology among scientists of other disciplines. Physicists and physical chemists have helped bring to modern virology a zeal for quantification, structural studies, and mechanism-based research. Considering the virus as a genome-loaded nano-container, rather than a biochemically complex pathogen, has reduced the problem to one of mechanics. Understanding these mechanics has proven to be beneficial in understanding the virus as a whole. Using the basic research results generated by physical virologists, clinical virologists can now pinpoint specific functions, performed by specific biological or chemical components of the virus, with which to interfere. This can be done, for example, by intentionally developing antiviral drugs that inhibit a specific task of the virus (rather than finding, by chance, a compound that works as an antiviral drug and only later discovering its mechanism of action). Therefore, quantified fundamental research into the structure and function of viruses will be of great benefit to clinical virology research and thus to mankind.

This doctoral dissertation explores two important components of double stranded DNA virus survival: the ability of the virus to efficiently infect its host, and the ability of the virus to retain its pressurized DNA load. Using bacteriophage λ and herpes simplex virus type-1 as model systems, we have explored the role of DNA pressure in DNA ejection and retention. These two important components of the viral replication cycle have opposite dependences on pressure, leading to a seeming paradox in viral design. We explore that paradox here.

We have shown that a combination of pressure and temperature is responsible for the rapid initiation of DNA ejection. To initiate DNA ejection a virus must, in addition to binding to a chemical trigger (the receptor protein for bacteriophages, or the nuclear pore complex for herpesviruses), generate a critical thermo-mechanical stress to exert on its portal complex. This thermo-mechanical stress comes from a

combination of stored internal DNA energy and thermal energy harvested from the environment. We have concluded that this requirement to both bind to a receptor and also overcome an additional energy barrier is a double-lock mechanism employed by the virus to prevent useless ejection⁶. All of this data strongly suggests that dsDNA viruses are evolutionarily tuned to infect at physiological temperatures. The capsid size is tuned exactly to create a certain pressure when packaged with the genome. The portal stability is tuned exactly to open, essentially instantaneously at physiological temperatures, when pushed on by that DNA pressure. If any component of the system were changed (capsid size, genome length, portal strength, host temperature, etc.) the success of viral replication would be at risk.

We also explored the effect of pressure in one of the last steps of viral replication: DNA packaging and retention. To package that enormous DNA pressure, the virus must use a powerful molecular motor – one of the strongest molecular motors in existence⁷, in fact! If the viral capsid is not strong enough to stand up to this packaging process, infectious virions cannot be formed. We have found that minor capsid proteins are responsible for reinforcing the capsid during and after the DNA packaging process⁸. We explored the mechanism of this reinforcement for HSV-1 and its capsid protein expressed by the gene UL25 (protein is referred to as UL25 here, for simplicity). We found that capsid strength, as measured by spring constant and breaking force, is linearly proportional to the number of UL25 copies bound to the capsid. This dependence holds for capsids that are not saturated with UL25; however, once full occupancy is achieved, the strength remains constant. This strongly indicates that reinforcement occurs at the pentons, known to be the weakest points of any icosahedral structure, and that reinforcement of all capsid vertices is essential for viral capsid stability. Furthermore, we found that shortening the UL25 protein by more than 3 amino acids (out of 580 amino acids total) weakens the capsid. This reduction in particle strength is accompanied by a failure to form infectious DNA-containing virions. Thus, we conclude that a minimum capsid strength is required to package and retain the pressurized DNA.

Thus, we see that pressure is essential for efficient infection by viruses but also that pressure requires an extremely strong capsid. There must be a balance between storing enough energy (as DNA pressure) to power DNA ejection and storing more energy than the capsid can hold within its walls. This balance of pressure has been optimized through evolution, and results in the finely tuned and highly

reproducible replication cycle of viruses. It is very interesting that many dsDNA viruses share similar pressures – even those with very different capsid and genome sizes. This suggests that pressure is a universal mechanism employed by these viruses. Learning how to disrupt this pressure may lead to broad-spectrum antiviral drugs.

Future perspectives

There is still a wealth of fundamental research to be done on viruses. The data presented here generates several questions that would be interesting to answer. Does the size of a virus impact its ejection dynamics or mechanical strength? Do viruses which infect hosts with lower physiological temperatures (such as bird or fish viruses) have temperature-dependent dynamics which are optimized to their hosts? Is it possible to weaken a capsid *just enough* to allow it to still package its DNA within the safe confines of the nucleus, but rupture soon after exiting the cell and entering a harsher environment?

Aside from these topics related to the work in this dissertation, there are countless other topics worthy of investigation. How does the DNA packaging motor work? What drives capsid self-assembly? What is the nature of the signal sent when the virus binds to its receptor? It is clear that the work of physical virologists will not soon be over...studying viruses has opened an entirely new arena, rich with systems found nowhere else in nature, for physicists to explore.

References

1. Jenner, E., *An Inquiry into the Causes and Effects of the Variolae Vaccinae*. Classics of Medicine Library, Division of Gryphon Editions: London, 1801.
2. Pasteur, M., An Address on Vaccination in Relation to Chicken Cholera and Splenic Fever. *British medical journal* **1881**, 2, 283.
3. Hershey, A. D.; Chase, M., Independent Functions of Viral Protein and Nucleic Acid in Growth of Bacteriophage. *J Gen Physiol* **1952**, 36, 39-56.
4. Schwartz, M., Reversible Interaction between Coliphage Lambda and Its Receptor Protein. *J Mol Biol* **1975**, 99, 185-201.
5. MacKay, D. J.; Bode, V. C., Binding to Isolated Phage Receptors and L DNA Release in Vitro. *Virology* **1976**, 72, 167-181.
6. Freeman, K. G.; Behrens, M. A.; Streletzky, K. A.; Olsson, U.; Evilevitch, A., Portal Stability Controls Dynamics of DNA Ejection from Phage. *J Phys Chem B* **2016**, 120, 6421-6429.
7. Smith, D. E.; Tans, S. J.; Smith, S. B.; Grimes, S.; Anderson, D. L.; Bustamante, C., The Bacteriophage ϕ 29 Motor Can Package DNA against a Large Internal Force. *Nature* **2001**, 413.
8. Sae-Ueng, U.; Liu, T.; Catalano, C. E.; Huffman, J. B.; Homa, F. L.; Evilevitch, A., Major Capsid Reinforcement by a Minor Protein in Herpesviruses and Phage. *Nucleic Acids Res* **2014**, 42, 9096-9107.